POROUS SILICON AS A PLATFORM FOR GRADIENT REFRACTIVE INDEX PHOTONICS

BY

NEIL A. KRUEGER

DISSERTATION

Submitted in partial fulfillment of the requirements
for the degree of Doctor of Philosophy in Materials Science and Engineering
in the Graduate College of the
University of Illinois at Urbana-Champaign, 2016

Urbana, Illinois

Doctoral Committee:

Professor Paul V. Braun, Chair
Professor John A. Rogers
Assistant Professor Kristopher A. Kilian
Professor Brian T. Cunningham

ABSTRACT

Porous silicon (PSi) is a versatile optical material that is formed by electrochemically etching bulk Silicon (Si). The refractive index of PSi is readily modulated by the electrochemical current density, making PSi inherently applicable to gradient refractive index (GRIN) applications. A GRIN broadly refers to a spatially-varying refractive index, whether discrete or continuous in nature, which offers a means for strategically controlling the flow of electromagnetic radiation. As such, GRINs are useful in different fields such as photonic crystals (PhCs) and transformation optics (TO) for applications including—but not limited to—light sources, imaging, optical communication, and solar energy conversion. This dissertation focuses on utilizing PSi as a platform for GRIN photonics.

A modified transfer-printing method was developed to modularly assembly hybrid PSi microcavities (MCs) comprised of a foreign, light-emitting cavity material sandwiched between PSi 1D PhC reflectors formed from flat Si wafers. These hybrid light-emitting MCs were imparted with tunability by the introduction of a PSi cavity coupling layer.

Next, Si wafers were patterned with conventional microfabrication techniques to provide a shape-defined path for PSi formation. The shape-defined process has realized light-focusing GRIN square micro-columns with potential on-chip applicability, as well as cylindrical GRIN microlens arrays that could be useful for integration with detector pixels or light-sheet microscopes.

Finally, work was conducted on utilizing PSi templates to create visibly transparent GRIN photonic elements. This concept is demonstrated by a combination of thermal oxidation, to create transparent porous silicon dioxide ($PSiO_2$), and infiltration with titanium dioxide (TiO_2) by atomic layer deposition, forming optically tunable discrete and continuous $PSiO_2/TiO_2$ composite GRINs.

ACKNOWLEDGEMENTS

I consider myself very fortunate to have had Professor Paul Braun as my advisor. It has been a privilege to interact with such a great scientist and human being. I thank Paul for the freedom that he allowed me, the teachings that he shared with me, and the respect that he always showed. I am also thankful for the opportunity that I have had to work with the rest of my committee. Professor Kris Kilian was instrumental in helping me establish the setup that I used for fabricating all of the porous silicon used in this dissertation. I appreciate his willingness to share his graduate school experiences to make my own experience a little smoother. Professor John Rogers and Professor Brian Cunningham have also been great collaborators and provided me with exciting opportunities. This includes working alongside some very intelligent and very hard-working people like Dr. Yuhang Wan, Dr. Xing Sheng, Dr. Lan Yin, Dr. Seung-Kyun Kang, and Yoon Lee.

The facilities available to graduate students here at Illinois are fantastic, including MRL, MNTL, and MNMS. I am incredibly grateful for the entire staff that oversees the day-to-day operations at each of these labs and does its best to keep all of the equipment fully operational. Special thanks are in order for Mike Hansen, Dr. Glennys Mensing, and Dr. Julio Soares. Not only have they taken care of some of the equipment that was of great importance to my work, they have also selflessly taken the time to teach me the tricks of the trade that they have acquired over their successful careers. I truly appreciate what they have contributed to my growth as a scientist and engineer.

My time at Illinois has also afforded me the opportunity to both work with and befriend a number of incredible people. Dr. Joe Geddes was the first to help me make the slow, painful transition from undergraduate student-athlete to graduate student researcher. I appreciate the care and patience that he showed. I am forever indebted to Dr. Hailong Ning, Dr. Corissa (Lee) Chen, and Dr. Kevin Arpin. They helped me to pick up the pieces when grad school and/or life got tough and I am blessed to have had them as not only colleagues, but friends. Dr. Matt Goodman, Dr. Chunjie Zhang, Dr. Kris Waynant, Junie Wang, Runyu Zhang, Tommy O'Brien, Hector Lopez-Hernandez, Kaitlin Tyler, Tara Cullerton, Qiujie Zhao, Christian Ocier, Dr. Brett Krull, Wayne Lin, and Dr. Tim Lach have also been a bright spot. I thank them for the useful discussions that we have had and, perhaps more importantly, the many, many laughs that we have shared.

To my dad, Bill Krueger, my biggest cheerleader in Heaven, and to my mom, Char Krueger, my biggest cheerleader on earth: thank you. Dad, I wish that you were here. It hurts to not physically have you around to share this milestone, but your lessons and love have carried me to this point, and I will carry both them and you in my heart forever. Mom, you are simply amazing. Your strength and love are seemingly immeasurable and I would not be where I am without you. I thank God for letting me be your little boy.

I have also been fortunate to be the recipient of unending support from distant but dear friends like Nick Wimberley, Nick Stone, Ben & Emily Zobrist, Chris & Lindsey Stemple, Allison Luther, and Nathan & Kendra Butkauskas. Thank you for always checking in on me and helping me to unwind on occasion. And, finally, to my greatest finding at Illinois, Ms. Hillary Valentino. I thank you for your friendship and your love, for your hand to hold and your shoulder to lean on. You are beautiful both inside and out and I am so blessed to have you and your family in my life. I cannot wait to take on life with you by my side.

TABLE OF CONTENTS

LIST OF ABBREVIATIONS

1D	one-dimensional
2D	two-dimensional
3D	three-dimensional
ALD	atomic layer deposition
AlGaAs	aluminum gallium arsenide
Al_2O_3	aluminum oxide
CCD	charge-coupled device
CCL	cavity coupling layer
DBR	distributed Bragg reflector
DFB	distributed feedback
DH	double heterostructure
DRIE	deep reactive ion etch
EMA	effective medium approximation
FTIR	Fourier transform infrared spectroscopy
FWHM	full-width half-maximum
GaAs	gallium arsenide
Ge	germanium
GRIN	gradient refractive index
GROT	graded optical thickness
HF	hydrofluoric acid
HfO_2	hafnium oxide
H_2O_2	hydrogen peroxide
H_3PO_4	phosphoric acid
Ir	iridium
IR	infrared
MC	microcavity
MEMS	microelectromechanical systems
MLA	microlens array
NIR	near-infrared
NOA	Norland optical adhesive

OPT	optical thickness
PBG	photonic bandgap
PbS	lead sulfide
PDMS	polydimethylsiloxane
PECVD	plasma-enhanced chemical vapor deposition
PhC	photonic crystal
PLGA	poly(lactic-co-glycolic acid)
PSi	porous silicon
$PSiO_2$	porous silicon dioxide
Pt	platinum
QD	quantum dot
Q-factor	quality factor
RIE	reactive ion etch
SEM	scanning electron microscope
Si	silicon
Si_3N_4	silicon nitride
SMC	square micro-column
SnO_2	tin oxide
TE	transverse electric
TiO_2	titanium dioxide
TM	transverse magnetic
TO	transformation optics
VCSEL	vertical cavity surface emitting laser
Zn	zinc
ZnO	zinc oxide

CHAPTER 1

INTRODUCTION AND BACKGROUND

1.1 Porous silicon

The discovery of porous silicon (PSi) dates back to the mid-1950s and the work of Uhlir at Bell Labs focused on electropolishing silicon (Si) in a hydrofluoric acid (HF) electrolyte[1]. The brown-colored film that resulted during Si anodization conditions was observed again a few years later in a follow-up study by Turner[2]. It turns out that Uhlir and Turner unveiled a regime of Si anodization in which Si can be etched with a porous microstructure rather than uniformly removed.

1.1.1 Formation and microstructure

The process of Si anodization consists of a Si wafer serving as the working electrode of an electrochemical cell with a HF-based electrolyte[3] (**Figure 1.1**). A positive voltage drives positive charge carriers (i.e., “holes”, designated as h^+) in the semiconducting Si to the Si/electrolyte interface where the Si is (electrically) oxidized and subsequently removed in its chemical interaction with the HF[4].

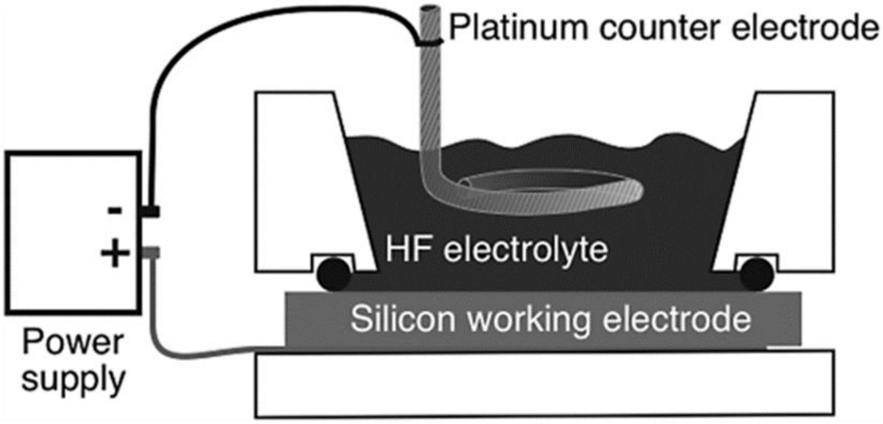

Figure 1.1. An electrochemical cell used for Si anodization. Image reproduced from[5]

At larger current densities where electropolishing occurs, Si anodization is a four-hole process[5] with the net electrochemical reaction

$$Si + 6\,F^{-} + 4\,h^{+} \rightarrow SiF_6{}^{2-} \qquad \textbf{(1.1)}$$

Consequently, the entire Si surface in contact with the electrolyte is uniformly oxidized and removed. However, as Uhlir and Turner inadvertently demonstrated, at lower current densities the Si anodization reaction becomes a two-hole process with a net electrochemical reaction of

$$Si + 6\,F^{-} + 2\,H^{+} + \,2\,h^{+} \rightarrow SiF_6{}^{2-} + H_2 \qquad \textbf{(1.2)}$$

The result is that the oxidation and removal of Si occur in an incomplete, anisotropic fashion that leaves behind a PSi microstructure[5].

PSi is, relative to the underlying bulk Si substrate, electrically "dead" and inert to further electrochemical etching[6]. As a result, electrochemical etching will only proceed where bulk Si and electrolyte are interfaced. This localized nature of the electrochemical process adds a level of versatility to PSi technology in that it enables free-standing thin films. This is accomplished by first operating in the electrochemical etching regime of Si anodization to generate a PSi thin film and then abruptly transitioning to the electropolishing regime, which breaks the PSi/Si interface[7] (**Figure 1.2**) and allows the PSi to be easily displaced from the Si wafer[8].

The microstructure of the resulting PSi, specifically the pore size, is a function of both the type (n or p) and concentration of the Si wafer doping[9]. The work in this dissertation relies on highly-doped (resistivity $< 0.05\ \Omega$ cm) p-type (100) Si wafers, resulting in a mesoporous (pore diameter ~ 2 – 50 nm) architecture (**Figure 1.3**). The porosity (i.e., void fraction) is determined by the applied etching current density (for a given set of wafer properties and electrolyte chemistry) and increases with increasing current density, providing a simple knob to tune not only the microstructure of PSi, but also its many physical properties[10] between the extrema defined by its constituents: Si and air.

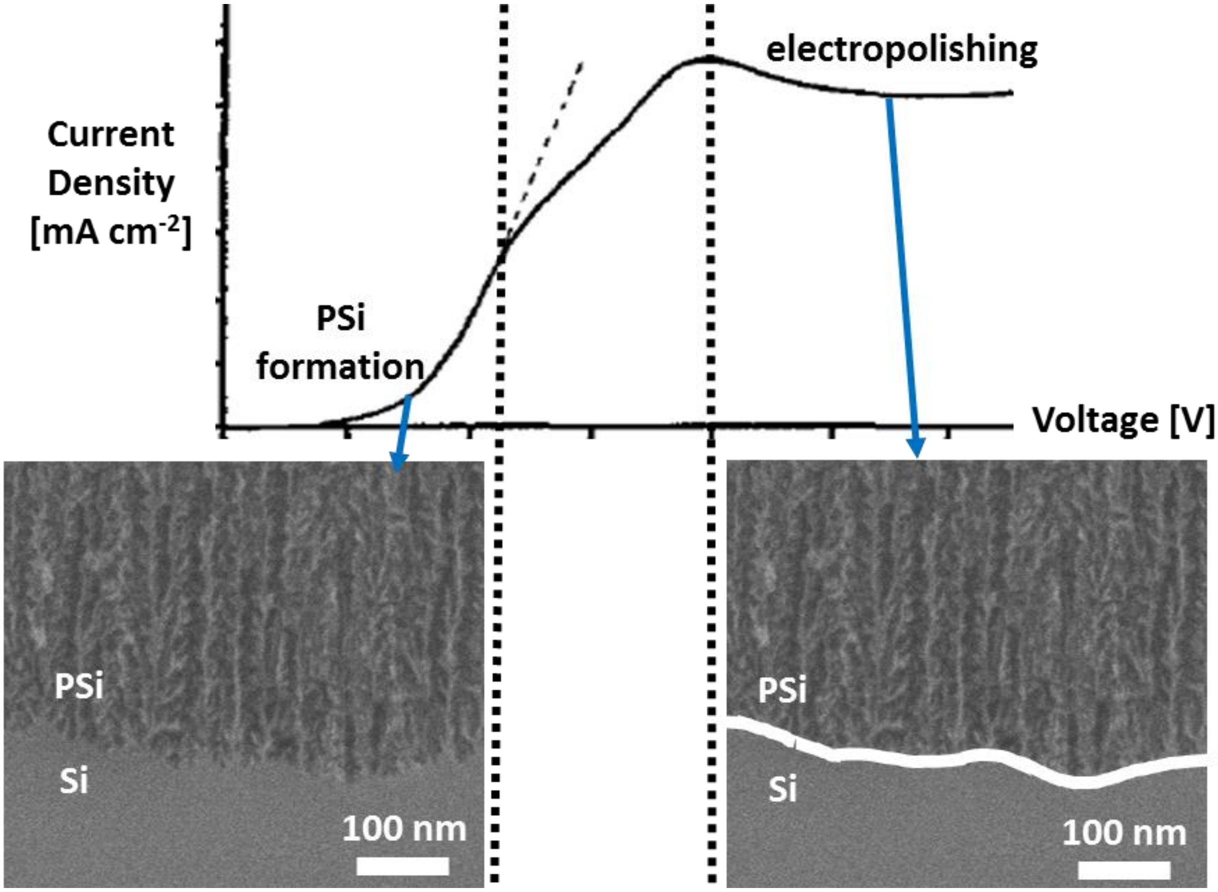

Figure 1.2. The anodization of Si features two distinct regions: the PSi formation region and the electropolishing region. When operating in the PSi formation region, Si is imparted with nanoscale porosity such as that shown in the lower left SEM image. The electropolishing region, on the other hand, uniformily removes Si in an isotropic fashion. Consequently, if the anodization process is transitioned from PSi formation to electropolishing, then the interface between the PSi film and the underlying bulk Si substrate is broken, depicted by the white trace in the lower right SEM image. Adapted from[4]

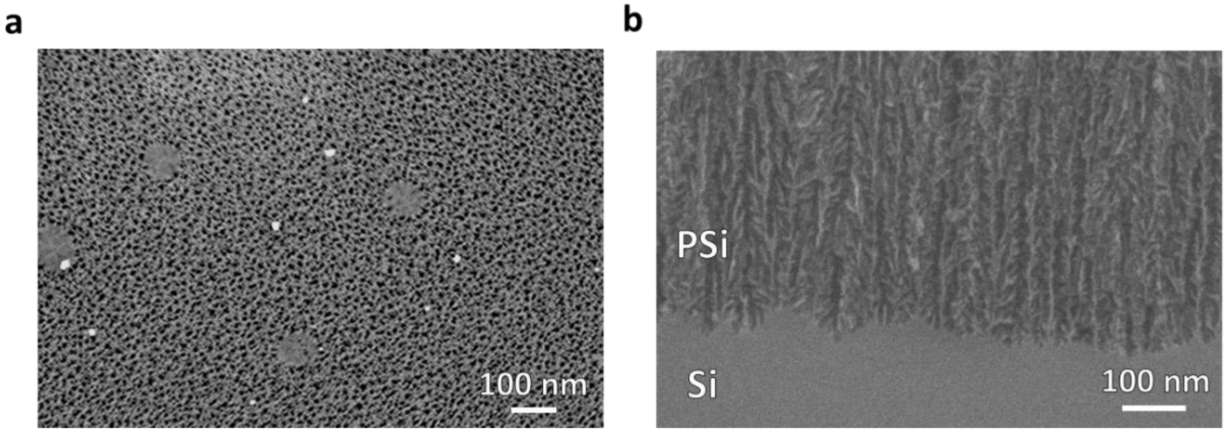

Figure 1.3. (a) Top and (b) cross-section SEM images displaying the nanoscale pores of mesoporous PSi etched from a highly-doped ($\rho < 0.01\ \Omega$ cm) p-type (100) Si wafer.

1.1.2 Optical properties

Although the tunability of PSi extends to various physical properties, the optical properties of PSi have gained the material system the most renown and are the focus of this dissertation. The intense interest in PSi as an optical material came about due to a pair of discoveries at the start of the 1990s by Canham[11] and Goesele[12]. Canham's observation of efficient photoluminescence at visible wavelengths from PSi[11] along with Goesele's report of quantum confinement effects manifest in PSi absorption[12] set off a firestorm of work to explore PSi as an enabling technology for Si-based light sources[13,14]. Despite progress to this end, interest in PSi for integrated optoelectronics[15,16] eventually subsided owing to shortcomings in performance.

While interest in PSi light-emitting technology has dissipated, it was demonstrated during the mid-1990s that PSi could be used to form porous superlattices[17] by modulating the electrochemical etching current density during formation so as to generate a (periodic) porosity (and thus refractive index) gradient along the depth of the PSi film. These PSi superlattices (**Figure 1.4**) were shown to exhibit well-defined optical signatures[18] reminiscent of optical superlattices like distributed Bragg reflectors (DBRs). This ability to electrochemically define the refractive index, coupled with the sensitivity of PSi’s optical properties to foreign media penetrating its void space[19], has significantly shaped the landscape of PSi research for the last twenty-plus years, which has largely focused on PSi as a platform for sensing with photonic architectures such as DBRs[20,21], Rugate filters[22–24], interferometric thin films[25,26], slab waveguides[27,28], and optical microcavities[29,30].

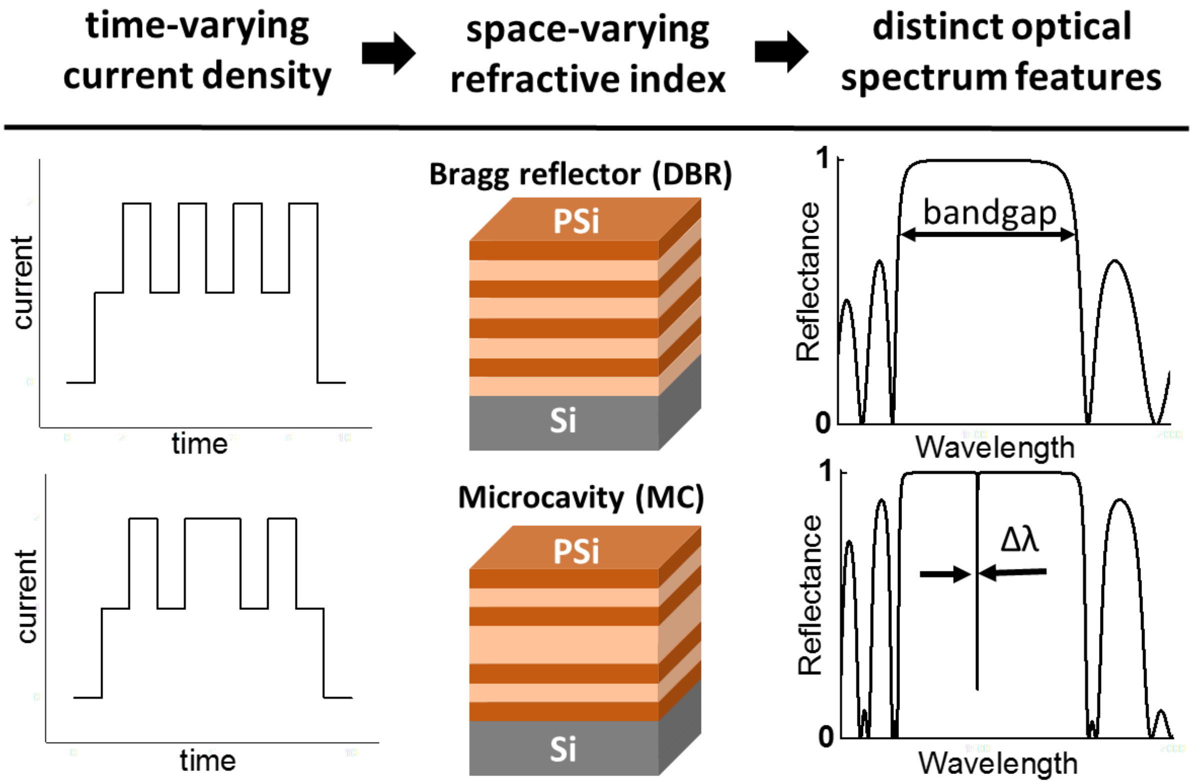

Figure 1.4. The application of a time-varying current waveform during PSi formation (left) can form an optical superlattice structure (middle) that can exhibit distinct features in their optical reflecctance and transmittance spectra (right). These spectra are sensitive to the presence of foreign media penetrating the porous architecture, which has been used as a highly sensitive platform for detecting various analytes.

The refractive index modulation of PSi has also been applied in non-sensing capacities to generate photonic architectures such as omnidirectional reflectors[31,32], anti-reflection coatings integrated with Si solar cells[33], lens-like thin films[34,35], and diffractive optics[36,37]. PSi-based DBRs have drawn consideration for use within optical interconnects[38–41], while microcavities have been shown to strongly modify the spontaneous emission of nanoscale emitters dispersed within the monolithic PSi microstructure[42–47]. Additionally, the ability to electrochemically detach PSi from its Si host substrate has enabled free-standing devices[48,49] and motivated efforts to modularly integrate functional PSi within more complex photonic device architectures by way of techniques like biofunctionalization-driven assembly[50,51] and dry removal lithography[52,53].

1.1.3 Additional applications

The versatility of PSi extends beyond optics-related applications, with the emergence of many applications pre-dating any consideration of light-matter interaction within PSi. In the 1970s, PSi found use within a new dielectric isolation technique for bipolar integrated circuits[54] and again in 1981 for dielectric isolation of lateral p-n junctions[55]. By the late-1980s, PSi had become a popular for its applicability to silicon-on-insulator technology[56,57] and in the 1990s was shown to be an excellent platform for the epitaxial growth of monocrystalline Si thin films[58], which has been further developed for transferring thin film crystalline Si solar cells[59]. Since then, PSi has also found a home in a number of microelectromechanical system (MEMS) technologies[60].

The biocompatibility of PSi[61] has generated additional opportunities for the material system. Drug delivery[62,63] is among the applications of interest, while cell/tissue culturing/engineering[64,65] have also been pursued. PSi has also played something of a passive role in this space, recently serving as a platform for transient electronic sensors designed to operate in the brain[66]. Overall, PSi is a well-studied material system with an impressive track record across a vast scientific landscape, of which the above is but a small dose. Interested readers are encourage to explore relevant reviews[10,67] and books[68,69] to gather a more complete and comprehensive overview.

1.2 Gradient refractive index optics and photonics

Broadly, the term gradient refractive index (GRIN) can be applied to any arbitrary, spatially-varying refractive index, whether discrete or continuous in nature. Light propagation through a GRIN does not follow a straight line, which explains naturally observed optical illusions like mirages. As such, strategic GRINs in the form of discrete GRIN photonic crystals, and continuous GRIN transformation optics can control the flow of electromagnetic radiation for assorted applications including light sources, imaging, optical communication, and solar energy conversion.

1.2.1 Discrete gradients: photonic crystals

Photonic crystals (PhCs) owe their functionality to a periodic refractive index that is spatially-varying at a scale on the order of the wavelength of light (**Figure 1.5**). This generates a photonic bandgap (PBG) when the multiple, coherent scattering events within the periodic structure destructively interfere in the forward direction[70], leaving the frequencies of light within the PBG incapable of freely propagating through the structure. Notable applications that utilize PBGs are dielectric mirrors/filters[71], guided resonance waveguides[72], and suppressed emission[73] (due to a suppressed density of optical states within the PBG, which, because of the conservation of the total integrated number of states, notably leads to enhancement at the edge of the PBG[74]).

In spite of the electric field profiles for frequencies within the PBG being evanescent in nature[75], they can couple into modes formed by defects in the PhC lattice that localize the electromagnetic energy, as predicted by John[76]. These localized defect modes expand the application space of PhCs. For example, a planar defect in a 1D PhC forms a miniature Fabry-Perot cavity that is the basis for vertical cavity surface emitting lasers (VCSELs)[77,78] (**Figure 1.6**) and distributed Feedback lasers (DFBs)[79].

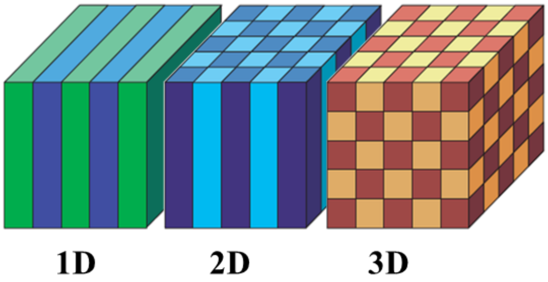

Figure 1.5. PhCs are formed by a 1-, 2-, or 3D periodic modulation of the refractive index. The refractive index modulation generates coherent scattering events that inhibit the propagation of a band of frequencies through the crystal. This is the origin of the so-called "photonic band gap", similar to the electronic band gaps discussed in solid-state physics. Adapted from[75]

Defects in 2D and 3D PhCs can similarly form low-threshold laser cavities[80]; however, they also enable the formation of complex waveguide pathways for on-chip optical circuitry[81,82]. Additionally, PBG-based light confinement applied to optical fibers generates single-mode operation at any wavelength (i.e., "endlessly single-mode")[83]. While PhCs (especially 3D) have arguably failed to make the broad, immediate, industrial impact that was anticipated, the promise of controlled light-matter interaction is likely to continue motivating researchers for years to come.

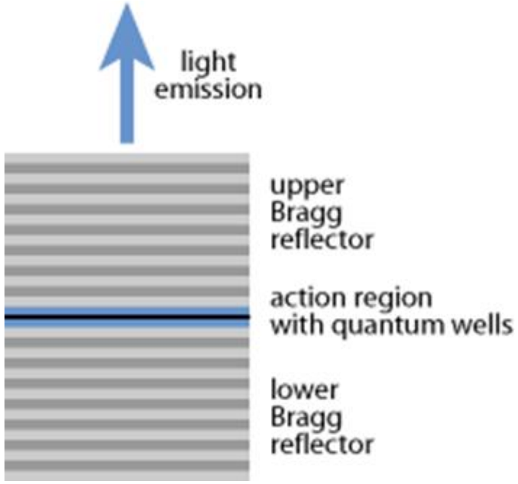

Figure 1.6. Basic optical layout of a vertical cavity surface emitting laser (VCSEL). The "action region" represents the optical cavity located between two Bragg reflectors, also known as 1D PhCs. The cavity represents a perturbation in the PhC periodicity, which enables energy localization. Reproduced from[84]

1.2.2 Continuous gradients: transformation optics

Transformation optics (TO) obtains its functionality—and name—from coordinate transformation-based refractive index distributions designed to strongly manipulate light propagation[85,86]. The desired path is defined as isotropic propagation in a virtual coordinate space. The mathematical operations describing the virtual to real (i.e., Cartesian *x*,*y*,*z*) space transformation are then applied to a material's properties (i.e., permittivity and permeability)[87,88], generating a complex spatial variation[89] that sends electromagnetic energy along the targeted trajectory (**Figure 1.7**).

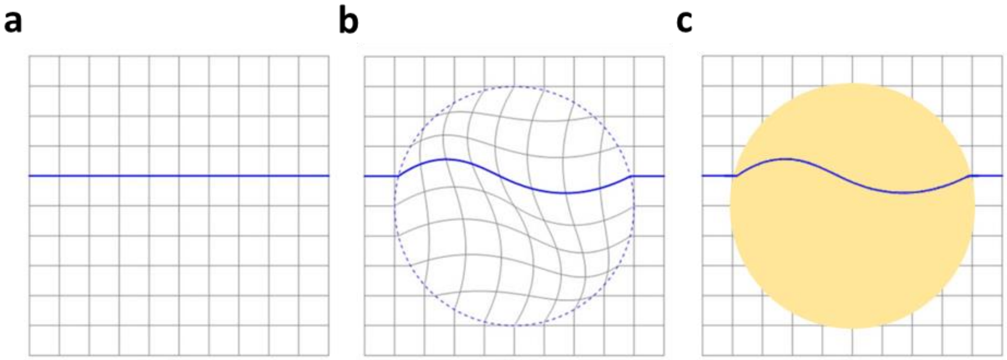

Figure 1.7. (a) Transformation optics design starts with assuming that the light propagation is isotropic in a Cartesian coordinate system. (b) In the region of interest (dashed circle), the desired light propagation trajectory is defined and assumed to be isotropic within a virtual coordinate system described by a mathematical transformation of the initial Cartesian coordinate system. (c) Application of the mathematical transformations mentioned in (b) to the previously homogeneous material properties (i.e. the permittivity, ε, and the permeability, μ) in the region of interest generates a material (solid circle) with spatially varying ε and μ that will guide light along the designed path. Adapted from[87]

The power of TO is in taking seemingly far-fetched applications and putting their realization within closer reach than once considered possible. The ultimate example is the concept of cloaking, which can render objects invisible when surrounded by an appropriately designed medium[90–92] (**Figure 1.8**). Additionally, TO-based elements provide an attractive route to directing energy flow for high-efficiency photovoltaics comprised of multi-junction solar cell modules in which each respective bandgap cell is electrically isolated from all the other cells[93]. Unfortunately, fabrication is often hindered by the required anisotropy and broadband spectral performance complicated by the use of narrowband resonance metamaterial building blocks[94]. Restricting the design space enables more practically achievable designs thanks to minimal anisotropy (quasi-conformal mapping[95,96]) or only needing a GRIN of isotropic dielectrics (conformal mapping[85,97]).

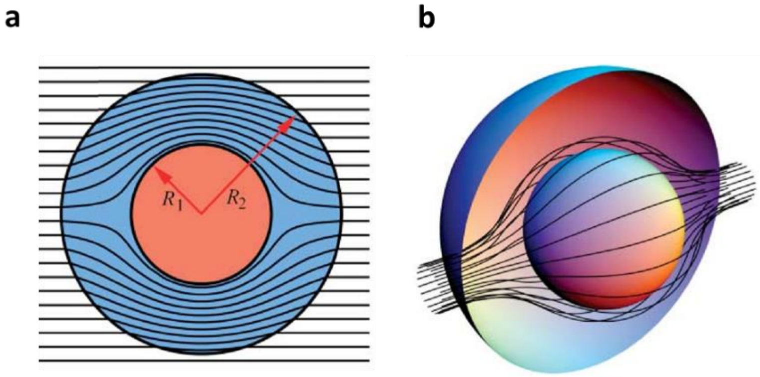

Figure 1.8. (a) 2D cross-section and (b) 3D view of light ray trajectories in a TO cloaking medium. The rays are diverted around the cloaked volume and returned to their original trajectory, seemingly unperturbed to observers. Reproduced from[86]

Restricting one's design space to conventional dielectric materials certainly does create performance limitations[98] for more advanced TO concepts, but there is still utility in this practice. Within an optically inhomogeneous medium, Fermat's principle indicates that light follows a curvilinear path[99], meaning that even a purely dielectric GRIN possesses the ability to control light propagation. Optical fibers can exploit this with a GRIN that reduces modal dispersion and enhances information capacity[100]. The application of a GRIN to other conventional elements like lenses similarly enables superior imaging performance[101] by mitigating (or even eliminating) geometrical aberrations[102]. Moreover, an appropriate radially-varying GRIN can impart an otherwise optically uninteresting geometry like a slab of glass with the optical power of a lens (**Figure 1.9**), as reportedly first demonstrated by Wood[103].

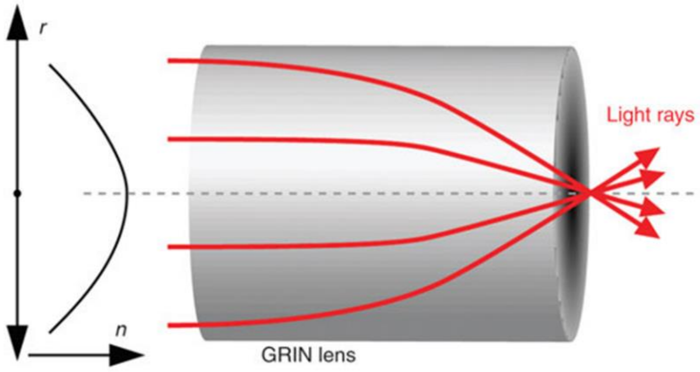

Figure 1.9. A GRIN lens uses a parabolic GRIN profile (left) to focus light. Reproduced from[104]

GRIN lenses of this nature have not only been realized, but have found widespread usage in various optical systems such as those associated with scanners/photocopiers[105,106], fiber optics[107], and endoscopes[108]. Microscale GRIN elements are also coveted for on-chip integration within photonic integrated circuits because an ability to facilitate high-efficiency fiber-to-chip coupling[102,109] and generate small photonic mode volumes[110]. Overall, the field of TO as a whole (dielectric GRINs included) figures to remain an interesting and relevant area of optical science and the pursuit of unprecedented control over light propagation for applications such as optical communications and energy harvesting.

1.3 References

1. Uhlir, A. Electrolytic Shaping of Germanium and Silicon. *Bell Syst. Tech. J.* **35,** 333–347 (1956).

2. Turner, D. R. Electropolishing Silicon in Hydrofluoric Acid Solutions. *J. Electrochem. Soc.* **105,** 402–408 (1958).
3. Zhang, X. G. in *Electrochemistry of Silicon and Its Oxide* 353–439 (Springer US, 2004).
4. Zhang, X. G., Collins, S. D. & Smith, R. L. Porous Silicon Formation and Electropolishing of Silicon by Anodic Polarization in HF Solution. *J. Electrochem. Soc.* **136,** 1561–1565 (1989).
5. Sailor, M. J. in *Porous Silicon in Practice* 1–42 (Wiley-VCH Verlag GmbH & Co. KGaA, 2011).
6. Zhang, X. G. Morphology and Formation Mechanisms of Porous Silicon. *J. Electrochem. Soc.* **151,** C69–C80 (2004).
7. Solanki, C. S. *et al.* Self-Standing Porous Silicon Films by One-Step Anodizing. *J. Electrochem. Soc.* **151,** C307–C314 (2004).
8. Lammel, G. & Renaud, P. Free-standing, mobile 3D porous silicon microstructures. *Sens. Actuators Phys.* **85,** 356–360 (2000).
9. Herino, R., Bomchil, G., Barla, K., Bertrand, C. & Ginoux, J. L. Porosity and Pore Size Distributions of Porous Silicon Layers. *J. Electrochem. Soc.* **134,** 1994–2000 (1987).
10. Korotcenkov, G. & Cho, B. K. Silicon Porosification: State of the Art. *Crit. Rev. Solid State Mater. Sci.* **35,** 153–260 (2010).
11. Canham, L. T. Silicon quantum wire array fabrication by electrochemical and chemical dissolution of wafers. *Appl. Phys. Lett.* **57,** 1046–1048 (1990).
12. Lehmann, V. & Gösele, U. Porous silicon formation: A quantum wire effect. *Appl. Phys. Lett.* **58,** 856–858 (1991).
13. Canham, L. Gaining light from silicon. *Nature* **408,** 411–412 (2000).

14. Hirschman, K. D., Tsybeskov, L., Duttagupta, S. P. & Fauchet, P. M. Silicon-based visible light-emitting devices integrated into microelectronic circuits. *Nature* **384,** 338–341 (1996).

15. Bisi, O., Ossicini, S. & Pavesi, L. Porous silicon: a quantum sponge structure for silicon based optoelectronics. *Surf. Sci. Rep.* **38,** 1–126 (2000).

16. Collins, R. T., Fauchet, P. M. & Tischler, M. A. Porous Silicon: From Luminescence to LEDs. *Phys. Today* **50,** 24–31 (2008).

17. Frohnhoff, S. & Berger, M. G. Porous silicon superlattices. *Adv. Mater.* **6,** 963–965 (1994).

18. Vincent, G. Optical properties of porous silicon superlattices. *Appl. Phys. Lett.* **64,** 2367–2369 (1994).

19. Bjorklund, R. B., Zangooie, S. & Arwin, H. Planar pore-filling — adsorption in porous silicon. *Adv. Mater.* **9,** 1067–1070 (1997).

20. Qiao, H., Guan, B., Gooding, J. J. & Reece, P. J. Protease detection using a porous silicon based Bloch surface wave optical biosensor. *Opt. Express* **18,** 15174 (2010).

21. Guillermain, E. *et al.* Bragg surface wave device based on porous silicon and its application for sensing. *Appl. Phys. Lett.* **90,** 241116 (2007).

22. Ciampi, S., Böcking, T., Kilian, K. A., Harper, J. B. & Gooding, J. J. Click Chemistry in Mesoporous Materials: Functionalization of Porous Silicon Rugate Filters. *Langmuir* **24,** 5888–5892 (2008).

23. Ruminski, A. M., King, B. H., Salonen, J., Snyder, J. L. & Sailor, M. J. Porous Silicon-Based Optical Microsensors for Volatile Organic Analytes: Effect of Surface Chemistry on Stability and Specificity. *Adv. Funct. Mater.* **20,** 2874–2883 (2010).

24. King, B. H. & Sailor, M. J. Medium-wavelength infrared gas sensing with electrochemically fabricated porous silicon optical rugate filters. *J. Nanophotonics* **5,** 051510–051510–14 (2011).

25. Lin, V. S.-Y., Motesharei, K., Dancil, K.-P. S., Sailor, M. J. & Ghadiri, M. R. A Porous Silicon-Based Optical Interferometric Biosensor. *Science* **278,** 840–843 (1997).

26. Létant, S. & Sailor, M. J. Detection of HF Gas with a Porous Silicon Interferometer. *Adv. Mater.* **12,** 355–359 (2000).

27. Rong, G., Najmaie, A., Sipe, J. E. & Weiss, S. M. Nanoscale porous silicon waveguide for label-free DNA sensing. *Biosens. Bioelectron.* **23,** 1572–1576 (2008).

28. Rong, G., Ryckman, J. D., Mernaugh, R. L. & Weiss, S. M. Label-free porous silicon membrane waveguide for DNA sensing. *Appl. Phys. Lett.* **93,** 161109 (2008).

29. Mulloni, V. & Pavesi, L. Porous silicon microcavities as optical chemical sensors. *Appl. Phys. Lett.* **76,** 2523–2525 (2000).

30. Stefano, L. D., Rendina, I., Moretti, L. & Rossi, A. M. Optical sensing of flammable substances using porous silicon microcavities. *Mater. Sci. Eng. B* **100,** 271–274 (2003).

31. Ariza-Flores, A. D., Gaggero-Sager, L. M. & Agarwal, V. White metal-like omnidirectional mirror from porous silicon dielectric multilayers. *Appl. Phys. Lett.* **101,** 031119–031119–3 (2012).

32. Bruyant, A., Lérondel, G., Reece, P. J. & Gal, M. All-silicon omnidirectional mirrors based on one-dimensional photonic crystals. *Appl. Phys. Lett.* **82,** 3227–3229 (2003).

33. Selj, J. H., Thøgersen, A., Foss, S. E. & Marstein, E. S. Optimization of multilayer porous silicon antireflection coatings for silicon solar cells. *J. Appl. Phys.* **107,** 074904 (2010).

34. Ilyas, S. & Gal, M. Gradient refractive index planar microlens in Si using porous silicon. *Appl. Phys. Lett.* **89,** 211123–211123–3 (2006).

35. Zhong, F., Lü, X., Jia, Z. & Tian, M. Microlens fabricated in silicon on insulator using porous silicon. *Optoelectron. Lett.* **9,** 105–107 (2013).

36. Golub, M. A., Hutter, T. & Ruschin, S. Diffractive optical elements with porous silicon layers. *Appl. Opt.* **49,** 1341–1349 (2010).

37. Lai, M., Sridharan, G. M., Parish, G., Bhattacharya, S. & Keating, A. Multilayer porous silicon diffraction gratings operating in the infrared. *Nanoscale Res. Lett.* **7,** 645 (2012).

38. Weiss, S. M. Tunable Porous Silicon Photonic Bandgap Structures: Mirrors for Optical Interconnects and Optical Switching. (University of Rochester, 2005).

39. Weiss, S. M. & Fauchet, P. M. Electrically tunable porous silicon active mirrors. *Phys. Status Solidi A* **197,** 556–560 (2003).

40. Weiss, S. M., Haurylau, M. & Fauchet, P. M. Tunable Porous Silicon Mirrors for Optoelectronic Applications. in *Symposia E/F – Physics and Technology of Semiconductor Quantum Dots – Nanocrystalline Semiconductor Materials and Devices* **737,** F3.50 (2002).

41. Song, D. Porous silicon based micro-opto-electro-mechanical-systems (MOEMS) components for free space optical interconnects. (State University of New York at Albany, 2008).

42. Venturello, A. *et al.* Controlled light emission from dye-impregnated porous silicon microcavities. *J. Non-Cryst. Solids* **352,** 1230–1233 (2006).

43. Dwivedi, V. K., Pradeesh, K. & Vijaya Prakash, G. Controlled emission from dye saturated single and coupled microcavities. *Appl. Surf. Sci.* **257,** 3468–3472 (2011).

44. Qiao, H. *et al.* Optical properties of II-VI colloidal quantum dot doped porous silicon microcavities. *Appl. Phys. Lett.* **96,** 161106 (2010).

45. Weiss, S. M., Zhang, J., Fauchet, P. M., Seregin, V. V. & Coffer, J. L. Tunable silicon-based light sources using erbium doped liquid crystals. *Appl. Phys. Lett.* **90,** 031112 (2007).

46. DeLouise, L. A. & Ouyang, H. Photoinduced fluorescence enhancement and energy transfer effects of quantum dots porous silicon. *Phys. Status Solidi C* **6,** 1729–1735 (2009).

47. Jenie, S. N. A. *et al.* Lanthanide Luminescence Enhancements in Porous Silicon Resonant Microcavities. *ACS Appl. Mater. Interfaces* (2014). doi:10.1021/am500983r

48. Ghulinyan, M., Oton, C. J., Bonetti, G., Gaburro, Z. & Pavesi, L. Free-standing porous silicon single and multiple optical cavities. *J. Appl. Phys.* **93,** 9724–9729 (2003).

49. Sychev, F. Y. *et al.* Vertical hybrid microcavity based on a polymer layer sandwiched between porous silicon photonic crystals. *Appl. Phys. Lett.* **95,** 163301 (2009).

50. Böcking, T. *et al.* Biofunctionalization of free-standing porous silicon films for self-assembly of photonic devices. *Soft Matter* **8,** 360–366 (2011).

51. Böcking, T. *et al.* Substrate Independent Assembly of Optical Structures Guided by Biomolecular Interactions. *ACS Appl. Mater. Interfaces* **2,** 3270–3275 (2010).

52. Gargas, D. J., Muresan, O., Sirbuly, D. J. & Buratto, S. K. Micropatterned Porous-Silicon Bragg Mirrors by Dry-Removal Soft Lithography. *Adv. Mater.* **18,** 3164–3168 (2006).

53. Sirbuly, D. J., Lowman, G. M., Scott, B., Stucky, G. D. & Buratto, S. K. Patterned Microstructures of Porous Silicon by Dry-Removal Soft Lithography. *Adv. Mater.* **15,** 149–152 (2003).

54. Watanabe, Y., Arita, Y., Yokoyama, T. & Igarashi, Y. Formation and Properties of Porous Silicon and Its Application. *J. Electrochem. Soc.* **122,** 1351–1355 (1975).

55. Imai, K. A new dielectric isolation method using porous silicon. *Solid-State Electron.* **24,** 159–164 (1981).

56. Bomchil, G., Halimaoui, A. & Herino, R. Porous silicon: The material and its applications in silicon-on-insulator technologies. *Appl. Surf. Sci.* **41–42,** 604–613 (1989).

57. Tsao, S. S. Porous silicon techniques for SOI structures. *IEEE Circuits Devices Mag.* **3,** 3–7 (1987).

58. Yonehara, T., Sakaguchi, K. & Sato, N. Epitaxial layer transfer by bond and etch back of porous Si. *Appl. Phys. Lett.* **64,** 2108–2110 (1994).

59. Brendel, R. Review of Layer Transfer Processes for Crystalline Thin-Film Silicon Solar Cells. *Jpn. J. Appl. Phys.* **40,** 4431–4439 (2001).

60. Müller, G., Friedberger, A. & Knese, K. in *Handbook of Silicon Based MEMS Materials and Technologies* 409–431 (William Andrew Publishing, 2010).

61. Low, S. P. & Voelcker, N. H. in *Handbook of Porous Silicon* (ed. Canham, L.) 381–393 (Springer International Publishing, 2014).

62. Anglin, E. J., Cheng, L., Freeman, W. R. & Sailor, M. J. Porous silicon in drug delivery devices and materials. *Adv. Drug Deliv. Rev.* **60,** 1266–1277 (2008).

63. Salonen, J., Kaukonen, A. M., Hirvonen, J. & Lehto, V.-P. Mesoporous Silicon in Drug Delivery Applications. *J. Pharm. Sci.* **97,** 632–653 (2008).

64. Sun, W., Puzas, J. E., Sheu, T.-J., Liu, X. & Fauchet, P. M. Nano- to Microscale Porous Silicon as a Cell Interface for Bone-Tissue Engineering. *Adv. Mater.* **19,** 921–924 (2007).

65. Low, S. P., Voelcker, N. H., Canham, L. T. & Williams, K. A. The biocompatibility of porous silicon in tissues of the eye. *Biomaterials* **30,** 2873–2880 (2009).

66. Kang, S.-K. *et al.* Bioresorbable silicon electronic sensors for the brain. *Nature* **530,** 71–76 (2016).

67. Sailor, M. J. & Link, J. R. 'Smart dust': nanostructured devices in a grain of sand. *Chem. Commun.* 1375–1383 (2005). doi:10.1039/B417554A

68. Sailor, M. J. *Porous Silicon in Practice*. (Wiley-VCH Verlag GmbH & Co. KGaA, 2011).

69. Canham, L. *Handbook of Porous Silicon*. (Springer International Publishing, 2014).

70. Yablonovitch, E. Inhibited Spontaneous Emission in Solid-State Physics and Electronics. *Phys. Rev. Lett.* **58,** 2059–2062 (1987).

71. Arsenault, A. C., Puzzo, D. P., Manners, I. & Ozin, G. A. Photonic-crystal full-colour displays. *Nat. Photonics* **1,** 468–472 (2007).

72. Fan, S. & Joannopoulos, J. D. Analysis of guided resonances in photonic crystal slabs. *Phys. Rev. B* **65,** 235112 (2002).

73. Brown, E. R., Yablonovitch, E. & Parker, C. D. Radiation properties of a planar antenna on a photonic-crystal substrate. *J. Opt. Soc. Am. B* **10,** 404–407 (1993).

74. López, C. Materials Aspects of Photonic Crystals. *Adv. Mater.* **15,** 1679–1704 (2003).

75. Joannopoulos, J. D., Johnson, S. G., Winn, J. N. & Meade, R. D. *Photonic Crystals: Molding the Flow of Light*. (Princeton University Press, 2008).

76. John, S. Strong localization of photons in certain disordered dielectric superlattices. *Phys. Rev. Lett.* **58,** 2486–2489 (1987).

77. Iga, K., Koyama, F. & Kinoshita, S. Surface emitting semiconductor lasers. *IEEE J. Quantum Electron.* **24,** 1845–1855 (1988).

78. Iga, K. Surface-emitting laser-its birth and generation of new optoelectronics field. *IEEE J. Sel. Top. Quantum Electron.* **6,** 1201–1215 (2000).

79. Kogelnik, H. & Shank, C. V. Coupled-Wave Theory of Distributed Feedback Lasers. *J. Appl. Phys.* **43,** 2327–2335 (1972).

80. Yablonovitch, E. *et al.* Donor and acceptor modes in photonic band structure. *Phys. Rev. Lett.* **67,** 3380–3383 (1991).

81. Braun, P. V., Rinne, S. A. & García-Santamaría, F. Introducing Defects in 3D Photonic Crystals: State of the Art. *Adv. Mater.* **18,** 2665–2678 (2006).

82. Arsenault, A. *et al.* Perfecting Imperfection—Designer Defects in Colloidal Photonic Crystals. *Adv. Mater.* **18,** 2779–2785 (2006).

83. Birks, T. A., Knight, J. C. & Russell, P. S. J. Endlessly single-mode photonic crystal fiber. *Opt. Lett.* **22,** 961–963 (1997).

84. Paschotta, R. *Field Guide to Lasers*. (SPIE Press, 2008).

85. Leonhardt, U. Optical Conformal Mapping. *Science* **312,** 1777–1780 (2006).

86. Pendry, J. B., Schurig, D. & Smith, D. R. Controlling Electromagnetic Fields. *Science* **312,** 1780–1782 (2006).

87. Kundtz, N. B., Smith, D. R. & Pendry, J. B. Electromagnetic Design With Transformation Optics. *Proc. IEEE* **99,** 1622–1633 (2011).

88. Schurig, D., Pendry, J. B. & Smith, D. R. Calculation of material properties and ray tracing in transformation media. *Opt. Express* **14,** 9794 (2006).

89. Leonhardt, U. & Philbin, T. G. General relativity in electrical engineering. *New J. Phys.* **8,** 247 (2006).

90. Valentine, J., Li, J., Zentgraf, T., Bartal, G. & Zhang, X. An optical cloak made of dielectrics. *Nat. Mater.* **8,** 568–571 (2009).

91. Cai, W., Chettiar, U. K., Kildishev, A. V. & Shalaev, V. M. Optical cloaking with metamaterials. *Nat. Photonics* **1,** 224–227 (2007).

92. Ergin, T., Stenger, N., Brenner, P., Pendry, J. B. & Wegener, M. Three-Dimensional Invisibility Cloak at Optical Wavelengths. *Science* **328,** 337–339 (2010).

93. Polman, A. & Atwater, H. A. Photonic design principles for ultrahigh-efficiency photovoltaics. *Nat. Mater.* **11,** 174–177 (2012).

94. Chen, H., Chan, C. T. & Sheng, P. Transformation optics and metamaterials. *Nat. Mater.* **9,** 387–396 (2010).

95. Li, J. & Pendry, J. B. Hiding under the Carpet: A New Strategy for Cloaking. *Phys. Rev. Lett.* **101,** 203901 (2008).

96. Landy, N. I., Kundtz, N. & Smith, D. R. Designing Three-Dimensional Transformation Optical Media Using Quasiconformal Coordinate Transformations. *Phys. Rev. Lett.* **105,** 193902 (2010).

97. Xu, L. & Chen, H. Conformal transformation optics. *Nat. Photonics* **9,** 15–23 (2015).

98. Leonhardt, U. Notes on conformal invisibility devices. *New J. Phys.* **8,** 118 (2006).

99. Leonhardt, U. & Philbin, T. G. in *Progress in Optics* (ed. Wolf, E.) **53,** 69–152 (Elsevier, 2009).

100. Olshansky, R. & Keck, D. B. Pulse broadening in graded-index optical fibers. *Appl. Opt.* **15,** 483 (1976).

101. Moore, D. T. Gradient-index optics: a review. *Appl. Opt.* **19,** 1035–1038 (1980).

102. Di Falco, A., Kehr, S. C. & Leonhardt, U. Luneburg lens in silicon photonics. *Opt. Express* **19,** 5156–5162 (2011).

103. Wood, R. W. *Physical optics*. (New York : The Macmillan Company, 1905).

104. Murayama, M. & Larkum, M. E. In vivo dendritic calcium imaging with a fiberoptic periscope system. *Nat. Protoc.* **4,** 1551–1559 (2009).

105. Kawazu, M. & Ogura, Y. Application of gradient-index fiber arrays to copying machines. *Appl. Opt.* **19,** 1105 (1980).

106. Spears, K. & Harris, R. Compact integrated optical imaging assembly. (2004).

107. Hashizume, H., Hamanaka, K., Graham III, A. C. & Zhu, X. F. Future of gradient index optics. in *Proc. SPIE* **4437,** 26–39 (2001).

108. Bentley, Julie L. Integration of the Design and Manufacture of Gradient-Index Optical Systems. (University of Rochester, 1995).

109. Gabrielli, L. H. & Lipson, M. Integrated Luneburg lens via ultra-strong index gradient on silicon. *Opt. Express* **19,** 20122–20127 (2011).

110. Spadoti, D. H., Gabrielli, L. H., Poitras, C. B. & Lipson, M. Focusing light in a curved-space. *Opt. Express* **18,** 3181–3186 (2010).

CHAPTER 2

TRANSFER-PRINTING OF TUNABLE POROUS SILICON MICROCAVITIES WITH EMBEDDED LIGHT EMITTERS[*]

2.1 Introduction and Motivation

Porous silicon (PSi) is formed by electrochemically etching silicon (Si) in a hydrofluoric acid-based electrolyte, with the resultant porosity (i.e., void fraction) determined by the applied current density, etch solution chemistry, and silicon doping[2]. This material first drew considerable attention for its visible photoluminescence at room temperature[3,4] leading to consideration of Si-based light sources for optoelectronics[5,6]. But, the research that followed was unable to advance PSi light-emitting technology to a level of performance meriting widespread implementation. PSi was, however, found to be a very versatile optical material, in particular for sensing applications[7–9], because its effective refractive index, and thus optical properties, can be modulated by foreign materials that enter the porous network[10–12]. Porosity variations induced by time-varying etching currents enable the formation of high-quality superlattices[13] with pronounced optical signatures, including high quality-factor (Q-factor) microcavities[14,15] with the potential to function as resonant cavities for lasers[16].

The versatility and optical properties of PSi microcavities, coupled with highly efficient emitters, may provide a new platform for realizing the strong light emission manipulation required for lasers[17], displays[18], and quantum information processing[19,20]. However, to date, emission modification efforts using PSi microcavities have relied heavily on the limited scope of emitters that can either be embedded into the mesoporous structure[21–26] or implanted into the Si wafer used

---

[*] Content in this chapter was previously published by the author and reproduced with permission[1]

to fabricate the PSi[27]. While these efforts have shown promise, lack of spatial control of the emitter distribution may lead to fluorescence quenching due to energy transfer among the emitters, or between the emitters and the PSi surface[28–30]. Fabrication of hybrid structures comprised of a well-defined, high-quality emitting cavity layer introduced between a top and bottom PSi distributed Bragg reflector (DBR) can address the above issues, potentially bridging the gap between PSi photonics and optoelectronic devices. Prior to the work here, realization of PSi hybrid microcavities has been hindered by difficulties in transferring fragile PSi films from a donor substrate to an acceptor substrate without damage. Methods of assembling PSi photonic devices have been proposed, including dry-removal lithography[31] and biofunctionalization-driven self-assembly[32]. However, these techniques have been geared towards the formation of PSi-based sensing arrays that lack the optical properties required for emission modification[33,34]. Recently, approaches based on transfer-printing have successfully enabled a broad variety of heterogeneously integrated optoelectronic and photonic systems[35–38]. In these methods, the kinetically controlled adhesion between the elastomeric stamp and the object to be transferred allows for high-quality assemblies over a large area.

Here, we demonstrate that high-quality PSi hybrid microcavities can easily be constructed using a modified transfer-printing technique, enabling strongly controlled emission from any variety of emitters, from quantum dots to solid-state thin-films. By introducing a PSi cavity coupling layer in addition to the PSi DBR mirrors, the hybrid microcavity resonance can be both globally tuned and spatially modulated.

2.2 Printing hybrid porous silicon microcavities

Transfer-printing assembly is a pick-and-place method that uses an elastomeric stamp, commonly polydimethylsiloxane (PDMS), as the carrier element[36]. Our initial efforts to transferprint free-standing PSi were unsuccessful due to the strong adhesion of PSi to the PDMS stamp, making damage-free transfer of the PSi film to a new substrate in an optically flat, planar configuration difficult. The adhesion strength was decreased by a standard silanization procedure[39,40] to the surface of the PDMS stamp. The treated stamp still offers sufficient viscoelasticity[36] to enable successful retrieval and printing of a free-standing PSi DBR film (**Figure 2.1**).

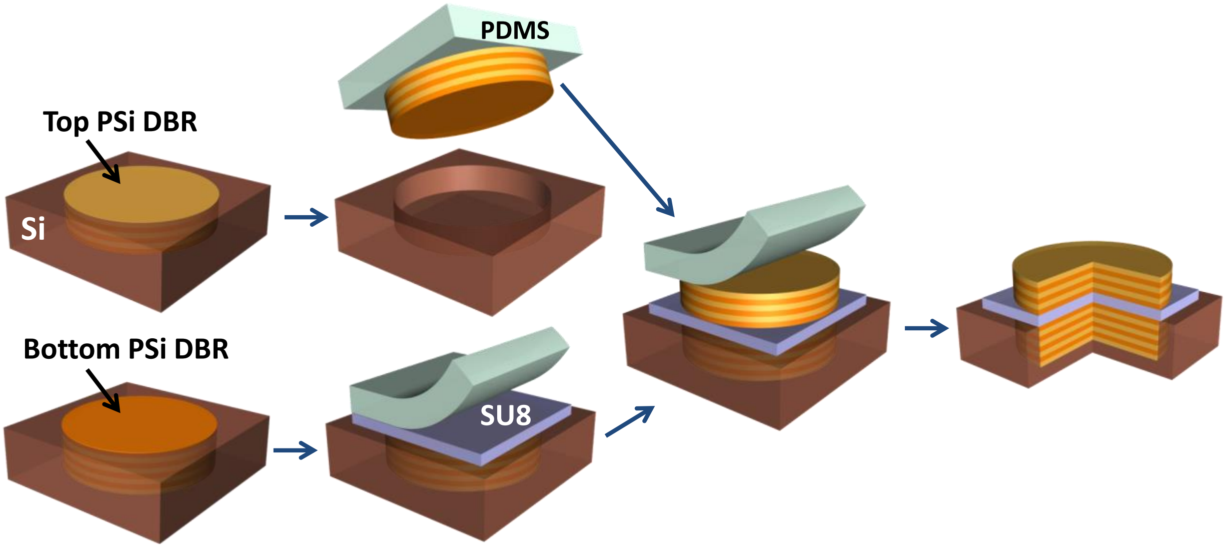

Figure 2.1. Schematic illustrating the general process flow for the assembly of PSi-based hybrid microcavities. The process features sequential printings of SU-8 photoresist and a free-standing PSi DBR atop an as-fabricated PSi DBR. The result is a PSi/polymer hybrid microcavity with the cross-sectional structure depicted at the right.

A $\frac{\lambda}{2}$ PSi-based hybrid microcavity was constructed by assembling a PSi/polymer hybrid (**Figure 2.1**). The polymer, an ~500 nm thick SU-8 photoresist film, was printed onto a PSi DBR consisting of 15 pairs of alternating high (~2.4) and low (~1.7) refractive index layers (**Figure 2.2a, b**). Next, another PSi DBR with the same index contrast, but only 11 lattice periods, and thus slightly lower in reflectance, is transfer-printed onto the SU-8 cavity layer (**Figure 2.2c, d**). **Figure**

2.2e displays a cross-section of such a hybrid microcavity, showing that the printed SU-8 layer forms smooth, distinct interfaces with the PSi.

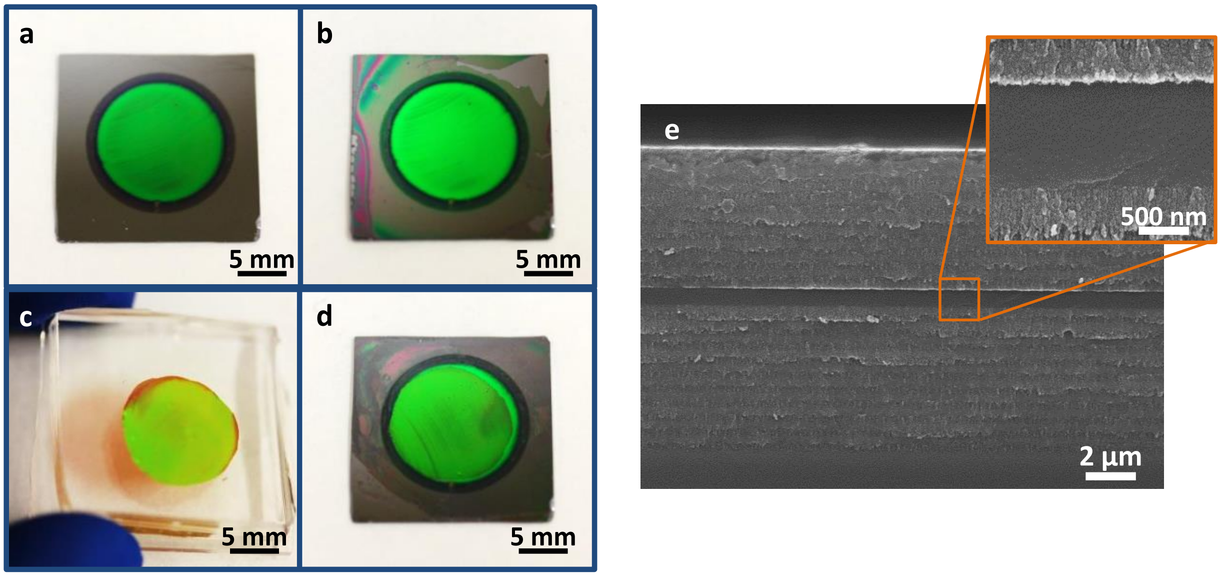

Figure 2.2. (a-d) Optical micrographs displaying the top view of the PSi/polymer hybrid microcavity at different stages of the assembly process shown in Figure 8 including (a) the as-fabricated PSi DBR (green region), (b) after printing an SU-8 polymer film atop the PSi DBR and the surrounding Si substrate, (c) after picking up a detached PSi DBR with a silane-treated PDMS stamp, and (d) the final PSi/polymer/PSi sandwich structure. (e) SEM image of a cross-section of the final PSi/polymer hybrid structure, (inset) higher magnification SEM image focusing on the cavity layer showing the high quality of the interfaces.

The hybrid microcavity is characterized by its reflectance spectrum (**Figure 2.3a**) and a sharp (average full-width at half-maximum (FWHM) = 2.1 nm) cavity mode near the center (1500 nm) of the 300 nm wide DBR stop band is observed. Compared to a monolithically etched PSi microcavity with a similar refractive index profile (**Figure 2.3b**), the cavity mode of the printed microcavity is only 0.3 nm wider. The small broadening in the linewidth relative to the monolithic structure is perhaps caused by thickness variations of the SU-8 cavity layer over the measurement spot. **Figure 2.3c** shows the measured cavity mode and mode linewidth across a 9 mm line of the printed SU-8 cavity. The small deviations in mode position (~6.8 nm) and linewidth (~0.3 nm) demonstrate the ability of this method to assemble large-area, high-quality microcavities.

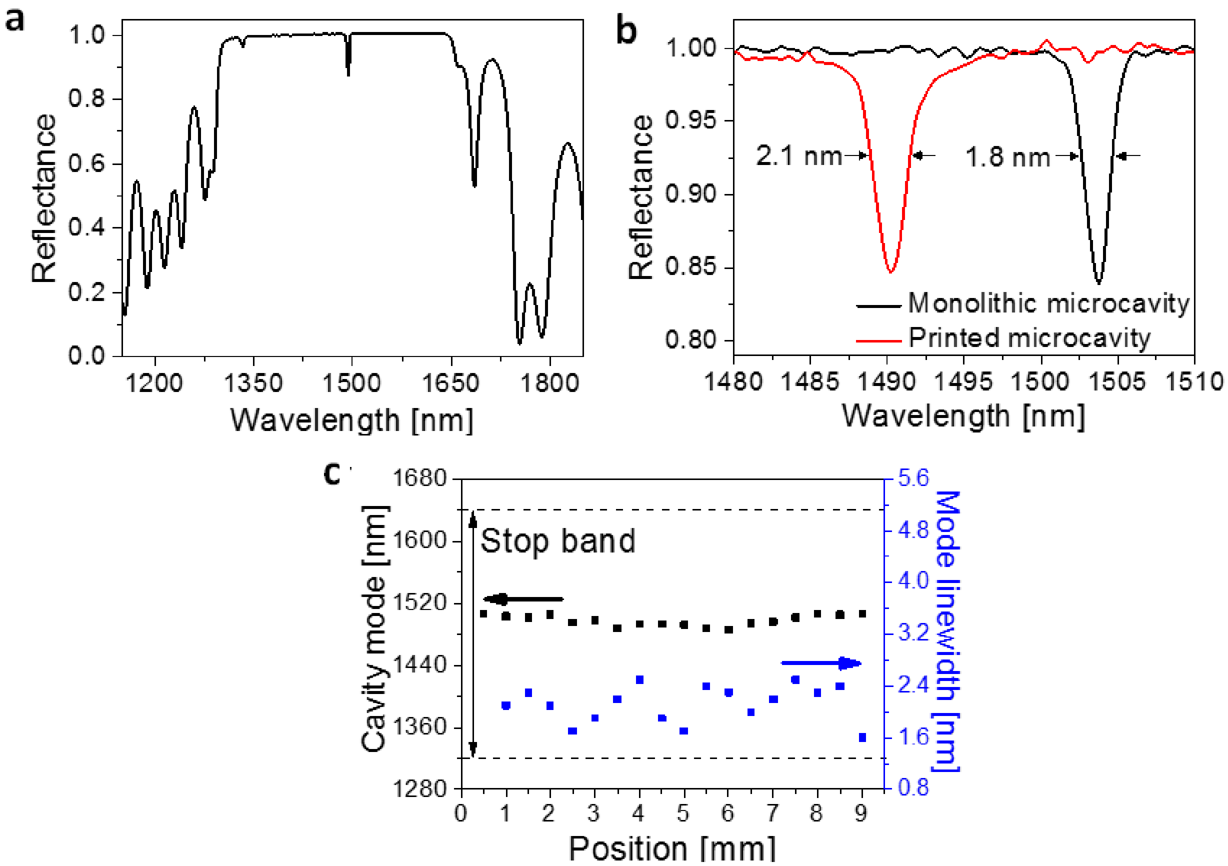

Figure 2.3. (a) Optical reflectance spectrum of the PSi/polymer hybrid microcavity exhibiting a sharp dip in the middle of the DBR stop band around 1500 nm, confirming the presence of the cavity mode. (b) Comparison of the resonant cavity mode of the printed microcavity with a monolithic PSi microcavity showing the similar optical response of the printed and monolithic devices. (c) Spectral position and linewidth of the cavity mode across the sample

2.3 Incorporating external emitters

The high optical quality of the hybrid microcavity makes it a strong candidate for controlling the emission of a light-emitter. The polymer cavity can serve as a host to any emitters that can be dispersed in a polymer matrix (e.g. organic dye molecules, colloidal quantum dots, and rare earth nanocrystals)[41,42]. As an example, a PSi/polymer microcavity is formed with PbS quantum dots (QDs) dispersed in the SU-8 cavity layer (**Figure 2.4a**). The microcavity resonance strongly influences the original, broad emission (FWHM ~100 nm) of the embedded PbS QDs (**Figure 2.4b**), significantly redistributing the emission spectrum in the normal direction to a ~2.1 nm FWHM at 1198 nm. This assembly method clearly permits the construction of high-quality structures containing spatially localized emitters in a specifically controlled chemical environment. Because formation of the emitter layer is decoupled from the assembly process, the emitters can be dispersed in a preferred matrix for controlling the physical dispersion to avoid undesirable energy transfer processes that lead to fluorescence quenching[28–30].

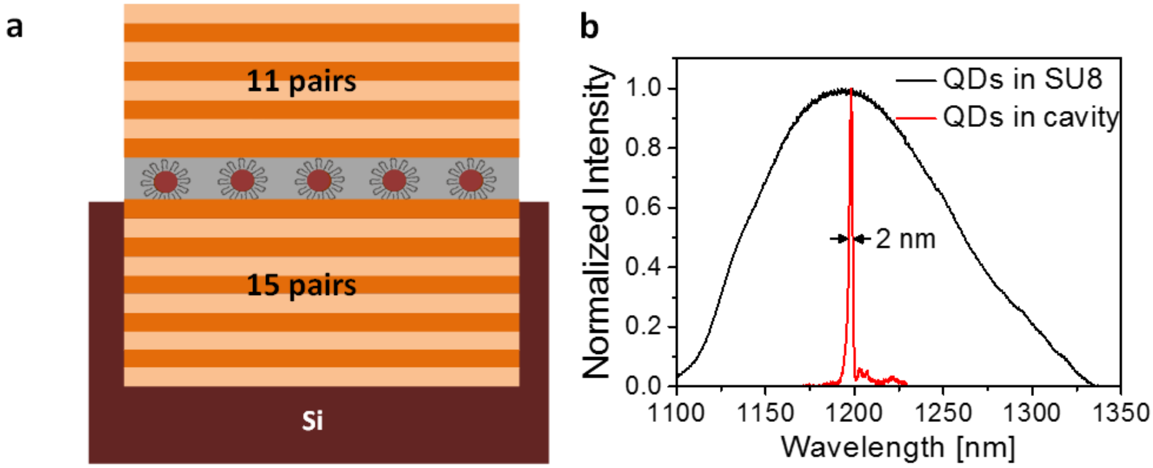

Figure 2.4. (a) Schematic of a printed PSi microcavity with a SU-8 cavity layer doped with PbS QDs. (b) Emission of SU-8 doped with PbS QDs within a hybrid cavity compared to a bare, QD-doped SU-8 film.

Another major attribute of printing-based assembly is the ease of incorporating a solid-state thin-film emitter, such as a group III-V compound semiconductor. Although promising hybrid light-emitting devices consisting of Si and group III-V semiconductors have been demonstrated[37,43–45], they primarily operate below the Si bandgap (λ > 1100 nm) to reduce the absorption loss from Si. The use of PSi can broaden the spectral range of operation, as it exhibits considerably less absorption above the Si bandgap due to the reduced absorbing volume and the increased effective electronic bandgap[46]. Here, we provide demonstration of a PSi/III-V hybrid microcavity light-emitting module that operates at energies above the Si bandgap. **Figure 2.5a** illustrates the structural layout of a hybrid microcavity featuring an ~ 1200 nm thick heterogeneous GaAs film. The interfacial SU-8 layers in the structure ensure the complete printing of both the GaAs layer and the top PSi DBR, allow control over the total cavity length, and provide extra optical confinement in the emitting layer due to their high refractive index contrast with respect to GaAs.

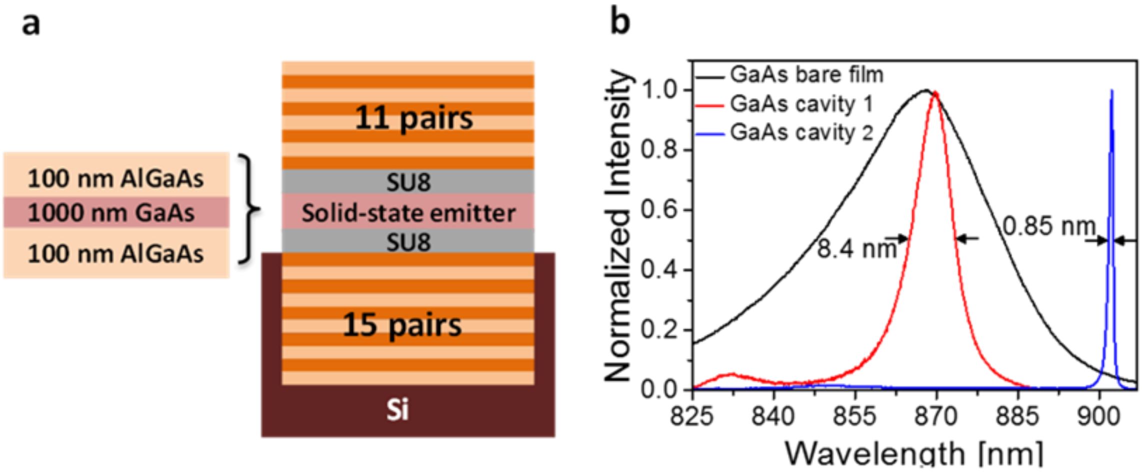

Figure 2.5. (a) Schematic of transfer-printed PSi/GaAs hybrid emitting structure. (b) Emission data from the bare GaAs structure and the GaAs structure after incorporation in two different cavities, showing a clear modification of the emission of the GaAs by the microcavity.

Figure 2.5b compares the emission spectrum of bare GaAs with those from two separate hybrid microcavities possessing different cavity lengths. The first microcavity's emission peak is near the center of the GaAs emission spectrum (FWHM ~30 nm) and features an 8.4 nm FWHM at 870 nm. The second microcavity structure is constructed with a larger SU-8 thickness that shifts the microcavity resonance to the tail of the GaAs emission spectrum. This leads to a strongly modified emission with a 0.85 nm FWHM at 902 nm, corresponding to a Q-factor ($Q = \lambda_0 / \Delta\lambda$) of

1058. Assuming no absorption in the cavity layer, the calculated mode linewidths of the two microcavities are 0.7 nm (first) and 0.5 nm (second), respectively, suggesting that the broader linewidth of the first microcavity is likely dominated by the re-absorption of emitted photons within the GaAs layer at 870 nm and not a result of the printing process or absorption by the PSi DBRs.

2.4 Microcavity resonance tuning

The ease with which the effective refractive index of PSi can be modulated not only enables the formation of microcavity structures, but also provides a simple route to cavity tuning[23,24]. To add tuning to a non-porous polymer or a solid-state cavity layer, the top and bottom DBRs are modified by introducing an additional, monolithic PSi layer above and below the cavity layer. We term this layer the cavity coupling layer (CCL), as it couples with the cavity layer to produce a resonant mode spectrally positioned at

$$m\lambda = n_1 d_1 + n_2 d_2 + n_3 d_3 \tag{2.1}$$

where m is a half-integer multiple, representing the order of the cavity mode, and $n_i d_i$ is the optical thickness of the i^{th} layer. The CCL provides a facile route to tune the resonant mode of the assembled hybrid microcavity through gradual infiltration of its mesoporous structure with a conformal deposition tool such as atomic layer deposition (ALD). **Figure 2.6a** illustrates a 2λ microcavity consisting of two CCLs and a SU-8 layer doped with PbS QDs. Al_2O_3 is deposited into the top half of the structure at 1.2 Å per ALD cycle (the solid emitter layer blocks deposition of Al_2O_3 into the bottom half of the structure).

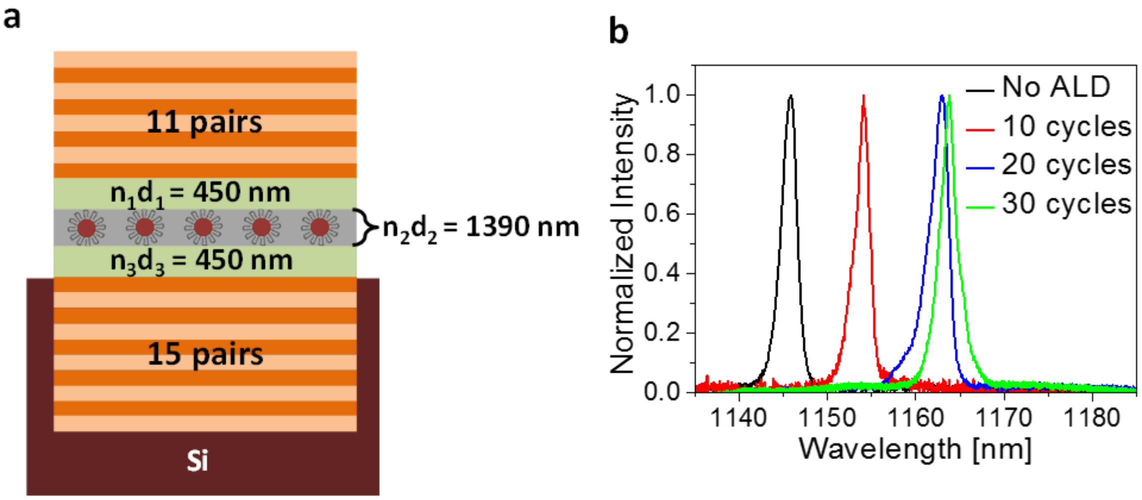

Figure 2.6. (a) Schematic of a hybrid microcavity with CCL (green) and PbS QD-doped SU-8 layer (gray with red circles). (b) Al_2O_3 ALD gradually increases the optical thickness of the PSi CCL, globally red-shifting the emission of the hybrid cavity until the porous network is pinched off (~ 20 ALD cycles).

The Al_2O_3 deposition gradually increases the CCL optical thickness, causing the position of the emission peak to red-shift ~0.9 nm per cycle from its initial position at 1145 nm. The peak eventually settles around 1163 nm after 20 cycles (**Figure 2.6b**), suggesting that the mesoporous network has undergone pinch-off.[47] Al_2O_3 infiltration of a simple 15-period DBR structure confirms that the stopband shift does not occur at the expense of the DBR photonic strength (**Figure 2.7**), and thus Al_2O_3 infiltration does not broaden or diminish the strength of the resonant mode of a microcavity structure.

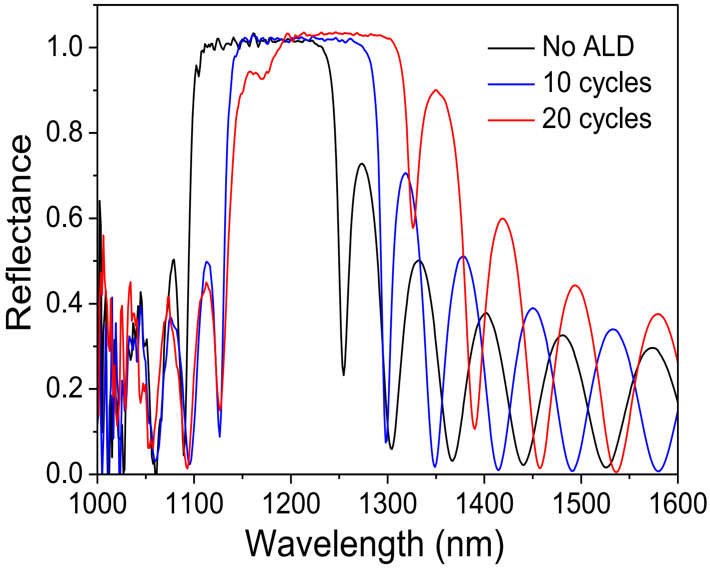

Figure 2.7. A DBR experiences a shift in its stop band position as a result of exposure to Al_2O_3 ALD. While the stop band red-shifts with Al_2O_3 ALD, the photonic strength of the mirror remains near unity.

The magnitude of this spectral shifting is linearly proportional to the product of the optical thickness fraction of CCL (i.e., CCL optical thickness relative to total cavity optical thickness) and the refractive index of the material introduced during ALD. Based upon the shift in the cavity mode position, the effective refractive index of the CCL increases from ~1.7 to ~1.83. The filling fraction of Al_2O_3 introduced can be determined with the three-component Bruggeman effective medium model[48] given by

$$0 = \emptyset_{Si}\left(\frac{n_{Si}^2 - n_{CCL}^2}{n_{Si}^2 + 2n_{CCL}^2}\right) + \emptyset_{Al_2O_3}\left(\frac{n_{Al_2O_3}^2 - n_{CCL}^2}{n_{Al_2O_3}^2 + 2n_{CCL}^2}\right) + \left(1 - \emptyset_{Si} - \emptyset_{Al_2O_3}\right)\left(\frac{1 - n_{CCL}^2}{1 + 2n_{CCL}^2}\right) \qquad \textbf{(2.2)}$$

where $\emptyset$ represents the volume fraction and n the refractive index of the indicated material components, respectively. Before filling, the porosity is calculated to be ~ 65% assuming that n_{Si} is 3.53. Further calculation determined that after pinch-off of the microcavity structure, the CCL is comprised of 14% Al_2O_3 ($n_{Al_2O_3}$ ~ 1.66) by volume. A larger tuning range could be attained either by increasing the CCL fraction (currently the top CCL accounts for 18% of the total cavity optical thickness) or by infiltrating the CCL with higher refractive index materials such as HfO_2,

TiO_2, or Si (**Figure 2.8**). While techniques such as ALD permanently shift the cavity mode, reversible tuning based on dynamic control of the infiltration may be possible. Reversible shifts in the optical response of PSi films have, for example, already been demonstrated by infiltration with various solvent vapors.[49,50]

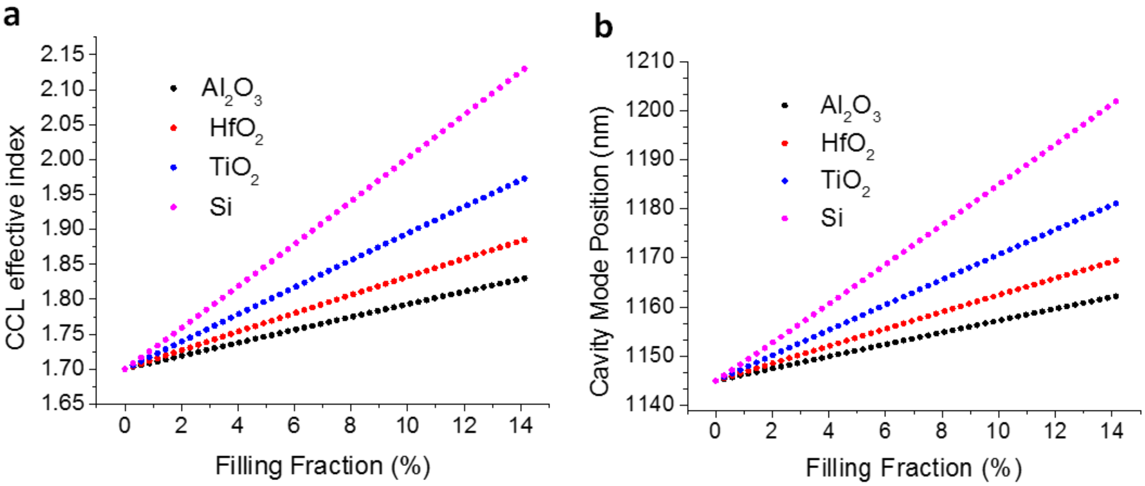

Figure 2.8. (a) The calculated evolution of a PSi CCL's effective refractive index as a function of filling fraction for the indicated materials (all of which can be deposited via ALD or CVD). (b) The calculated evolution of the spectral position of the resonant cavity mode of a PSi structure as a function of the filling fraction of the material infiltrating the CCL of the structure.

The microcavity resonance can be spatially modulated by using a CCL with a gradient optical thickness (GROT), providing spatial variation of the cavity mode. Because both the refractive index and formation rate of PSi are determined by the local current density[51], a simple GROT CCL can be produced by a spatially-varying current density that is introduced through the electrode configuration used to form the CCL[52]. Here, a Pt ring electrode that resides ~25 mm from the sample is first used to generate a uniform current density distribution during the formation of the PSi DBR. This electrode is then replaced by a Pt wire ~1 mm above the sample, giving rise to a strong radial variation in the current density that produces the GROT CCL. In this design, the PSi DBR and the GROT CCL form a continuous, monolithic structure. **Figure 2.9a** is the optical image of one such monolithic structure prior to PSi microcavity assembly. The optical thickness variation is apparent from the CCL side, as visually manifested by the interference fringes. We note that the DBR should be electrochemically etched before the GROT CCL is etched, because the spatially non-uniform formation of the GROT CCL will result in a non-uniform DBR.

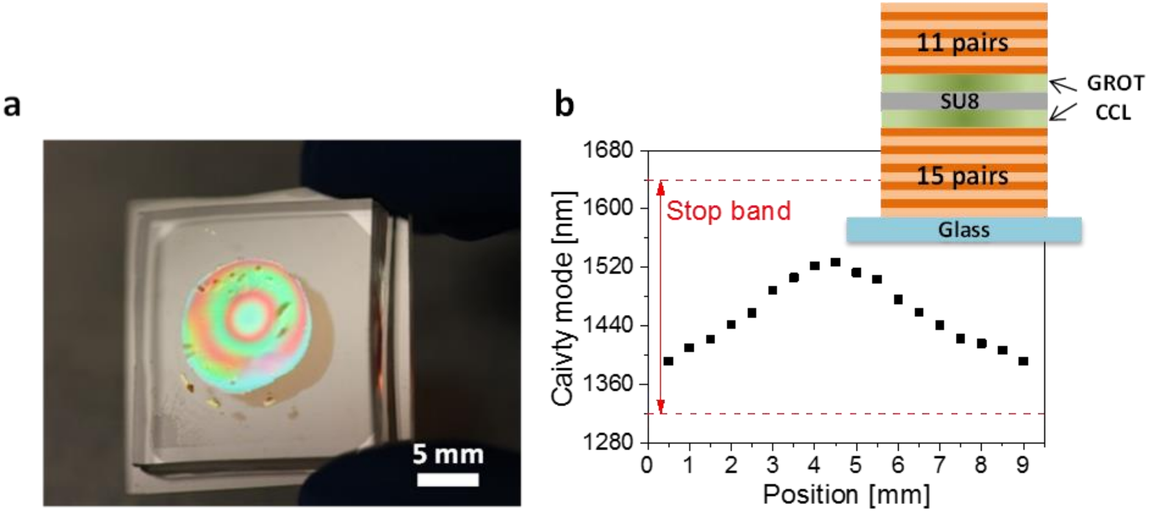

Figure 2.9. (a) Optical image of a PSi CCL formed with a GROT to spatially modulate the cavity resonance. The GROT is apparent from the appearance of the radially-symmetric fringes seen from a GROT-containing PSi CCL and underlying PSi DBR that has been retrieved with a PDMS stamp for printing. (b) Optical response of a GROT PSi CCL in a cavity configuration showing spatial modulation of the cavity resonance spectral position by ~ 140 nm. A schematic of the structure is shown in the inset.

A microcavity with symmetric GROT CCLs is fabricated on a glass substrate via double-printing (see 2.) and consists of a top DBR (11 pairs) with a GROT CCL component, a 500 nm thick SU-8 layer, and a bottom DBR (15 pairs) with a GROT CCL component (**Figure 2.9b, inset**). **Figure 2.9** shows the spatial distribution of the cavity mode across the entire sample. The two GROT CCLs have identical, radially-varying optical thickness profiles and, together with the SU-8 layer, produce a $\frac{3\lambda}{2}$ microcavity at the center of the sample. The spatial resonance modulation is designed so that the optical thickness of the microcavity decreases when moving away from the center, eventually blue-shifting the cavity mode ~140 nm from the center to the edge.

An interesting aspect of a GROT CCL is the possibility for introducing different solid-state emitters specifically designed for the local microcavity resonance where they are placed. As a simple demonstration, three separate GaAs thin film emitters are printed ~1 mm apart (**Figure 2.10a**) in a microcavity containing a GROT CCL. The emission is collected at the center of each module, which shows that the GROT CCL blue-shifts the modified emission peaks as the total cavity optical thickness decreases from module 1 to module 3 (**Figure 2.10b**).

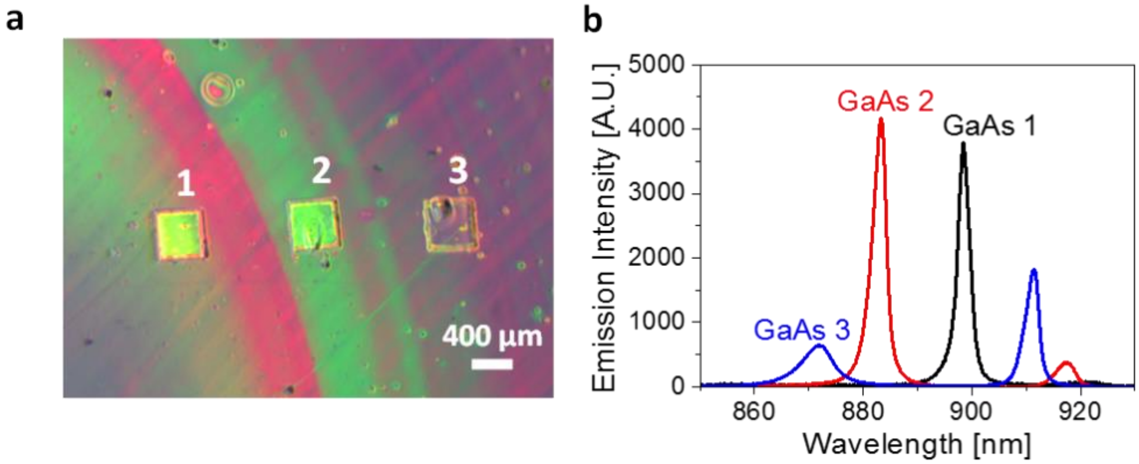

Figure 2.10. (a) Optical image of a GROT PSi CCL structure containing three distinct GaAs light emitting modules. (b) The GROT CCL spatially modulates the GaAs emission, resulting in spectrally distinct emission from each of the light emitting modules.

2.5 Conclusions

We have demonstrated that a modified transfer-printing technique enables the formation of high-quality, PSi-based hybrid microcavities compatible with several classes of light emitters. The versatility of this assembly method was demonstrated by applying it to a hybrid structure of PSi DBRs containing a PbS QD-doped polymer cavity and a PSi/III-V hybrid microcavity light-emitting module operating at energies above the bandgap of bulk Si. Using a properly designed gain medium, such as a III-V multi-quantum-well structure[37], we speculate that it may even be possible to realize coherent light sources in the 900 nm ~ 1100 nm wavelength regime using PSi hybrid microcavities. Using a PSi CCL, PSi's inherent index modulation capabilities provided a mechanism for manipulating the hybrid microcavity's resonant cavity mode and emission spectrum. Global tuning of the emission of a hybrid microcavity containing PbS QDs over a spectral range of 18 nm was possible by using Al_2O_3 ALD to infiltrate and thus change the effective optical thickness of the homogeneous CCL. The conformal, atomic-scale infiltration also offers a powerful knob to finely control the spectral shift of the resonant mode. Spatial porosity variations in the form of a GROT CCL enabled spatial resonance modulation generating three emission peaks at distinct spectral positions from each of three GaAs emitter modules located at distinct spatial positions in the hybrid microcavity. The generality of the transfer-printing method, coupled with the unique optical properties of PSi, may offer a new paradigm in the assembly of Si-based photonic architectures for optoelectronic and energy harvesting applications.

2.6 Experimental Methods

2.6.1 Porous silicon fabrication

The PSi DBR was formed from double-side polished, highly-doped ($\rho \sim 0.01\text{-}0.03\ \Omega$ cm) p-type Si (University Wafers). Etching was carried out in a polypropylene cell with an exposed etch area of ~ 1.20 cm^2. Contact to the back of the Si was established with a stainless steel electrode. Current was delivered to the cell by an SP-200 Research Grade Potentiostat/Galvanostat (Bio-Logic Science Instruments) and pulsed with a duty cycle of 33% at a frequency of 1.33 Hz (unless specified otherwise). The high (low) refractive index layer was formed using a current density of 50 (250) mA cm^{-2}, with the applied etching time varied to achieve the appropriate layer optical thickness for the designed stop band position. After etching, all samples were sequentially rinsed with ethanol and hexanes. The electrolyte was comprised of a 1:1 volume ratio of 48% hydrofluoric acid (aq) (Sigma-Aldrich) and 100% ethanol (Decon Labs). A 5 mm diameter Pt-Ir inoculating loop (Thomas Scientific) served as the counter electrode and was located at the center of the cell ~25mm from the etch surface to provide a uniform current density across the sample..

The radial GROT CCLs were formed using an electrolyte comprised of a 1:3 volume ratio of 48% hydrofluoric acid (aq) and 100% ethanol. A current density of 15 mA cm^{-2} was applied, with the Pt-Ir pin electrode placed ~1 mm from the etch surface.

Electropolishing was carried out with an electrolyte comprised of a 1:3 volume ratio of 48% hydrofluoric acid (aq) and 100% ethanol. The 5 mm Pt-Ir ring served as the counter electrode and a current density of 300 mA cm^{-2} was applied with a duty cycle of 20% at a frequency of 0.40 Hz. Before the electrochemically-induced detachment, a stainless steel syringe needle was used to mechanically score and release the edges of the PSi film to allow the film to remain flat for printing. After the electropolishing process, all samples were sequentially rinsed with ethanol and hexanes in a gentle fashion in order to avoid causing the film to be displaced on the Si substrate. Rinsing was followed by drying on a hot plate at 60°C.

2.6.2 Transfer-printing

PDMS stamps (Dow-Sylgard 184) were cast onto flat substrates and cut to dimensions 2.5 cm × 2.5 cm × 5 mm. To transfer the SU-8 film, the stamp was treated with oxygen plasma (600 mTorr, 50 W, 80 s) and subsequently spin-coated with SU-8 2000.5 (MicroChem Corp.) at 2000 rpm for 30 s. The SU-8-PDMS stamp was prebaked in a conventional oven at 65 °C for 5 min and then laminated against the receiver substrate (PSi or GaAs). To facilitate the release of SU-8 layer, both the PDMS and the receiver substrate were heated at 65 °C for 20 min, followed by slow removal of the stamp. To transfer the PSi DBR, the PDMS stamp was treated with oxygen plasma and then exposed to a fluorinated silane vapor for 1 hour. The stamp was laminated against the lifted-off PSi film and rapidly peeled away from the donor substrate. The PSi film was subsequently printed onto the receiver substrate (SU-8 film) following the above printing procedure.

2.6.3 Quantum dot/SU-8 composite

PbS core QDs (10 mg ml^{-1} in hexane) were purchased from Evident Technologies. 0.2 ml of the QDs solution was slowly added to 0.75 g 2000.5 SU-8 solution. The resulting solution was subsequently spin-casted onto an oxygen plasma-treated PDMS stamp at 2000 rpm for 30 s. The composite layer was pre-baked at 65 °C for 5 min and finally printed onto the PSi substrate following the procedure described previously.

2.6.4 Assembling symmetric microcavity with gradient optical thickness cavity-coupling layers

Because the GROT CCL is formed after the DBR etching, the bottom component must be double-printed to achieve the proper orientation. This is accomplished by first printing the detached bottom component from one PDMS stamp to another PDMS stamp, where the second stamp is subjected to a lesser silanization treatment and, therefore, possesses greater adhesion with PSi than the initial stamp. The bottom PSi component is subsequently printed onto a glass substrate with a layer of Norland Optical Adhesive (NOA), followed by sequentially printing the SU-8 layer and the top DBR with GROT CCL component

2.6.5 GaAs thin films

An AlGaAs/GaAs/AlGaAs double heterostructure (DH)[53] was formed by growth on a gallium arsenide (GaAs) substrate via metal-organic chemical vapor deposition. This was performed Dr. Chen Zhang, who was graduate student in the research group of Prof. Xiuling Li at the time. The detailed structure (from bottom to top) included the GaAs substrate, a 500 nm

$Al_{0.95}Ga_{0.05}As$ sacrificial layer, a 5 nm GaAs protection layer, a 100 nm n-$Al_{0.3}Ga_{0.7}As$ ($n = 3 \times 10^{18}$ cm^{-3}), a 1000 nm p-GaAs ($p = 5 \times 10^{17}$ cm^{-3}), a 100 nm p-$Al_{0.3}Ga_{0.7}As$ ($p = 3 \times 10^{18}$ cm^{-3}), and another 5 nm GaAs protection layer. Zn and Si served as p-type and n-type dopants, respectively. The DH devices (size 400 μm × 400 μm) were lithographically fabricated, using H_3PO_4 (85 wt% in water) / H_2O_2 (30 wt% in water) / H_2O (3:1:25) to etch the GaAs and $Al_{0.3}Ga_{0.7}As$ layers. After removing the $Al_{0.95}Ga_{0.05}As$ sacrificial layer in an ethanol-rich hydrofluoric acid (HF) solution (ethanol:HF = 1.5:1 by volume), individual DH devices were released from the GaAs wafer and then bonded onto PSi DBR by transfer-printing with a flat PDMS stamp.[54] A layer of 500 nm SU-8 acted as an adhesive to facilitate printing. Printing was performed in collaboration with Dr. Hailong Ning, a fellow graduate student in the Prof. Paul Braun's group at the time, and Prof. Xing Sheng, a former post-doctoral researcher from the research group of Prof. John Rogers.

2.6.6 Optical characterization

The reflectance spectrum was collected by a Bruker 70 FTIR system with a 4 X objective and 1.8 mm aperture at the image plane, corresponding to a 200 μm field of view. Both PbS QDs and the GaAs thin films were excited by a 785 nm continuous wave laser diode. The emission of PbS QDs was recorded by a home-made system with a 4X objective and a NIR CCD detector (Horiba, Symphony). The emission of GaAs was measured by a Horiba confocal Raman imaging microscope with a 4X objective and a 200 μm aperture. PbS QD and GaAs characterization were performed in collaboration with Dr. Hailong Ning.

2.7 References

1. Ning, H. *et al.* Transfer-Printing of Tunable Porous Silicon Microcavities with Embedded Emitters. *ACS Photonics* **1,** 1144–1150 (2014).

2. Gal, M., Reece, P. J., Zheng, W. & Lerondel, G. Porous silicon: a versatile optical material. in *Proc. SPIE* **5277,** 9–16 (2004).

3. Canham, L. T. Silicon quantum wire array fabrication by electrochemical and chemical dissolution of wafers. *Appl. Phys. Lett.* **57,** 1046–1048 (1990).

4. Cullis, A. G. & Canham, L. T. Visible light emission due to quantum size effects in highly porous crystalline silicon. *Nature* **353,** 335–338 (1991).

5. Canham, L. Gaining light from silicon. *Nature* **408,** 411–412 (2000).

6. Collins, R. T., Fauchet, P. M. & Tischler, M. A. Porous Silicon: From Luminescence to LEDs. *Phys. Today* **50,** 24–31 (2008).

7. Korotcenkov, G. & Cho, B. K. Porous Semiconductors: Advanced Material for Gas Sensor Applications. *Crit. Rev. Solid State Mater. Sci.* **35,** 1–37 (2010).

8. Rong, G., Najmaie, A., Sipe, J. E. & Weiss, S. M. Nanoscale porous silicon waveguide for label-free DNA sensing. *Biosens. Bioelectron.* **23,** 1572–1576 (2008).

9. Rong, G., Ryckman, J. D., Mernaugh, R. L. & Weiss, S. M. Label-free porous silicon membrane waveguide for DNA sensing. *Appl. Phys. Lett.* **93,** 161109 (2008).

10. Anderson, M. A. *et al.* Sensitivity of the optical properties of porous silicon layers to the refractive index of liquid in the pores. *Phys. Status Solidi A* **197,** 528–533 (2003).

11. Chan, S., Fauchet, P. M., Li, Y., Rothberg, L. J. & Miller, B. L. Porous Silicon Microcavities for Biosensing Applications. *Phys. Status Solidi A* **182,** 541–546 (2000).

12. Mulloni, V. & Pavesi, L. Porous silicon microcavities as optical chemical sensors. *Appl. Phys. Lett.* **76,** 2523–2525 (2000).

13. Frohnhoff, S. & Berger, M. G. Porous silicon superlattices. *Adv. Mater.* **6,** 963–965 (1994).

14. Ghulinyan, M., Oton, C. J., Bonetti, G., Gaburro, Z. & Pavesi, L. Free-standing porous silicon single and multiple optical cavities. *J. Appl. Phys.* **93,** 9724–9729 (2003).
15. Reece, P. J., Lérondel, G., Zheng, W. H. & Gal, M. Optical microcavities with subnanometer linewidths based on porous silicon. *Appl. Phys. Lett.* **81,** 4895–4897 (2002).
16. Zheng, W. H., Reece, P., Sun, B. Q. & Gal, M. Broadband laser mirrors made from porous silicon. *Appl. Phys. Lett.* **84,** 3519–3521 (2004).
17. Yablonovitch, E. Inhibited Spontaneous Emission in Solid-State Physics and Electronics. *Phys. Rev. Lett.* **58,** 2059–2062 (1987).
18. Schubert, E. F. & Kim, J. K. Solid-State Light Sources Getting Smart. *Science* **308,** 1274–1278 (2005).
19. Khitrova, G., Gibbs, H. M., Kira, M., Koch, S. W. & Scherer, A. Vacuum Rabi splitting in semiconductors. *Nat. Phys.* **2,** 81–90 (2006).
20. Strauf, S. Quantum optics: Towards efficient quantum sources. *Nat. Photonics* **4,** 132–134 (2010).
21. Venturello, A. *et al.* Controlled light emission from dye-impregnated porous silicon microcavities. *J. Non-Cryst. Solids* **352,** 1230–1233 (2006).
22. Dwivedi, V. K., Pradeesh, K. & Vijaya Prakash, G. Controlled emission from dye saturated single and coupled microcavities. *Appl. Surf. Sci.* **257,** 3468–3472 (2011).
23. Qiao, H. *et al.* Optical properties of II-VI colloidal quantum dot doped porous silicon microcavities. *Appl. Phys. Lett.* **96,** 161106 (2010).

24. Weiss, S. M., Zhang, J., Fauchet, P. M., Seregin, V. V. & Coffer, J. L. Tunable silicon-based light sources using erbium doped liquid crystals. *Appl. Phys. Lett.* **90,** 031112 (2007).

25. DeLouise, L. A. & Ouyang, H. Photoinduced fluorescence enhancement and energy transfer effects of quantum dots porous silicon. *Phys. Status Solidi C* **6,** 1729–1735 (2009).

26. Jenie, S. N. A. *et al.* Lanthanide Luminescence Enhancements in Porous Silicon Resonant Microcavities. *ACS Appl. Mater. Interfaces* (2014). doi:10.1021/am500983r

27. Reece, P. J., Gal, M., Tan, H. H. & Jagadish, C. Optical properties of erbium-implanted porous silicon microcavities. *Appl. Phys. Lett.* **85,** 3363–3365 (2004).

28. Tan, M. C. *et al.* Synthesis and optical properties of infrared-emitting YF3:Nd nanoparticles. *J. Appl. Phys.* **106,** 063118 (2009).

29. Rinnerbauer, V. *et al.* Energy transfer in close-packed PbS nanocrystal films. *Phys. Rev. B* **77,** 085322 (2008).

30. Clegg, R. M. Fluorescence resonance energy transfer. *Curr. Opin. Biotechnol.* **6,** 103–110 (1995).

31. Sirbuly, D. J., Lowman, G. M., Scott, B., Stucky, G. D. & Buratto, S. K. Patterned Microstructures of Porous Silicon by Dry-Removal Soft Lithography. *Adv. Mater.* **15,** 149–152 (2003).

32. Böcking, T. *et al.* Biofunctionalization of free-standing porous silicon films for self-assembly of photonic devices. *Soft Matter* **8,** 360–366 (2011).

33. Böcking, T. *et al.* Substrate Independent Assembly of Optical Structures Guided by Biomolecular Interactions. *ACS Appl. Mater. Interfaces* **2,** 3270–3275 (2010).

34. Gargas, D. J., Muresan, O., Sirbuly, D. J. & Buratto, S. K. Micropatterned Porous-Silicon Bragg Mirrors by Dry-Removal Soft Lithography. *Adv. Mater.* **18,** 3164–3168 (2006).

35. Kim, S. *et al.* Microstructured elastomeric surfaces with reversible adhesion and examples of their use in deterministic assembly by transfer printing. *Proc. Natl. Acad. Sci. USA* **107,** 17095–17100 (2010).

36. Meitl, M. A. *et al.* Transfer printing by kinetic control of adhesion to an elastomeric stamp. *Nat. Mater.* **5,** 33–38 (2006).

37. Yang, H. *et al.* Transfer-printed stacked nanomembrane lasers on silicon. *Nat. Photonics* **6,** 615–620 (2012).

38. Justice, J. *et al.* Wafer-scale integration of group III-V lasers on silicon using transfer printing of epitaxial layers. *Nat. Photonics* **6,** 610–614 (2012).

39. Xia, Y. & Whitesides, G. M. Soft Lithography. *Annu. Rev. Mater. Sci.* **28,** 153 (1998).

40. Qin, D., Xia, Y. & Whitesides, G. M. Soft lithography for micro- and nanoscale patterning. *Nat. Protoc.* **5,** 491–502 (2010).

41. Stouwdam, J. W. & van Veggel, F. C. J. M. Near-infrared Emission of Redispersible Er3+, Nd3+, and Ho3+ Doped LaF3 Nanoparticles. *Nano Lett.* **2,** 733–737 (2002).

42. Ning, H., Mihi, A., Geddes, J. B., Miyake, M. & Braun, P. V. Radiative Lifetime Modification of LaF3:Nd Nanoparticles Embedded in 3D Silicon Photonic Crystals. *Adv. Mater.* **24,** OP153–OP158 (2012).

43. Lee, A., Liu, H. & Seeds, A. Semiconductor III–V lasers monolithically grown on Si substrates. *Semicond. Sci. Technol.* **28,** 015027 (2013).

44. Park, H., Fang, A., Kodama, S. & Bowers, J. Hybrid silicon evanescent laser fabricated with a silicon waveguide and III-V offset quantum wells. *Opt. Express* **13,** 9460–9464 (2005).

45. Fang, A. W. *et al.* A continuous-wave hybrid AlGaInAs-silicon evanescent laser. *IEEE Photonics Technol. Lett.* **18,** 1143–1145 (2006).

46. Datta, S. & Narasimhan, K. L. Model for optical absorption in porous silicon. *Phys. Rev. B* **60,** 8246–8252 (1999).

47. Brzezinski, A., Chen, Y.-C., Wiltzius, P. & Braun, P. V. Complex three-dimensional conformal surfaces formed by atomic layer deposition: computation and experimental verification. *J. Mater. Chem.* **19,** 9126–9130 (2009).

48. Bosch, S., Ferré-Borrull, J., Leinfellner, N. & Canillas, A. Effective dielectric function of mixtures of three or more materials: a numerical procedure for computations. *Surf. Sci.* **453,** 9–17 (2000).

49. Bjorklund, R. B., Zangooie, S. & Arwin, H. Color changes in thin porous silicon films caused by vapor exposure. *Appl. Phys. Lett.* **69,** 3001–3003 (1996).

50. Bjorklund, R. B., Zangooie, S. & Arwin, H. Planar pore-filling — adsorption in porous silicon. *Adv. Mater.* **9,** 1067–1070 (1997).

51. Ilyas, S. & Gal, M. Single and multi-array GRIN lenses from porous silicon. in *2006 Conference on Optoelectronic and Microelectronic Materials and Devices* 245–248 (2006). doi:10.1109/COMMAD.2006.4429927

52. Collins, B. E., Dancil, K.-P. S., Abbi, G. & Sailor, M. J. Determining Protein Size Using an Electrochemically Machined Pore Gradient in Silicon. *Adv. Funct. Mater.* **12,** 187–191 (2002).

53. Schnitzer, I., Yablonovitch, E., Caneau, C. & Gmitter, T. J. Ultrahigh spontaneous emission quantum efficiency, 99.7% internally and 72% externally, from AlGaAs/GaAs/AlGaAs double heterostructures. *Appl. Phys. Lett.* **62,** 131–133 (1993).

54. Carlson, A., Bowen, A. M., Huang, Y., Nuzzo, R. G. & Rogers, J. A. Transfer Printing Techniques for Materials Assembly and Micro/Nanodevice Fabrication. *Adv. Mater.* **24,** 5284–5318 (2012).

CHAPTER 3

SHAPE-DEFINED FORMATION OF POROUS SILICON GRADIENT REFRACTIVE INDEX SQUARE MICROLENSES

3.1 Introduction and Motivation

Gradient refractive index (GRIN) elements possess spatially-varying refractive indices, endowing them with the ability to send light along curvilinear optical paths, as Fermat's principle explains, because light travels stationary, extremal trajectories within optically inhomogeneous media[1]. This behavior enables powerful optical elements such as Luneburg lenses, which are devoid of geometrical aberrations and offer high efficiency fiber-to-chip coupling[2–4]. Other designer GRINs are embodied by elements decoupling physical geometry and optical function, such as carpet cloaks[5,6] and flat lenses[7]. Flat lenses, particularly flat, Si-based microlenses, are attractive for compact, on-chip optics within the framework of integrated Si photonics[7]. Additionally, the presence of coupled birefringent/GRIN effects provide an opportunity for a GRIN element to perform distinct, polarization-selective operations[8]. However, to date, conventional processing has confined Si-based GRIN elements to thin, 2D geometries[2–7].

Porous silicon (PSi) was initially studied due to its visible luminescence at room temperature[9,10]. While PSi has not displaced current emitter technologies, it has established an identity as a versatile optical material[11], as its nanoscale porosity (and thus refractive index) can be modulated during its electrochemical fabrication[12,13]. During fabrication, a time-varying etch current density results in a porosity (and thus refractive index) gradient along the etch pathway. This effect has most notably been used to form 1D optical superlattices[14,15] that can be exploited as chemical sensors[16–19]. Refractive index modulation in 2D or 3D as required for a GRIN element, however, is more difficult in that it requires a spatially-varying current density. This can be accomplished by using shaped electrodes[20], but the approach is limited in that the etch rate of PSi also varies with current density[21,22], making flat elements unattainable. Additionally, current spreading in the substrate and electrolyte prevent sharp GRIN variations like those that can be achieved with a time-varying current density. Photo-mediated etching offers an attractive route to arbitrary 2D PSi GRIN structures[23], but is restricted to thin (e.g., 2-3 µm) structures due to optical absorption in the PSi.

Here, we fabricate 3D birefringent GRIN micro-optics by electrochemically etching preformed Si microstructures (e.g., square micro-columns) into porous Si (PSi) structures with defined refractive index profiles. These elements perform novel, polarization-dependent optical functions, including splitting and focusing, expanding the use of PSi for a wide range of integrated photonics applications.

3.2 Shape-defined porous silicon formation

We suggest that a versatile approach to 3D GRIN elements is to use a defined Si topography to serve as the starting point for the lateral etch required to form a GRIN profile. Now, a time-varying current density generates the GRIN along the PSi etch pathway that initiates at all unmasked Si/electrolyte interfaces (**Figure 3.1a**). While non-planar electrochemical processing has been shown for Si[24,25] and Ge[26], the previous work only utilized the shape-defined etch pathway to form conventional optical superlattices.

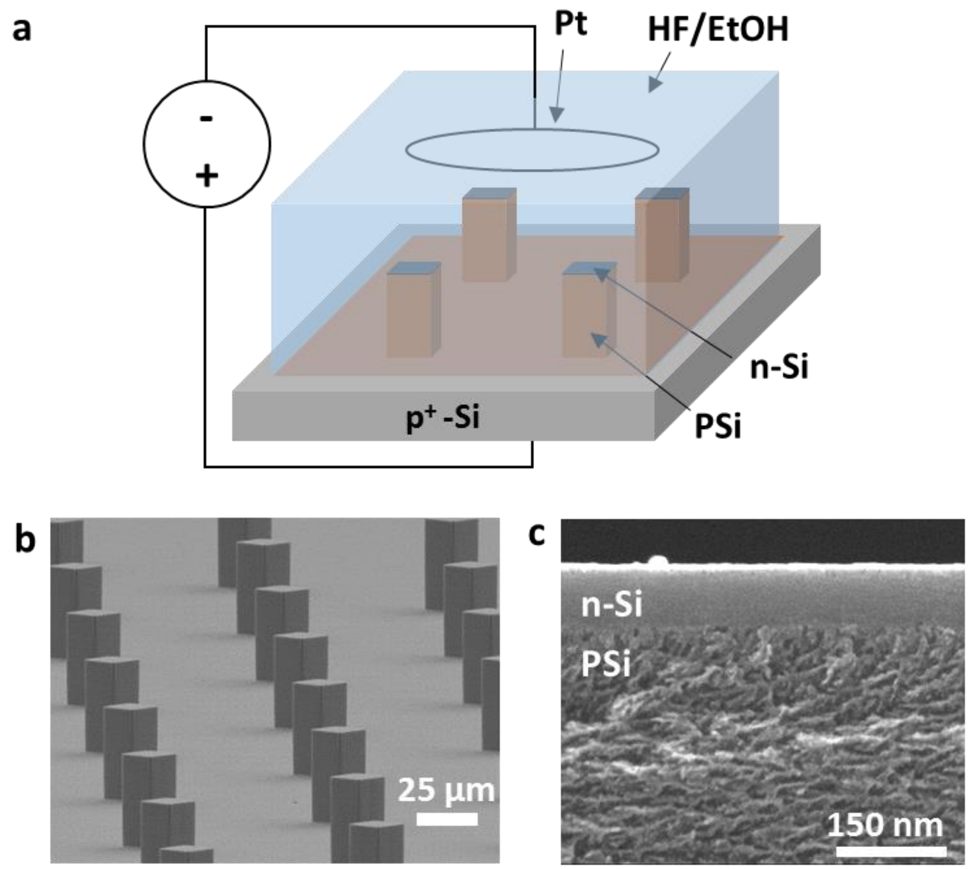

Figure 3.1. (a) Schematic outlining the process by which p-type Si SMCs with n-type caps undergo shape-defined electrochemical etching to endow them with nanoscale porosity that defines the local refractive index. (b) SEM image of a section of an array of Si SMCs subjected to shape-defined PSi formation. (c) SEM cross-section at the top of an etched feature showing how PSi formation proceeds beneath the n-type cap.

Our process begins with a p^+-type Si wafer doped to form a shallow (~100 nm) n-type surface. Photolithography, followed by deep reactive ion etching, generates an array of microscale elements (e.g., square micro-columns (SMCs)) across the wafer (**Figure 3.1b**). Electrochemical etching simultaneously converts all of the elements to PSi in a few minutes. The n-type cap restricts PSi formation[27] to the sidewalls, resulting in an etch path and GRIN profile that runs inward from and perpendicular to each of the SMC sidewalls (**Figure 3.1c**). Changes in the current density, whether discrete or continuous, provide nearly arbitrary refractive index control within the limits determined available for PSi (**Figure 3.2**).

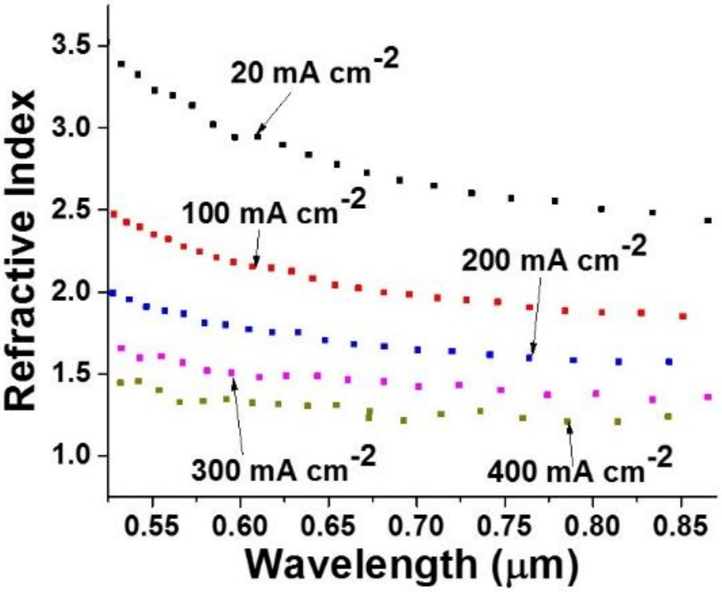

Figure 3.2. Dispersion curves associated with PSi fabricated at different current densities as determined by reflectance spectroscopy of thin films on bulk Si substrates. The process for experimentally determining the refractive index of planar PSi films is outlined in **Appendix A**.

As a demonstration, a SMC (**Figure 3.3a**) is etched with a current density profile consisting of three discrete segments of 20, 200, and 400 mA cm^{-2}, followed by a linear increase from 20 to 400 mA cm^{-2}. The resulting GRIN profile (**Figure 3.3b**) is visibly manifested by the color appearing from the thin-film interference within the SMC's n-type Si cap. As shown in this demonstration, one can leave a bulk Si core, further extending the accessible refractive index range and providing possibilities for exotic devices coupling GRINs with functional Si.

As is common for (100) mesoporous PSi, the pores align in domains with their long axis normal to the surface where they initiated, creating, for the SMC, four domains with aligned pores that converge at the center of the element (**Figure 3.4**). This has interesting optical implications, as PSi has been reported to possess a large positive birefringence ($n_e - n_o \approx 0.1 - 0.2$) with the optic axis defined by the pore orientation[28,29]. Henceforth, for simplicity, we assume a constant value of $n_e - n_o = 0.15$.

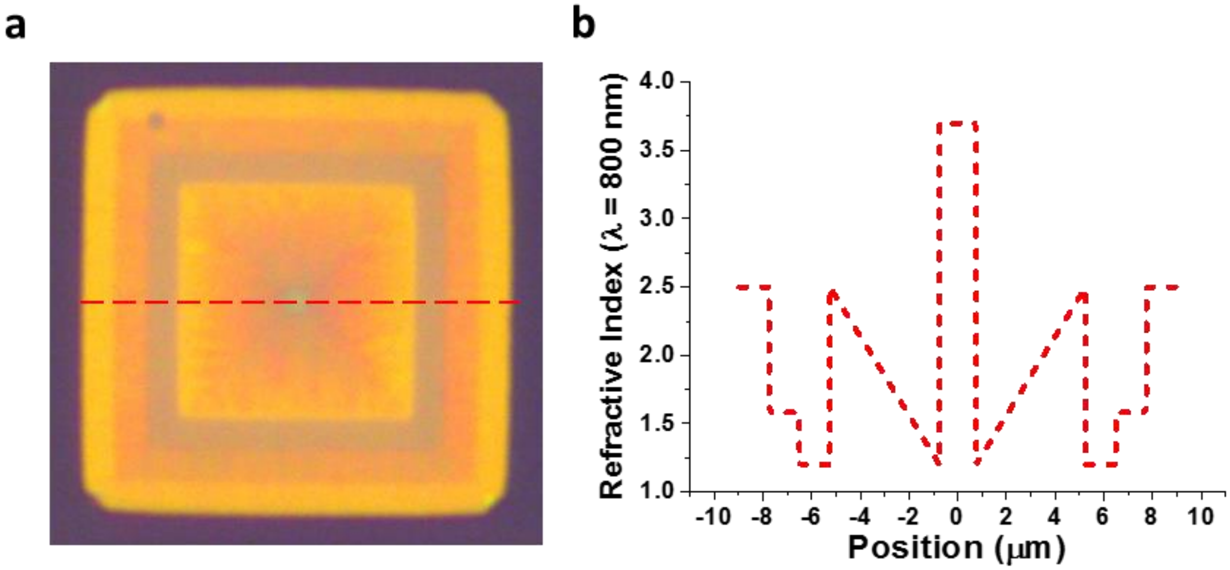

Figure 3.3. (a) Reflection-mode optical micrograph from the top of an ~18 μm PSi SMC with an arbitrary GRIN. The coloration is a result of thin-film interference effects within the n-type Si cap, which are modulated by the underlying GRIN of the PSi SMC. (b) The trace of the GRIN profile along the dashed red line in (a).

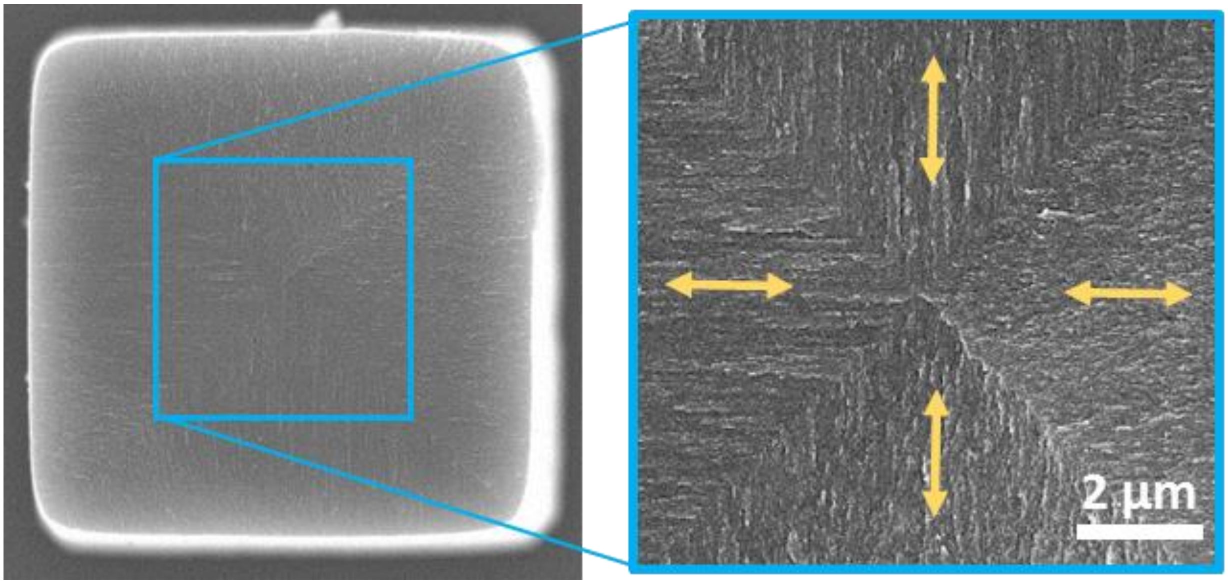

Figure 3.4. Low (left) and higher (right) magnification SEM image at the base of a fully-etched PSi SMC. The images display the convergence of four domains with defined pore orientation, represented by the yellow arrows at the right, which subsequently define the optic axis of each uniaxial birefringent domain.

3.3 Optical characterization

Optical characterization of the PSi SMCs is performed by mechanically removing them from the Si substrate and dispersing them on a glass substrate, where most elements end up lying flat on their side. The schematic shown in **Figure 3.5** summarizes the major parameters governing the optical response of the PSi SMCs. TM polarization will see the four domains as having the same refractive index, while TE polarization will interact with the ordinary refractive index (n_o) in the top and bottom domains and the (higher) extraordinary refractive index (n_e) in the left and right domains. Superimposed on any birefringence effects is the applied GRIN, represented here by a pair of general, truncated polynomials of order m that vary along the z-direction for the top and bottom domains and along the x-direction for the left and right domains.

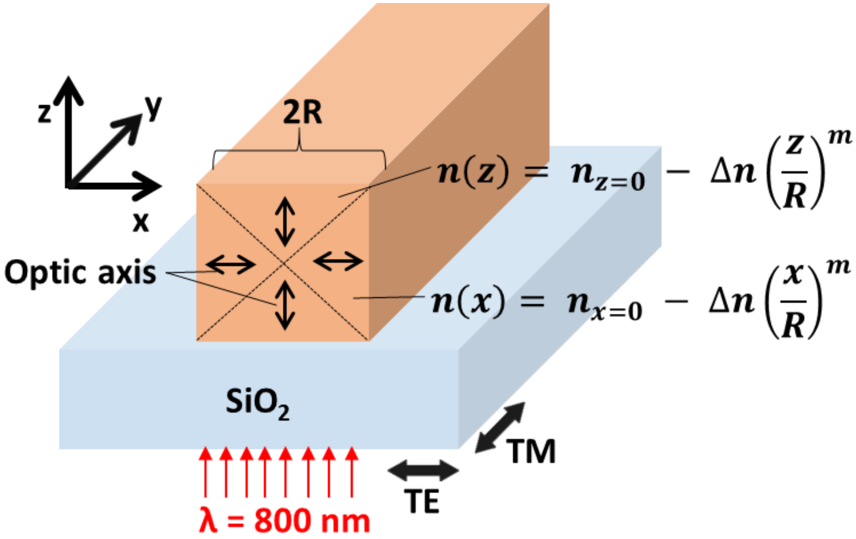

Figure 3.5. Schematic representing the major parameters under consideration when optically probing a side-lying PSi SMC on top of a transparent substrate.

As a simple predictor of birefringent and GRIN effects, one can look at the integrated optical thickness (OPT) (i.e., integrated along z-direction) across the x-direction of the sample as

$$OPT(x) = \int n(z)dz + n(x)dz \qquad \textbf{(3.1)}$$

Given the x-axis symmetry, we simply integrate over the refractive index profile in the first Cartesian quadrant (i.e., $x, z > 0$ with $x, z = 0$ at the center of the SMC) and multiply by 2

$$OPT(x) = 2\left[\int_x^R \left(n_{z=0} - \Delta n \left(\frac{z}{R}\right)^m\right) dz \; + \; \int_0^x \left(n_{x=0} - \Delta n \left(\frac{x}{R}\right)^m\right) dz\right] \qquad \textbf{(3.2)}$$

Performing this integration and substituting in the limits of integration gives

$$OPT(x) = 2\left[n_{z=0}R - \, n_{z=0}x - \frac{\Delta n}{R^m}\left(\frac{1}{m+1}\right) R^{m+1} + \frac{\Delta n}{R^m}\left(\frac{1}{m+1}\right) x^{m+1} + \, n_{x=0}x - \, n_{x=0}(0) - \frac{\Delta n}{R^m} x^m(x) + \frac{\Delta n}{R^m} x^m(0)\right] \qquad \textbf{(3.3)}$$

Finally, after grouping like-terms and simplifying, the generalized, integrated optical thickness is

$$OPT(x) = \frac{2\,\Delta n}{R^m}\left(\frac{1}{m+1} - 1\right)|x|^{m+1} + 2(n_{x=0} - n_{z=0})|x| + 2R\left(n_{z=0} - \frac{\Delta n}{m+1}\right) \qquad \textbf{(3.4)}$$

3.4 Basic birefringent response

For a purely birefringent structure ($\Delta n = 0$) the expression for OPT are

$$OPT_{TM}(x) = \; 2R(n_o) \qquad \textbf{(3.5)}$$

$$OPT_{TE}(x) = \; 2(n_e - n_o)|x| + 2R(n_o) \qquad \textbf{(3.6)}$$

with $x = 0$ defined to be at the center of the SMC. As expected, the TM OPT is uniform across the structure given the homogeneous refractive index (**Figure 3.6a**), indicating that TM light should pass through unperturbed. The TE response is more complicated in that the positive birefringence and internal structure (i.e., the convergent trajectory of the pores in the four domains) couple such that the OPT increases linearly towards the edge of the SMC (**Figure 3.6b**), suggesting that TE light will be diverged by its interaction with the birefringent SMC. Simulations performed with COMSOL Multiphysics® Modeling Software (**Figure 3.6c, d**), optical measurements at 800 nm (**Figure 3.6e, f**), and OPT-based predictions all strongly agree for both the TM and TE cases. The agreement between simulation and experiment even includes the observed small amount of

TM beam convergence, attributed to diffraction at the edge of the SMC. Interestingly, these simple structures exhibit functionality comparable to that of dielectric metasurfaces for pixel-integrated polarization splitters[30]. We suggest that birefringent shape-defined PSi structures offer a powerful option for realizing such elements without the need for processes like electron-beam lithography.

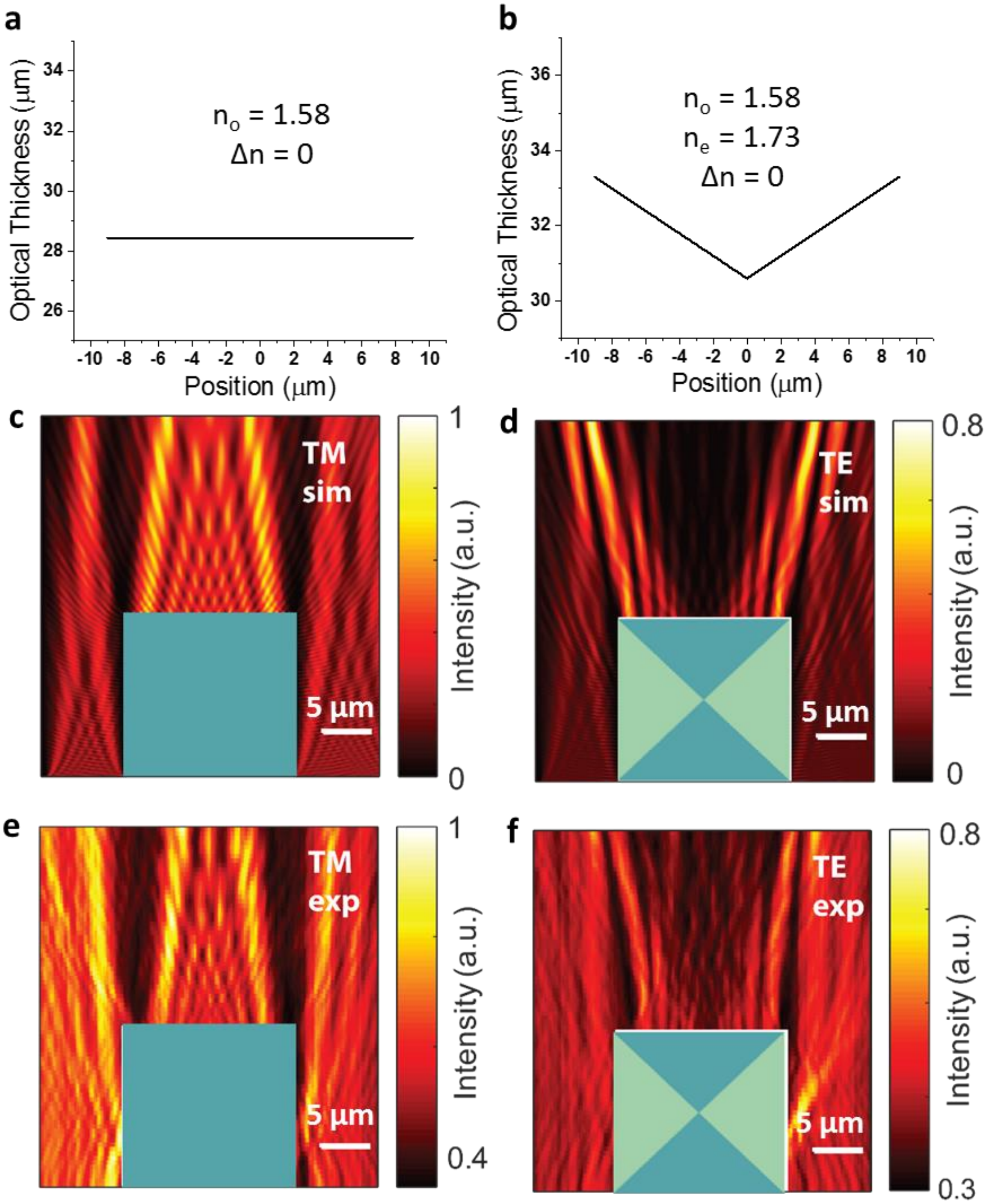

Figure 3.6. (a) Integrated OPT for TM polarization interacting with a homogeneously etched PSi SMC, which is optically flat. (b) Integrated OPT for TE polarization interacting with a

Figure 3.6 (cont.) homogeneously etched PSi SMC, which exhibits a linear OPT profile expected to diverge light. (c) Simulated intensity distribution for TM polarization interacting with a homogeneously etched PSi SMC confirming that light passes through largely unperturbed, with the exception of a small amount of beam convergence attributed to diffraction effects at the edges of the PSi SMC. (d) Simulated intensity distribution for TE polarization interacting with a homogeneously etched PSi SMC confirming that light should diverge as a result of the birefringence and internal structure. (e, f) Experimental intensity distributions for TM and TE polarizations, respectively, that are in strong agreement with simulations. (c) and (d) are normalized to the maximum intensity observed in simulation, while (e) and (f) are normalized to the maximum intensity observed in experiment.

3.5 Birefringence plus linear gradient refractive index

While the birefringence of PSi SMCs results in interesting properties, our primary interest is to exploit PSi's refractive index modulation capabilities. Here, we show that a linear GRIN (i.e., m = 1) generates a parabolic OPT capable of polarization-selective light focusing. Inserting m = 1 into **Equation (3.4)** yields

$$OPT_{TM}(x) = \frac{-\Delta n}{R}|x|^2 + 2R\left(n_{o,z=0} - \frac{\Delta n}{2}\right) \tag{3.7}$$

$$OPT_{TE}(x) = \frac{-\Delta n}{R}|x|^2 + 2\left(n_{e,x=0} - n_{o,z=0}\right)|x| + 2R\left(n_{o,z=0} - \frac{\Delta n}{2}\right) \tag{3.8}$$

which are plotted in **Figure 3.7a** and **Figure 3.7b**, respectively. TM light focusing by the linear GRIN PSi SMC is readily observed in simulation (**Figure 3.7c**), while the TE case is more complex, with an OPT profile consisting of adjacent parabolas (**Figure 3.7b**) that are functionally equivalent to two side-by-side lenses. The simulation of the structure's TE behavior (**Figure 3.7d**) is characterized by two high-intensity focal regions laterally displaced to either side of the single TM focus. To fabricate this linear GRIN element, we etch a SMC with a current density graded from ~300 to ~150 mA cm^{-2} such that the (ordinary) refractive index increases linearly from ~1.4 to ~1.7 (edge to center). The experimentally measured TM and TE intensity distributions (**Figure 3.7e, f**) strongly agree with simulations.

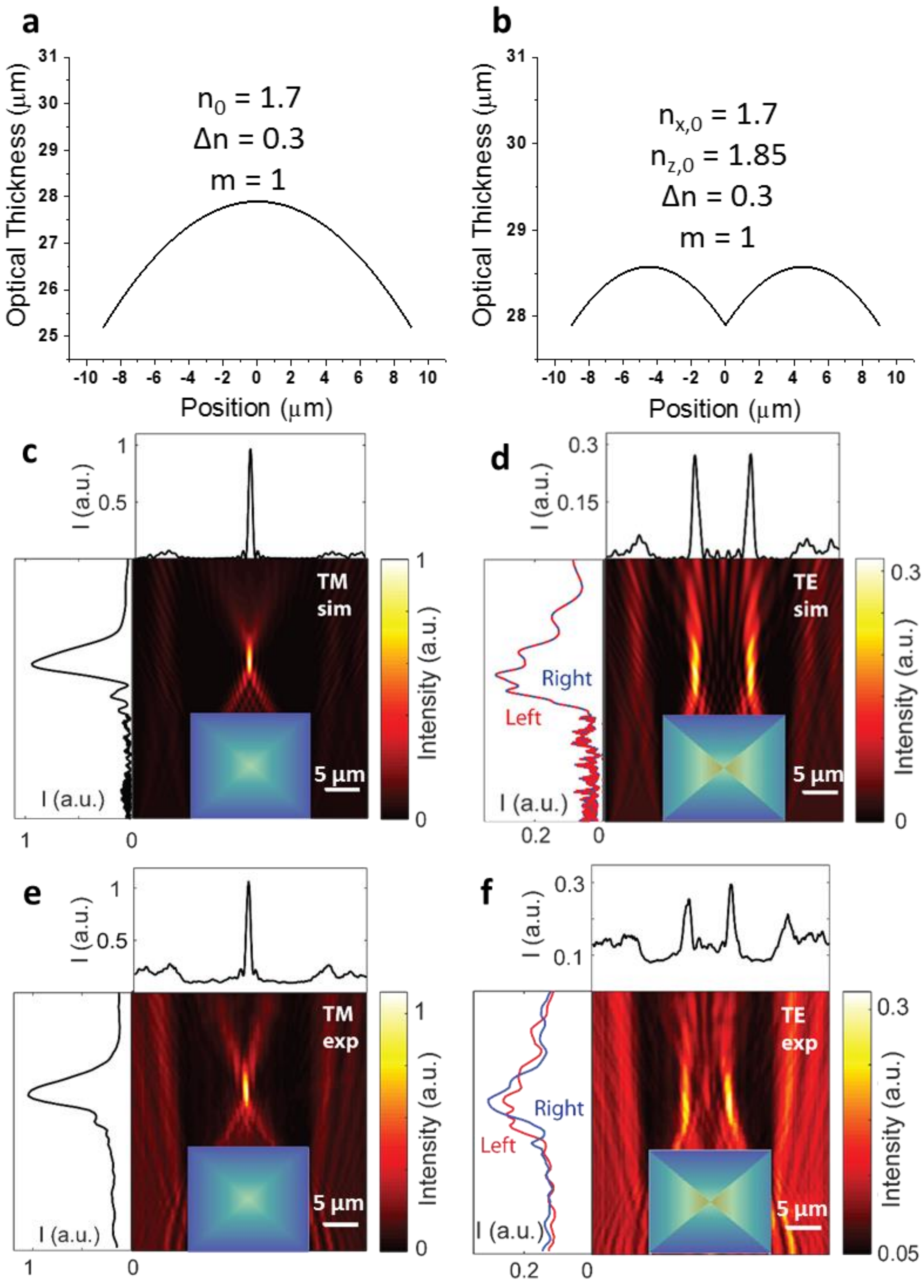

Figure 3.7. (a) Integrated OPT for TM polarization interacting with a linear GRIN PSi SMC that possesses a lens-like radius of curvature. (b) Integrated OPT for TE polarization interacting with a linear GRIN PSi SMC that exhibits two adjacent regions possessing a radius of curvature, which is functionally equivalent to two side-by-side lenses. (c) Simulated intensity distribution for TM

Figure 3.7 (cont.) polarization interacting with a linear GRIN PSi SMC, as expected, focusing is observed. (d) Simulated intensity distribution for TE polarization interacting with a linear GRIN PSi SMC that exhibits two high-intensity regions laterally displaced from the simulated TM focus. (e, f) Experimental intensity distributions for TM and TE polarizations, respectively, that are in strong agreement with simulations. (c) and (d) are normalized to the maximum intensity observed in simulation, while (e) and (f) are normalized to the maximum intensity observed in experiment. In (c)-(f) the top and side panels represent traces that are transverse to and along the propagation direction, respectively, and run through the region(s) of maximum intensity.

Under TM illumination, the measured back focal length is ~10 µm, which can be modulated by changing the magnitude of the GRIN variation (**Figure 3.8**), while the convergence (half) angle from the back surface is ~30^0, suggesting a numerical aperture of ~0.5. As such, a diffraction-limited focal spot is ~λ (800 nm in this case), similar to the full-width half-maximum of the intensity trace along the focal plane in **Figure 3.7e**. For TE illumination, there is a slight deviation from the simulation results, which may be a result of the assumed value and spatial invariance of birefringence. Still, our simple assumptions reasonably capture the coupled birefringent/GRIN response for a linear GRIN PSi SMC.

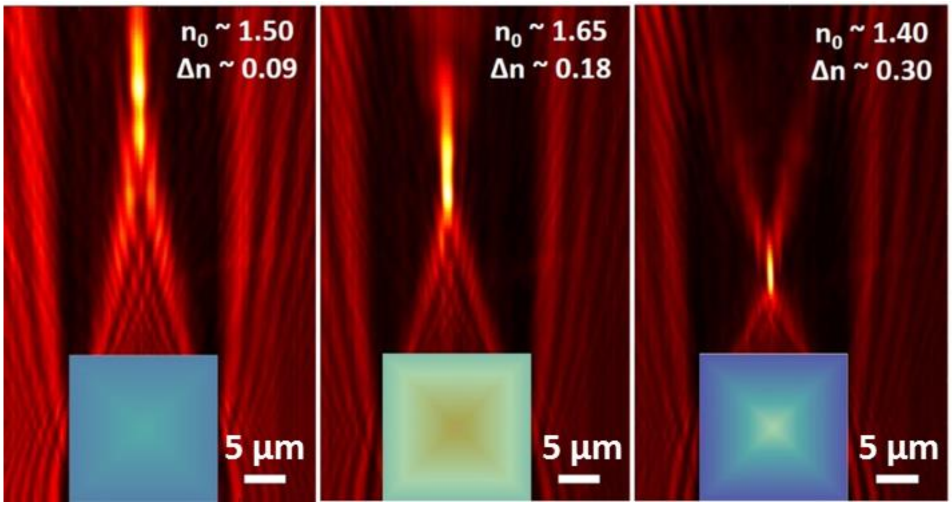

Figure 3.8. Collection of experimentally collected TM intensity profiles for three separate PSi linear GRIN SMCs etched such that the magnitude of the linear GRIN is varied. As can be seen, increasing the magnitude of the linear GRIN change reduces the TM focal length of the SMC.

3.6 Conclusions

In summary, we have presented a new technique for fabricating birefringent GRIN micro-optics based on the shape-defined formation of PSi. Using a SMC geometry, we showed that the birefringence of a homogeneous PSi structure offers opportunities beyond dielectric metasurfaces for easily fabricated polarization splitters. Additionally, we demonstrated that a PSi SMC possessing a linear GRIN is capable of focusing TM light to a diffraction-limited line, while TE light is directed to two high-intensity regions in roughly the same plane as, but laterally displaced to either side of, the TM focus. In light of these results, we envision possibilities beyond polarization-selective pixels, such as tailoring geometries and GRIN profiles for on-chip optical "Janus" devices[31] capable of performing modal operations like conversion or splitting as part of photonic integrated circuits.

3.7 Experimental Methods

3.7.1 Silicon micro-column fabrication

Fabrication was performed on 4" diameter, highly doped (ρ ~ 0.001 – 0.005 Ω cm) p-type (100) Si wafers (Topsil). Wafers were cleaned with Nanostrip for 10 min at 70 ^{0}C, followed by deposition of ~ 1.5 µm of SiO_2 by plasma-enhanced chemical vapor deposition (Trion Minilock-Orion PECVD, located in the Micro and Nanotechnology (MNTL) cleanroom) on the backside to serve as a diffusion barrier. Dr. Seung-Kyun Kang, a post-doctoral researcher in the group of Prof. John Rogers, performed n-type doping for ~ 10 min at 1000 ^{0}C in a furnace containing a solid-state Phosphorous source. After doping, the wafer was cleaned again with Nanostrip, followed by removal of all SiO_2 by immersing in 48% hydrofluoric acid (aq) for 2 min at room temperature. Photolithography was performed by processing SPR220-4.5 (Shipley) positive photoresist under manufacturer recommended conditions and exposing with an EVG620 mask aligner (EV Group).

Development with AZ MIF 917 (AZ Electronic Materials) reveals arrays of photoresist squares with their sides oriented such that the resulting Si square micro-column sidewalls will align with (100) degenerate crystal planes (which allows PSi etching calibration to be performed with flat pieces of (100) Si). Si etching was performed with a Pegasus ICP-DRIE (SPTS Technologies) running a Bosch process. Photolithography and DRIE were both carried out in the Micro-Nano-Mechanical Systems (MNMS) cleanroom in the Mechanical Engineering Building (MEB). After a final cleaning with Nanostrip, the Si wafer is cleaved into ~ 15 mm x 15 mm square chips containing a ~ 3 mm x 3 mm array of square micro-columns and placed in an electrochemical cell for PSi etching.

3.7.2 Porous silicon etching

Etching was carried out in a polypropylene cell with an exposed etch area of ∼1.20 cm^2. The electrolyte comprised a 1:1 volume ratio of 48% hydrofluoric acid (aq) and 100% ethanol. A 5 mm diameter Pt–Ir inoculating loop (Thomas Scientific) served as the counter electrode. Contact to the back of the SMC-containing Si chip was established with a stainless steel electrode. Current was delivered to the cell by an SP-200 research grade potentiostat/galvanostat (Bio-Logic Science Instruments). The current waveforms for generating GRIN samples were constructed via BenchLink Waveform Builder Pro software (Keysight Technologies, Inc.) and sent to the SP-200 through a 33220A Function/Arbitrary Waveform Generator (Keysight Technologies, Inc.). After etching, all samples were thoroughly rinsed with ethanol and dried under a gentle stream of nitrogen.

3.7.3 Optical characterization

PSi refractive index versus wavelength information at specific fabrication current densities was extracted from the reflectance spectrum of planar thin films (see **Appendix A**). Reflectance spectra were collected using a Si PDA spectrometer (Control Development, Inc.) hooked up to an Axio Observer D1 inverted microscope (Carl Zeiss, Inc.) with a white-light halogen lamp serving as the source. The setup is located in the Microscopy Suite of the Beckman Institute for Advanced Science and Technology.

The intensity distribution of the light transmitted through the a PSi SMC was measured at Stanford University by graduate student Aaron Holsteen using a confocal microscope (Nikon Eclipse, C1) in the lab of Prof. Mark Brongersma. The setup, shown in **Figure 3.9**, uses a white light supercontinuum illumination source that is wavelength-tunable from 400 to 2200 nm (NKT, SuperK Extreme). A linear polarizer and a half waveplate are utilized to generate a linearly polarized illumination beam. A substrate with PSi SMCs is mounted on a XYZ scan stage, such that SMC-containing side faces upwards towards the microscope objective, and is illuminated from below with the laser beam set to 800 nm. The light intensity in the x-y plane above the GRIN element is gathered using a 100X objective with a numerical aperture of 0.9 and captured by a high-resolution CCD camera (Princeton Instruments, PIXIS 1024B). By stepping the stage in 500 nm increments, images in the x-y plane can be stacked in the z dimension to construct the light intensity volume above the PSi SMC.

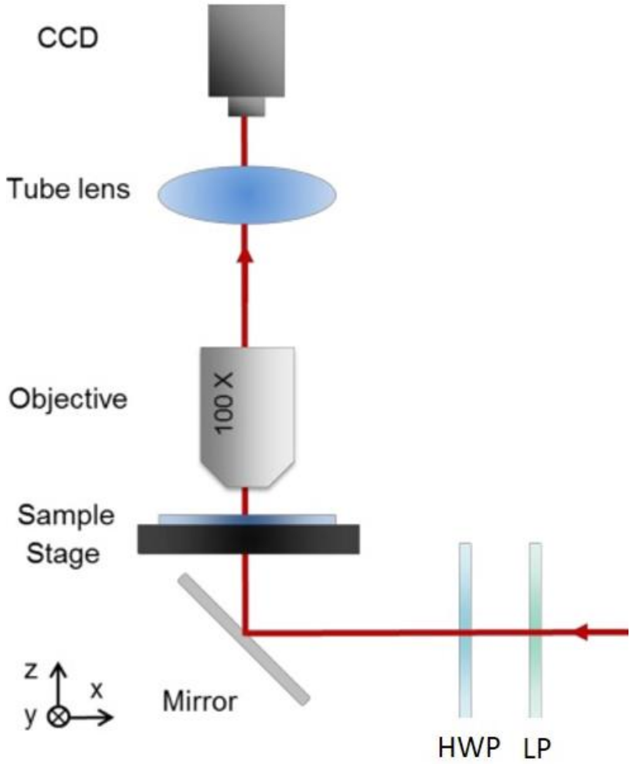

Figure 3.9. A schematic for the optical setup used by graduate student Aaron Holsteen to characterize side-lying PSi SMCs. A polarized and collimated laser beam with wavelength 800 nm is sent into a confocal microscope and propagates upward through the bottom of the sample stage, interrogating the sample. The sample stage is translated in the z-direction in discrete, 500 nm steps in order to collect various x-y plane intensity distributions, which are later stacked to recreate the intensity profile transmitted by the PSi SMC. The optical setup is located in the lab of Prof. Mark Brongersma at Stanford University.

3.8 References

1. Leonhardt, U. & Philbin, T. G. in *Progress in Optics* (ed. Wolf, E.) **53,** 69–152 (Elsevier, 2009).
2. Di Falco, A., Kehr, S. C. & Leonhardt, U. Luneburg lens in silicon photonics. *Opt. Express* **19,** 5156–5162 (2011).
3. Gabrielli, L. H. & Lipson, M. Integrated Luneburg lens via ultra-strong index gradient on silicon. *Opt. Express* **19,** 20122–20127 (2011).
4. Hunt, J. *et al.* Planar, flattened Luneburg lens at infrared wavelengths. *Opt. Express* **20,** 1706 (2012).

5. Valentine, J., Li, J., Zentgraf, T., Bartal, G. & Zhang, X. An optical cloak made of dielectrics. *Nat. Mater.* **8,** 568–571 (2009).

6. Gabrielli, L. H., Cardenas, J., Poitras, C. B. & Lipson, M. Silicon nanostructure cloak operating at optical frequencies. *Nat. Photonics* **3,** 461–463 (2009).

7. Spadoti, D. H., Gabrielli, L. H., Poitras, C. B. & Lipson, M. Focusing light in a curved-space. *Opt. Express* **18,** 3181–3186 (2010).

8. Danner, A. J., Tyc, T. & Leonhardt, U. Controlling birefringence in dielectrics. *Nat. Photonics* **5,** 357–359 (2011).

9. Canham, L. T. Silicon quantum wire array fabrication by electrochemical and chemical dissolution of wafers. *Appl. Phys. Lett.* **57,** 1046–1048 (1990).

10. Lehmann, V. & Gösele, U. Porous silicon formation: A quantum wire effect. *Appl. Phys. Lett.* **58,** 856–858 (1991).

11. Gal, M., Reece, P. J., Zheng, W. & Lerondel, G. Porous silicon: a versatile optical material. in *Proc. SPIE* **5277,** 9–16 (2004).

12. Smith, R. L. & Collins, S. D. Porous silicon formation mechanisms. *J. Appl. Phys.* **71,** R1–R22 (1992).

13. Zhang, X. G. Morphology and Formation Mechanisms of Porous Silicon. *J. Electrochem. Soc.* **151,** C69–C80 (2004).

14. Frohnhoff, S. & Berger, M. G. Porous silicon superlattices. *Adv. Mater.* **6,** 963–965 (1994).

15. Vincent, G. Optical properties of porous silicon superlattices. *Appl. Phys. Lett.* **64,** 2367–2369 (1994).

16. Lin, V. S.-Y., Motesharei, K., Dancil, K.-P. S., Sailor, M. J. & Ghadiri, M. R. A Porous Silicon-Based Optical Interferometric Biosensor. *Science* **278,** 840–843 (1997).

17. Mulloni, V. & Pavesi, L. Porous silicon microcavities as optical chemical sensors. *Appl. Phys. Lett.* **76,** 2523–2525 (2000).

18. Rong, G., Najmaie, A., Sipe, J. E. & Weiss, S. M. Nanoscale porous silicon waveguide for label-free DNA sensing. *Biosens. Bioelectron.* **23,** 1572–1576 (2008).

19. Link, J. R. & Sailor, M. J. Smart dust: Self-assembling, self-orienting photonic crystals of porous Si. *Proc. Natl. Acad. Sci.* **100,** 10607–10610 (2003).

20. Ilyas, S. & Gal, M. Gradient refractive index planar microlens in Si using porous silicon. *Appl. Phys. Lett.* **89,** 211123–211123–3 (2006).

21. Collins, B. E., Dancil, K.-P. S., Abbi, G. & Sailor, M. J. Determining Protein Size Using an Electrochemically Machined Pore Gradient in Silicon. *Adv. Funct. Mater.* **12,** 187–191 (2002).

22. Li, Y. Y., Kim, P. & Sailor, M. J. Painting a rainbow on silicon – a simple method to generate a porous silicon band filter gradient. *Phys. Status Solidi A* **202,** 1616–1618 (2005).

23. Barth, D. S. *et al.* Macroscale Transformation Optics Enabled by Photoelectrochemical Etching. *Adv. Mater.* **27,** 6131–6136 (2015).

24. Ruminski, A. M. *et al.* Topological Control of Porous Silicon Photonic Crystals by Microcontact Printing. *Adv. Opt. Mater.* **1,** 510–516 (2013).

25. Mangaiyarkarasi, D., Breese, M. B. H. & Ow, Y. S. Fabrication of three dimensional porous silicon distributed Bragg reflectors. *Appl. Phys. Lett.* **93,** 221905 (2008).

26. Kempa, T. J., Bediako, D. K., Kim, S.-K., Park, H.-G. & Nocera, D. G. High-throughput patterning of photonic structures with tunable periodicity. *Proc. Natl. Acad. Sci.* **112,** 5309–5313 (2015).

27. Imai, K. A new dielectric isolation method using porous silicon. *Solid-State Electron.* **24,** 159–164 (1981).

28. Kashkarov, P. K. *et al.* Photonic bandgap materials and birefringent layers based on anisotropically nanostructured silicon. *J. Opt. Soc. Am. B* **19,** 2273 (2002).

29. Ishikura, N., Fujii, M., Nishida, K., Hayashi, S. & Diener, J. Dichroic rugate filters based on birefringent porous silicon. *Opt. Express* **16,** 15531 (2008).

30. Khorasaninejad, M., Zhu, W. & Crozier, K. B. Efficient polarization beam splitter pixels based on a dielectric metasurface. *Optica* **2,** 376 (2015).

31. Zentgraf, T., Valentine, J., Tapia, N., Li, J. & Zhang, X. An Optical ‘Janus’ Device for Integrated Photonics. *Adv. Mater.* **22,** 2561–2564 (2010).

CHAPTER 4

FLAT CYLINDRICAL GRADIENT REFRACTIVE INDEX MICROLENS ARRAYS FROM SHAPE-DEFINED POROUS SILICON FORMATION

4.1 Introduction

A gradient refractive index (GRIN) material, so-named for its spatially-graded refractive index, causes light to travel a curved path[1,2]. Maxwell[3] and Luneburg[4] were among the first to consider the implications of optical elements with GRIN media, designing spherically-symmetric GRIN lenses capable of the aberration-free imaging of light from any direction[5]. Flat GRIN lenses, reportedly first proposed by Wood[6], similarly exploit the curvilinear trajectory of light through optically inhomogeneous media[7], imparting an otherwise optically uninteresting geometry with the refractive power of a lens. These flat GRIN lenses can exhibit improved performance through reduced aberrations[8,9] and offer advantageous form factors for integration within optical systems[9,10]. Flat lenses with 2D GRIN profiles that focus light to a spot tend to be more prevalent, but there are applications for 1D GRIN profiles that generate a focal line (i.e., cylindrical lenses), both at the macro- and microscale, such as shaping an astigmatic laser diode beam[11]. Although mature and commercially available, GRIN technology continues to seeks improvements in the magnitude, sharpness, and precision of manufactured GRIN profiles[8,9].

Porous silicon (PSi) is an interesting material to consider for GRIN elements[12,13]. Formed by electrochemically etching Si, the material's porosity and, consequently, effective refractive index, is defined by the applied etching current density[14,15]. As a result, a GRIN profile is defined with a temporally-modulated current density, which has yielded 1D GRIN optical superlattices[16,17] that can function as chemical sensors[18–20] given the sensitivity of PSi to foreign media penetrating its microstructure[21–23]. These elements are able to feature very large GRINs (dn ~ 1.0) over very short spatial dimensions (~ 1 µm) with the GRIN profile controlled by the input electrochemical current density waveform. This is in contrast to existing GRIN technology that can only change the refractive index by ~ 0.2 over millimeter length scales[8,24].

Here, we demonstrate that shape-defined PSi formation offers a viable new option towards planar, 1D GRIN microlens arrays (MLAs). We first introduce the process for manufacturing a PSi GRIN MLA, utilizing the optical properties and etching characteristics of PSi to construct the current density waveform that generates the desired spatial GRIN profile along the shape-defined etch pathway. The PSi GRIN MLA is isolated for optical characterization by embedding in a slab of transparent optical polymer, mechanically detaching the slab with the embedded GRIN MLA, and planarizing via basic mechanical polishing. Applying this design methodology and planarization technique, flat elements in the form of GRIN MLAs exhibiting line focusing and GRIN axicons generating Bessel sheet beams are achieved.

4.2 Shape-Defined Porous Silicon Microlens Arrays

Shape-defined formation of PSi GRIN MLAs begins with a crystalline, p-type Si wafer that features a thin (~ 100 nm) n-type region at its surface. Standard photolithography and deep reactive ion etching microfabrication techniques pattern the wafer with a 2D array of rectangular Si blocks (L ~ 150 µm, W ~ 18 µm, and H ~ 30 µm) (**Figure 4.1a**). While one could ideally utilize a circular geometry, the dependence of PSi formation on the crystallographic orientation of Si prevents an isotropic radial etch[25]. The n-type surface region from the starting wafer leaves the rectangular Si blocks with an n-type surface cap that inhibits PSi formation during electrochemical etching (**Figure 4.1b**), restricting the PSi GRIN profile to the x-direction within the rectangular Si feature (**Figure 4.1c**).

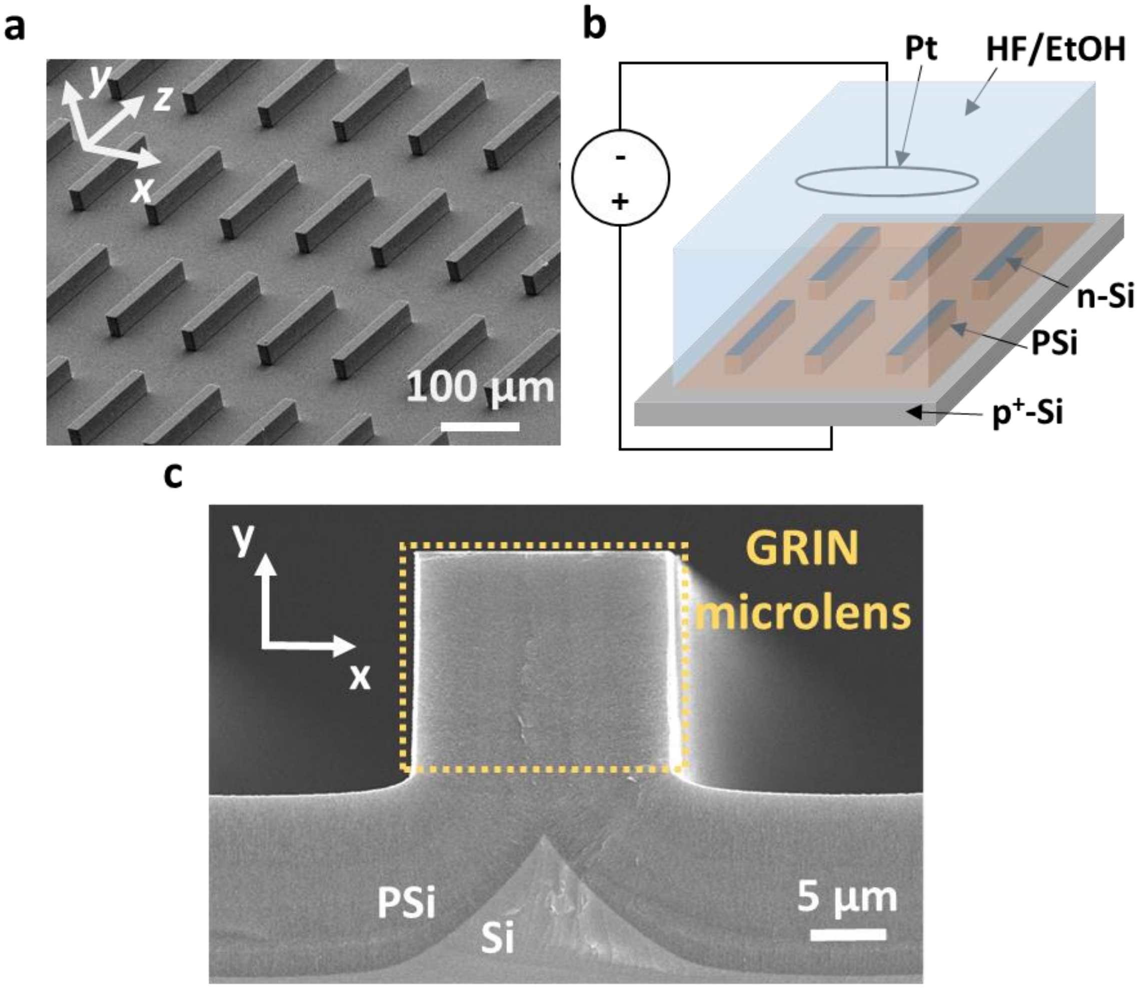

Figure 4.1. Shape-defined PSi formation for cylindrical GRIN MLAs. (a) Oblique incidence SEM image of an array of Si rectangular blocks generated by standard photolithography and deep reactive ion etching. (b) Schematic representing the electrochemical process that transforms the microfabricated Si rectangular block array into a PSi GRIN MLA. (c) Cross-section SEM image of a single lens within the PSi GRIN MLA.

In order for the initially bulk Si block to be transformed into a PSi GRIN lens, the current density dependence of PSi's refractive index and etch rate is used to construct the temporal current density waveform that generates the desired GRIN profile during electrochemical etching. We define the (ordinary) refractive index (λ = 800 nm) to be 1.60 at the center of the lens, decreasing to 1.40 at the edge along a parabolic trajectory. This GRIN profile, given by

$$n_o(x) = 1.60\,(1 - 0.5\alpha^2 x^2) \tag{4.1}$$

is plotted in **Figure 4.2a**, with a GRIN constant α = 0.0568 μm^{-1}. The dependence of PSi's (ordinary) refractive index on etching current density (**Figure 4.2b**) maps this spatial GRIN profile to a spatial current density profile (**Figure 4.2c**).

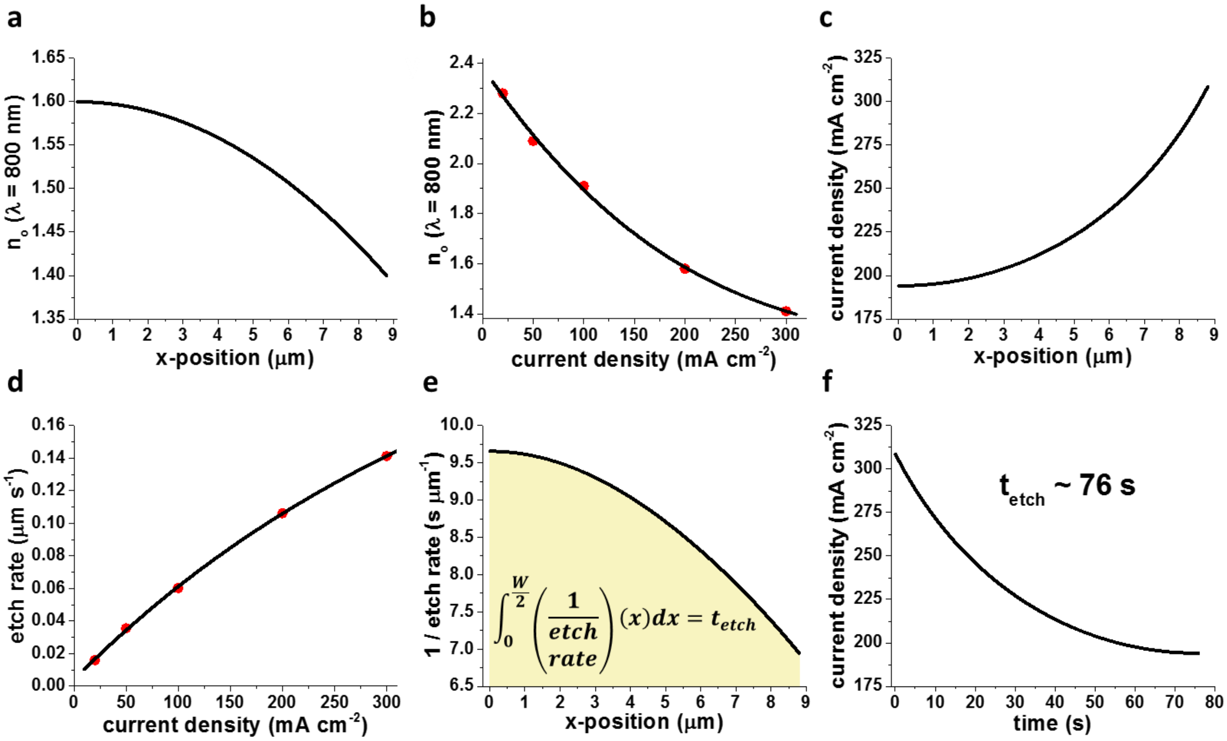

Figure 4.2. Converting a spatial GRIN profile into a temporal current density waveform. (a) The desired spatial GRIN profile to be etched into the lenses within the PSi GRIN MLA. (b) Refractive index versus etching current density relationship for PSi. (c) The spatial current density profile required to generate the spatial GRIN profile in (a), determined by using the refractive index versus current density in (b) to map refractive index to current density. (d) Empirically-measured etch rate versus etching current density relationship for PSi. (e) Using the etch rate information in (d), the spatial current density profile in (c) is mapped to a 1/etch rate versus position curve. The area under the 1/etch versus position curve represents the total required etching time. (f) With the required etching time calculated, the current density versus time waveform can finally be constructed. Given that the starting point of etching is $x = \frac{W}{2}$ at $t = 0$ and converges to $x = 0$ at $t = t_{etch}$, there is a one-to-one space-to-time mapping that transforms the spatial current density profile in (c) into a temporal current density waveform.

Next, the known etch rate information (**Figure 4.2d**) is used to map the current density profile to a spatial map of 1 / etch rate. The reason for utilizing the inverse etch rate is that the area under the curve (**Figure 4.2e**), expressed as the integral from the center ($x = 0$) to the edge ($x = \frac{W}{2}$) of the GRIN lens

$$\int_0^{\frac{W}{2}} \left(\frac{1}{\substack{etch \\ rate}}\right)(x)dx = t_{etch} \qquad \textbf{(4.2)}$$

gives the total required etch time (t_{etch}). This allows the current density profile to be mapped from the spatial to the temporal domain using the fact that starting point of etching is $x = \frac{W}{2}$ at $t = 0$ and converges to $x = 0$ at $t = t_{etch}$. As such, the spatial current density profile is transformed into a time-varying waveform (**Figure 4.2f**), fit to a third-order polynomial of the form

$$J(t) \cong 308 - 3.90\,t + (4.65 \times 10^{-2})\,t^2 - (1.98\,\times 10^{-4})\,t^3 \quad [mA\;cm^{-2}] \qquad \textbf{(4.3)}$$

4.3 Isolating and planarizing microlens arrays

With the ease of current density modulation, the waveform of **Equation (4.3)** is readily applied to electrochemically etch an array of Si rectangular blocks into a PSi GRIN MLA with the GRIN profile of **Equation (4.1)**. However, the MLA needs to be displaced from the Si fabrication substrate in order to be characterized, as the sub-surface formation of PSi generates a sharp scattering feature (**Figure 4.1c**) under each individual lens that would scatter light even if the MLA could be characterized on-wafer. To accomplish this, we center the PSi GRIN MLA within a ~ 10 mm diameter well made from a slab of cured polydimethylsiloxane (PDMS) that is ~ 2-3 mm thick. The PDMS well is filled with Norland Optical Adhesive (NOA), covered with a flat piece of cured PDMS to limit meniscus formation in the NOA layer, and then cured with ultraviolet light. The cured NOA and embedded MLA are separated from the Si wafer (**Figure 4.3a**) with a razor blade applying force along the x-direction (i.e., along the width of the PSi GRIN lens).

This mechanical detachment technique is fast and convenient, but not without issues. The PSi GRIN MLA fracture surface is not flat (**Figure 4.3b**) and each element in the MLA tends to sit ~ 3 - 4 µm below the NOA surface at the lowest point (**Figure 4.3c**), leaving the resulting lenses ~ 26 µm thick. To planarize the PSi GRIN MLA, an O_2 reactive ion etch selectively etches back the surrounding NOA medium and is followed by mechanical polishing. The planarized PSi GRIN MLA embedded in NOA (**Figure 4.3d**) exhibits improved surface quality when inspected with optical (**Figure 4.3e**) and atomic force microscopy (**Figure 4.3f**).

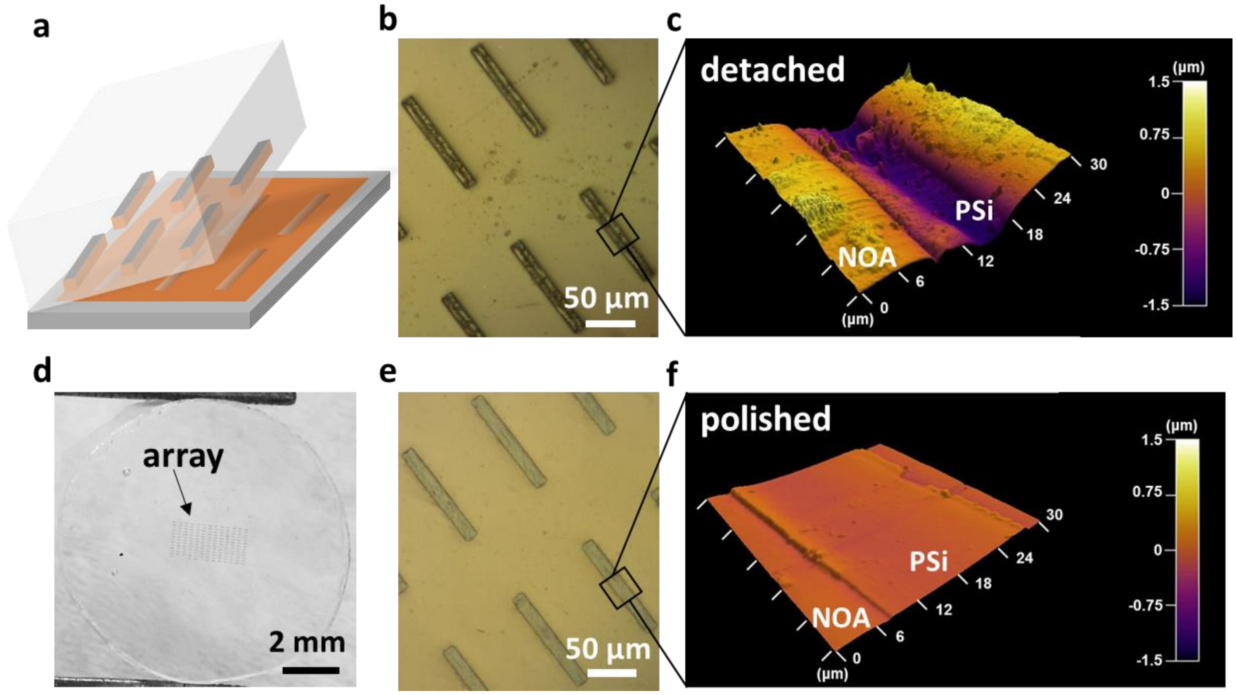

Figure 4.3. Embedding, detaching, and planarizing a PSi GRIN MLA. (a) Schematic representing a PSi GRIN MLA being embedded in NOA optical polymer that is cured and then mechanically detached, isolating the embedded PSi GRIN MLA from its Si fabrication substrate. (b) Top view optical micrograph of a section of the PSi GRIN MLA after detachment. (c) Atomic force microscopy-generated surface topography of a section of a single lens (and surrounding NOA) within the PSi GRIN MLA after the detachment process. (d) Top view optical image of a processed PSi GRIN MLA and the surrounding NOA optical polymer in which it is embedded. (e) Top view optical micrograph of a section of the PSi GRIN MLA after planarization. (f) Atomic force microscopy-generated surface topography of a section of a single lens (and surrounding NOA) within the PSi GRIN MLA after the planarization process.

While improved, the surface finish is not optically perfect. But, this could be improved by alternative, established techniques, such as backside planarization through the Si wafer or perhaps even diamond turning of the PSi GRIN MLA embedded in optical polymer. Additionally, elongated geometries (e.g., lenticular lenses) figure to be incompatible with our mechanical detachment process and are likely to require processing through the backside of the Si fabrication wafer. Still, our simple planarization methodology has afforded sufficient surface quality to optically probe the PSi GRIN MLA and provide strong proof of concept.

4.4 Optical characterization

The planarized PSi GRIN MLA can be optically interrogated with confocal microscopy. PSi possesses a positive, uniaxial birefringence with the optic axis defined by the pore direction[26,27], so both the TM polarization (along the z-direction/length of lens), which encounters the ordinary refractive index ($n_o(x)$), and TE polarization (along the x-direction/width of lens), which encounters the extraordinary refractive index ($n_e(x)$), are investigated. For simplicity, the birefringence is assumed constant with $n_e(x) - n_o(x)$ = 0.15. Therefore,

$$n_e(x) = 1.75\,(1 - 0.5\alpha^2 x^2) \tag{4.4}$$

where again the GRIN constant α = 0.0568 µm^{-1}. Focal lines are observed from the MLA for both TM (**Figure 4.4a**) and TE (**Figure 4.4b**) polarization, confirming operation of the MLA. Looking at the cross-sectional view of the transmitted intensity distribution above a single element, the focal length for the TM and TE polarization is found to be ~ 2 µm (**Figure 4.4c, trace in left panel**) and ~ 1 µm (**Figure 4.4d, trace in left panel**), respectively. These focal lengths agree well with COMSOL Multiphysics® Modeling Software simulations (**Figure 4.4e, f**), but the beam width in the focal plane (**Figure 4.4c-f, trace in top panel**) is noticeably broader in experiment. This may be from a small GRIN profile aberration or scattering from surface roughness. Even so, this demonstrates the opportunity that shape-defined PSi formation provides for cylindrical GRIN MLAs, which are useful as collection optics for detectors[28] operating at NIR and IR wavelengths.

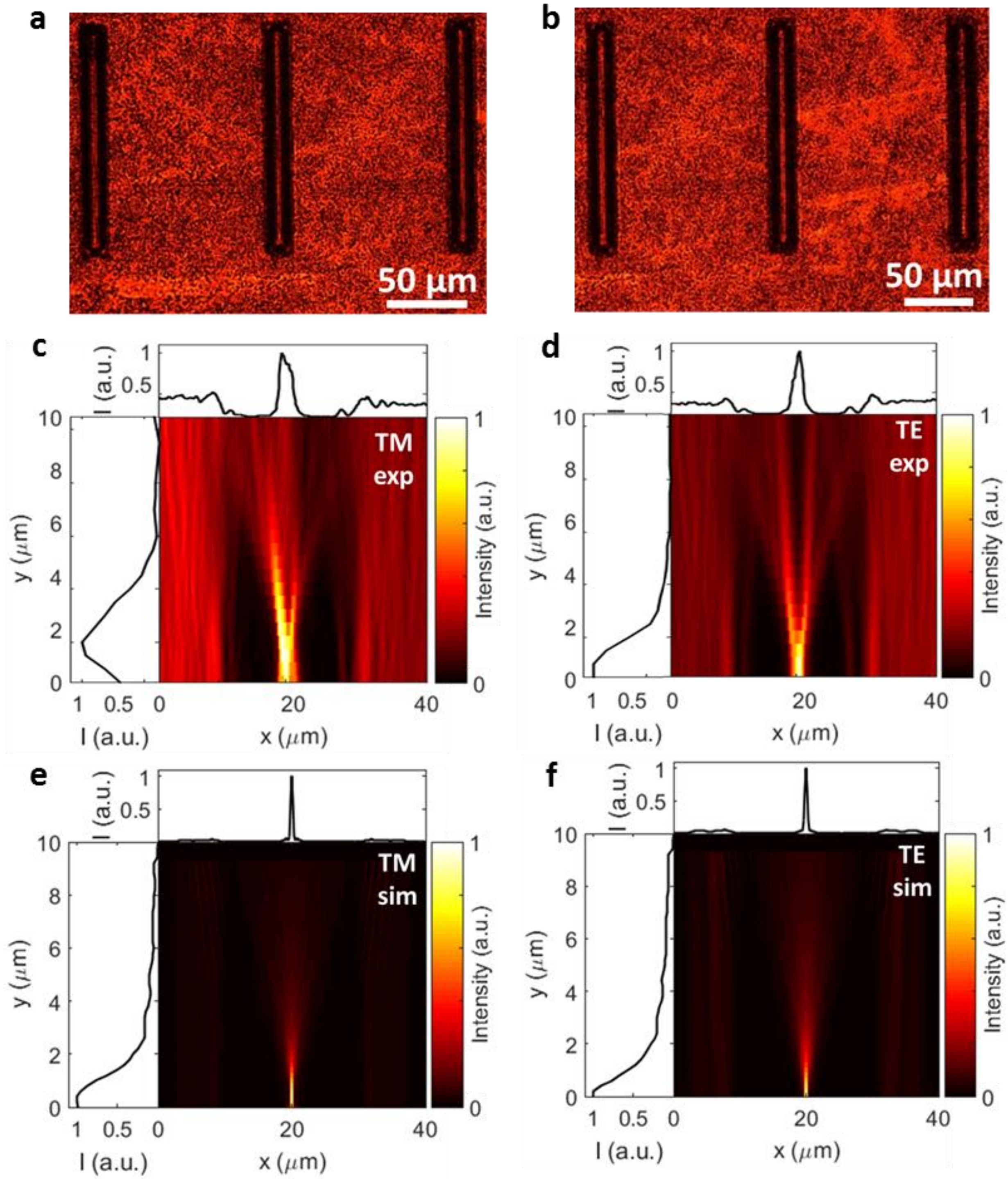

Figure 4.4. Optical characterization of PSi GRIN MLA with parabolic GRIN profile. (a), (b) Top view image in focal plane of PSi GRIN MLA under illumination with TM and TE polarization, respectively. (c), (d) Cross-sectional view of experimentally collected intensity distribution above a single element within the parabolic GRIN MLA under illumination with TM and TE polarization, respectively. (e), (f) Cross-sectional view of simulated intensity distribution above a single element within the parabolic GRIN MLA under illumination with TM and TE polarization, respectively. In (c) – (f) the trace in the left panel is the intensity profile along the y-direction through the point

Figure 4.4 (cont.) of maximum intensity, which represents the position of the focal plane. In (c) – (f) the trace in the top panel is the intensity profile along the x-direction through the point of maximum intensity, which represents the beam width.

The application space of PSi-based GRIN MLAs can be expanded by considering GRIN profiles beyond those that are parabolic in nature. Here, we make the (ordinary) refractive index linearly increase from 1.70 to 1.74 (edge to center) and transform a rectangular Si block into a 1D PSi GRIN axicon, which is expected to possess a Bessel function-like beam intensity profile in the direction transverse to propagation (i.e., along the x-direction)[29]. The GRIN profile

$$n_o(x) = 1.74 - \alpha|x| \quad \textbf{(4.5)}$$

possessing a GRIN constant α = 0.00455 μm^{-1}, maps to a linear current density waveform

$$J(t) \cong 157 - 0.131\, t \quad [mA\, cm^{-2}] \quad \textbf{(4.6)}$$

with an etch time of ~ 104 s. After planarization, vibrant focal lines can be observed from the top for both TM (**Figure 4.5a**) and TE (**Figure 4.5b**) polarizations, with the measured TM focal position (**Figure 4.5c, trace in left panel**) agreeing well with simulation (**Figure 4.5d, trace in left panel**). The transverse TM beam profile (**Figure 4.5c, trace in top panel**) does appear to have Bessel-like sidelobes, but slightly deviates from simulation (**Figure 4.5e, trace in top panel**), likely due to surface scattering. With improved planarization, we speculate that these flat axicon MLAs could be integrated for use in NIR light-sheet[30] or lattice light-sheet microscopy[31] configurations that utilize the large focal depth of Bessel sheet beams[32,33].

Interestingly, the measured focal position under TE polarization (**Figure 4.5d, trace in left panel**) is significantly shorter than under TM polarization. This suggests that the extraordinary GRIN profile is sharper than the ordinary GRIN profile. **Figure 4.5f** is the simulated intensity distribution above a PSi axicon featuring a GRIN profile linearly increasing from 1.85 to 1.90 and given by

$$n_e(x) = 1.90 - \alpha|x| \qquad \textbf{(4.7)}$$

with α = 0.00568 μm^{-1}, which better matches our experimental TE intensity distribution, including the longitudinal and transverse intensity traces. Although this change in GRIN constant is incredibly modest, it still substantially changes the focal position. The reported current density-dependence of the birefringence of PSi[26,27], which would generate a spatially-varying birefringence in the case of shape-defined formation, readily explains the existence of a discrepancy between the GRIN profiles encountered by TM and TE polarizations.

4.5 Conclusions

In summary, shape-defined formation of PSi represents a new approach towards fabricating flat, cylindrical MLAs. We have demonstrated the process for designing the time-varying current density waveform that transforms an array of bulk Si rectangular blocks into a PSi MLA with defined GRIN profile, which can be isolated from the Si fabrication substrate for use by embedding in a transparent optical polymer, mechanically detaching, and polishing. Flat MLAs with parabolic and linear GRIN profiles, with potential utility for integration within display and microscopy systems, were both realized. Beyond these basic applications, the birefringence of PSi MLAs offers polarization-dependent focusing that is of interest to the micro- and nano-optics community[34,35] and the pursuit for full control over the vectorial nature of light in both space and time[35].

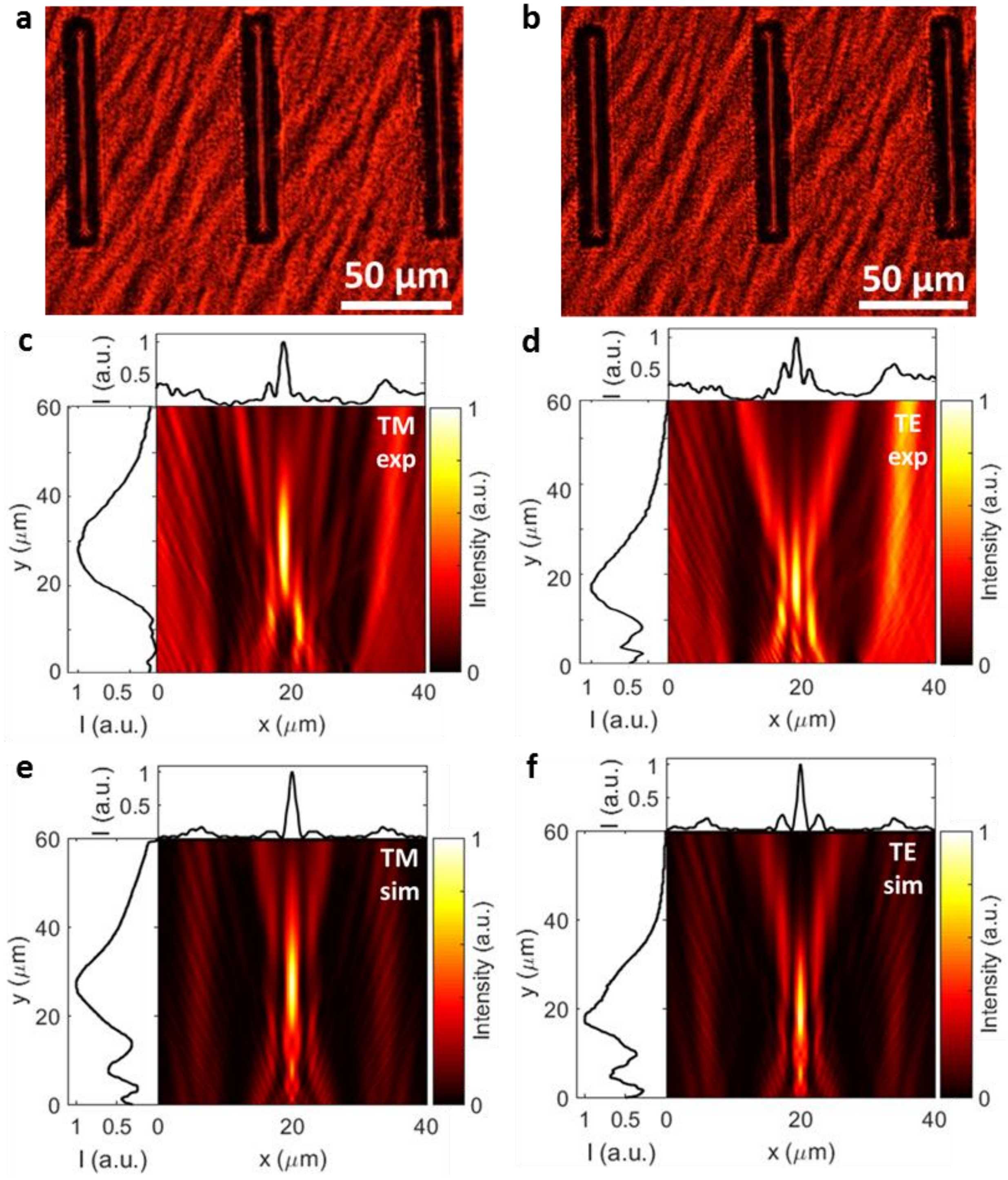

Figure 4.5. Optical characterization of a PSi GRIN MLA with linear GRIN profile. (a), (b) Top view image in focal plane of PSi GRIN MLA under illumination with TM and TE polarization, respectively. (c), (d) Cross-sectional view of experimentally collected intensity distribution above a single element within the linear GRIN MLA under illumination with TM and TE polarization, respectively. (e), (f) Cross-sectional view of simulated intensity distribution above a single element within the linear GRIN MLA under illumination with TM and TE polarization, respectively. In (c) – (f) the trace in the left panel is the intensity profile along the y-direction through the point of

Figure 4.5 (cont.) maximum intensity, which represents the position of the focal plane. In (c) – (f) the trace in the top panel is the intensity profile along the x-direction through the point of maximum intensity, which is expected to have the Bessel function-like sidelobes characteristic of an axicon (i.e., linear GRIN element).

4.6 Experimental Methods

4.6.1 Silicon rectangular blocks

Fabrication was performed on 4” diameter, highly doped (ρ ~ 0.001 – 0.005 Ω cm) p-type (100) Si wafers (Topsil). Wafers were cleaned with Nanostrip for 10 min at 70 ^{0}C, followed by deposition of ~ 1.5 µm of SiO_2 by plasma-enhanced chemical vapor deposition (Trion Minilock-Orion PECVD, located in the Micro and Nanotechnology (MNTL) cleanroom) on the backside to serve as a diffusion barrier. Dr. Seung-Kyun Kang, a post-doctoral researcher in the group of Prof. John Rogers, performed n-type doping for ~ 10 min at 1000 ^{0}C in a furnace containing a solid-state Phosphorous source. After doping, the wafer was cleaned again with Nanostrip, followed by removal of all SiO_2 by immersing in 48% hydrofluoric acid (aq) for 2 min at room temperature. Photolithography was performed by processing SPR220-4.5 (Shipley) positive photoresist under manufacturer recommended conditions and exposing with an EVG620 mask aligner (EV Group). Development with AZ MIF 917 (AZ Electronic Materials) reveals arrays of photoresist rectangles with their sides oriented such that the resulting Si rectangular block sidewalls will align with (100) degenerate crystal planes (which allows PSi etching calibration to be performed with flat pieces of (100) Si). Si etching was performed with a Pegasus ICP-DRIE (SPTS Technologies) running a Bosch process. Photolithography and DRIE were both carried out in the Micro-Nano-Mechanical Systems (MNMS) cleanroom in the Mechanical Engineering Building (MEB). After a final cleaning with Nanostrip, the Si wafer is cleaved into ~ 15 mm x 15 mm square chips containing the array of Si rectangular blocks at the center and placed in an electrochemical cell for PSi etching.

4.6.2 Porous silicon etching

Etching was carried out in a polypropylene cell with an exposed etch area of ∼1.20 cm^2. The electrolyte comprised a 1:1 volume ratio of 48% hydrofluoric acid (aq) and 100% ethanol. A 5 mm diameter Pt–Ir inoculating loop (Thomas Scientific) served as the counter electrode. Contact to the back of the Si chip containing the array of rectangular blocks was established with a stainless steel electrode. Current was delivered to the cell by an SP-200 research grade potentiostat/galvanostat (Bio-Logic Science Instruments). The current waveforms for generating GRINs were constructed via BenchLink Waveform Builder Pro software (Keysight Technologies, Inc.) and sent to the SP-200 through a 33220A Function/Arbitrary Waveform Generator (Keysight Technologies, Inc.). After etching, all samples were thoroughly rinsed with ethanol and dried under a gentle stream of nitrogen.

4.6.3 Microlens array embedding, detachment, and planarization

PSi GRIN MLAs were embedded in NOA 71 (Norland Products, Inc.) by centering the MLA within a ~ 10 mm diameter well made of cured PDMS ~ 2 – 3 mm thick. After filling the well with NOA 71, a flat slab of PDMS is laminated on top in an effort to minimize the formation of a meniscus in the NOA. The NOA 71 is then cured with ultraviolet light using the manufacturer's recommended dose. The PDMS and NOA do not stick together, so the top slab and the surrounding well can easily be removed after curing of NOA has been completed.

With the NOA cured, a razor blade is used to begin gently delaminating the NOA from the underlying Si substrate, with force applied along the width (i.e., short axis) of the lenses. With the MLA embedded in the NOA, it readily breaks off of the Si substrate, but the fracture surface, which is lower than the surrounding NOA, is not clean and needs to be planarized.

Planarization was performed by Qiujie “Jimmy” Zhao, an undergraduate research assistant in Prof. Paul Braun’s research group. To planarize, the PSi GRIN MLA embedded in NOA is placed in a reactive ion etcher (March) to selectively etch back the NOA under the following conditions: 200 W power, 200 mTorr pressure, and 20 sccm O_2 flow rate. The etching is performed in 60 sec increments until the MLA is protruding above the surrounding NOA, as determined by surface profilometry (Sloan Dektak). The PSi GRIN MLA is then polished against a cloth polishing pad (ChemoMet, Buehler) with a 20 nm colloidal silica slurry (MasterMet2, Buehler). Polishing is performed in 10 – 20 sec increments with the polishing wheel rotating at 50 rpm. Frequent optical and surface profilometry inspection are used to assess the surface and determine the relative height of the PSi MLA and NOA embedding medium. All of the equipment utilized in the planarization process is located in the Materials Research Lab (MRL).

4.6.4 Optical characterization

PSi refractive index versus wavelength information at specific fabrication current densities (**Figure 4.6**) was extracted from the reflectance spectrum of planar thin films (**Appendix A**). Reflectance spectra were collected using a Si PDA spectrometer (Control Development, Inc.) hooked up to an Axio Observer D1 inverted microscope (Carl Zeiss, Inc.) with a white-light halogen lamp serving as the source.

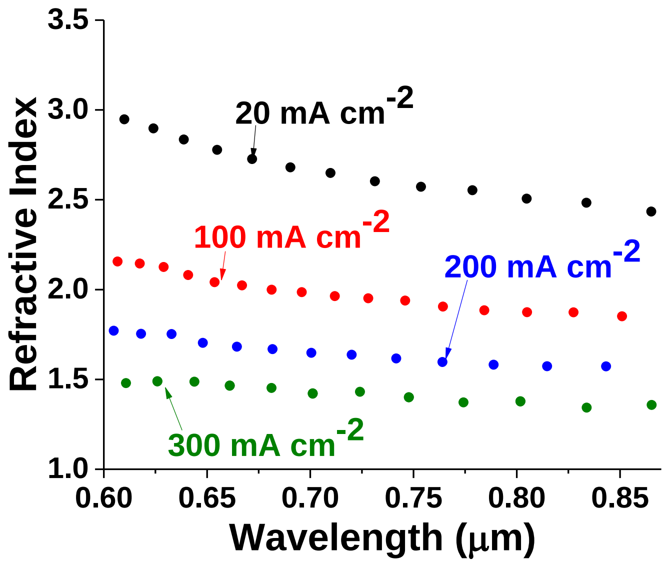

Figure 4.6. Dispersion curves associated with PSi fabricated at different current densities as determined by reflectance spectroscopy of thin films on bulk Si substrates. The process for experimentally determining the refractive index of planar PSi films is outlined in **Appendix A**.

The intensity distribution of the light transmitted through the elements in the PSi GRIN MLA was measured at Stanford University by graduate student Aaron Holsteen using a confocal microscope (Nikon Eclipse, C1) in the lab of Prof. Mark Brongersma. The setup, shown in **Figure 4.7**, uses a white light supercontinuum illumination source that is wavelength-tunable from 400 to 2200 nm (NKT, SuperK Extreme). A linear polarizer and a half waveplate are utilized to generate a linearly polarized illumination beam. The NOA slab with embedded PSi GRIN MLA is mounted on a XYZ scan stage, such that the planarized surface faces upwards towards the microscope objective, and is illuminated from below with the laser beam set to 800 nm. The light intensity in the x-z plane above a single GRIN lens is gathered using a 100X objective with a numerical aperture of 0.9 and captured by a high-resolution CCD camera (Princeton Instruments, PIXIS 1024B). By stepping the stage in 500 nm increments, images in the x-z plane can be stacked in the y dimension to construct the light intensity volume above a single element in the PSi GRIN MLA.

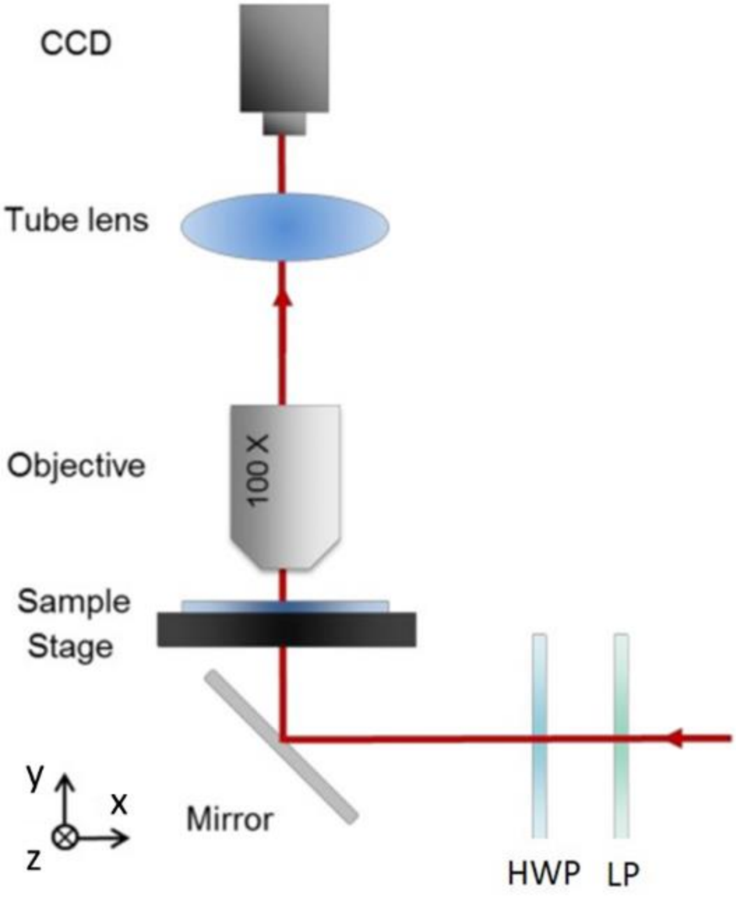

Figure 4.7. Schematic of the optical setup used by graduate student Aaron Holsteen to characterize PSi GRIN MLAs. A polarized and collimated laser beam with wavelength 800 nm is sent into a confocal microscope and propagates upward through the bottom of the sample stage, interrogating the sample. The sample stage is translated in the y-direction in discrete, 500 nm steps in order to collect various x-z plane intensity distributions, which are later stacked to recreate the intensity profile transmitted by the PSi GRIN MLA. The optical setup is located in the lab of Prof. Mark Brongersma at Stanford University.

4.7 References

1. Marchand, E. W. in *Gradient Index Optics* 1–6 (Academic Press, 1978).
2. Miller, S. E. Light Propagation in Generalized Lens-Like Media. *Bell Syst. Tech. J.* **44,** 2017–2064 (1965).
3. Maxwell, J. C. *The scientific papers of James Clerk Maxwell*. **2,** (Cambridge, University Press, 1890).

4. Luneburg, R. K. *Mathematical Theory of Optics*. (University of California Press, 1964).

5. Di Falco, A., Kehr, S. C. & Leonhardt, U. Luneburg lens in silicon photonics. *Opt. Express* **19,** 5156–5162 (2011).

6. Wood, R. W. *Physical optics*. (New York : The Macmillan Company, 1905).

7. Leonhardt, U. & Philbin, T. G. in *Progress in Optics* (ed. Wolf, E.) **53,** 69–152 (Elsevier, 2009).

8. Moore, D. T. Gradient-index optics: a review. *Appl. Opt.* **19,** 1035–1038 (1980).

9. Hashizume, H., Hamanaka, K., Graham III, A. C. & Zhu, X. F. Future of gradient index optics. in *Proc. SPIE* **4437,** 26–39 (2001).

10. Kawazu, M. & Ogura, Y. Application of gradient-index fiber arrays to copying machines. *Appl. Opt.* **19,** 1105 (1980).

11. Wang, P. Y. Beam-shaping optics deliver high-power beams. *Laser Focus World* **37,** 115 (2001).

12. Gal, M., Reece, P. J., Zheng, W. & Lerondel, G. Porous silicon: a versatile optical material. in *Proc. SPIE* **5277,** 9–16 (2004).

13. Ilyas, S. & Gal, M. Optical devices from porous silicon having continuously varying refractive index. *J. Mater. Sci. Mater. Electron.* **18,** 61–64 (2007).

14. Smith, R. L. & Collins, S. D. Porous silicon formation mechanisms. *J. Appl. Phys.* **71,** R1–R22 (1992).

15. Zhang, X. G. Morphology and Formation Mechanisms of Porous Silicon. *J. Electrochem. Soc.* **151,** C69–C80 (2004).

16. Frohnhoff, S. & Berger, M. G. Porous silicon superlattices. *Adv. Mater.* **6,** 963–965 (1994).

17. Vincent, G. Optical properties of porous silicon superlattices. *Appl. Phys. Lett.* **64,** 2367–2369 (1994).

18. Mulloni, V. & Pavesi, L. Porous silicon microcavities as optical chemical sensors. *Appl. Phys. Lett.* **76,** 2523–2525 (2000).

19. Rong, G., Najmaie, A., Sipe, J. E. & Weiss, S. M. Nanoscale porous silicon waveguide for label-free DNA sensing. *Biosens. Bioelectron.* **23,** 1572–1576 (2008).

20. Link, J. R. & Sailor, M. J. Smart dust: Self-assembling, self-orienting photonic crystals of porous Si. *Proc. Natl. Acad. Sci.* **100,** 10607–10610 (2003).

21. Bjorklund, R. B., Zangooie, S. & Arwin, H. Adsorption of Surfactants in Porous Silicon Films. *Langmuir* **13,** 1440–1445 (1997).

22. Anderson, M. A. *et al.* Sensitivity of the optical properties of porous silicon layers to the refractive index of liquid in the pores. *Phys. Status Solidi A* **197,** 528–533 (2003).

23. Lin, V. S.-Y., Motesharei, K., Dancil, K.-P. S., Sailor, M. J. & Ghadiri, M. R. A Porous Silicon-Based Optical Interferometric Biosensor. *Science* **278,** 840–843 (1997).

24. Teichman, J., Holzer, J., Balko, B., Fisher, B. & Buckley, L. Gradient Index Optics at DARPA. (2013).

25. Astrova, E. V., Ulin, V. P., Zharova, Y. A., Shul'pina, I. L. & Nashchekin, A. V. Anisotropy Effects in Electrochemical Etching of p+-Si. *J. Electrochem. Soc.* **159,** D172–D180 (2012).

26. Kashkarov, P. K. *et al.* Photonic bandgap materials and birefringent layers based on anisotropically nanostructured silicon. *J. Opt. Soc. Am. B* **19,** 2273 (2002).

27. Ishikura, N., Fujii, M., Nishida, K., Hayashi, S. & Diener, J. Dichroic rugate filters based on birefringent porous silicon. *Opt. Express* **16,** 15531 (2008).

28. Ares, M., Royo, S. & Caum, J. Shack-Hartmann sensor based on a cylindrical microlens array. *Opt. Lett.* **32,** 769 (2007).

29. Lin, D., Fan, P., Hasman, E. & Brongersma, M. L. Dielectric gradient metasurface optical elements. *Science* **345,** 298–302 (2014).

30. Huisken, J. & Stainier, D. Y. R. Selective plane illumination microscopy techniques in developmental biology. *Development* **136,** 1963–1975 (2009).

31. Chen, B.-C. *et al.* Lattice light-sheet microscopy: Imaging molecules to embryos at high spatiotemporal resolution. *Science* **346,** 1257998 (2014).

32. Mondal, P. P. Temporal resolution in fluorescence imaging. *Nanobiotechnology* **1,** 11 (2014).

33. Planchon, T. A. *et al.* Rapid three-dimensional isotropic imaging of living cells using Bessel beam plane illumination. *Nat. Methods* **8,** 417–423 (2011).

34. Ye, X., Zhang, F., Ma, Y. & Qi, L. Brittlestar-Inspired Microlens Arrays Made of Calcite Single Crystals. *Small* **11,** 1677–1682 (2015).

35. Schmid, D. *et al.* Adjustable and robust methods for polarization-dependent focusing. *Opt. Express* **21,** 15538 (2013).

CHAPTER 5

TRANSFORMING POROUS SILICON TEMPLATES INTO VISIBLY TRANSPARENT GRADIENT REFRACTIVE INDEX PHOTONIC ELEMENTS

5.1 Introduction and Motivation

Porous silicon (PSi) first caught the attention of the photonics community as a potential route towards Si-based light sources owing to its observed visible light emission[1,2]. While intrinsic material limitations have prevented PSi from overtaking state-of-the-art light-emitting technology, PSi has remained interesting because of its versatility as an optical material[3]. The optical properties (e.g., refractive index) of PSi, which depend heavily on the porosity (i.e., void fraction), are defined by the applied current density during electrochemical etching[4]. Consequently, a time-varying current density can be used to program a gradient refractive index (GRIN) along the PSi etch pathway, an approach that has enabled 1D GRIN elements such as distributed Bragg reflectors (DBRs)[5,6], rugate filters[7,8], and vertical microcavities[9–11]. In addition, the optical response of PSi is highly sensitive to foreign media penetrating its porous microstructure[12–14], which, in combination with the well-defined optical signature of PSi 1D GRIN elements, provides a powerful platform for chemical and biological sensing[14–19].

The large refractive index contrast (~ 1.0 refractive index unit) accessible with PSi is excellent for IR and NIR GRIN elements[20]. However, the presence of Si makes PSi GRIN elements highly absorptive in the visible spectrum. Extending the optical functionality of PSi GRIN elements to visible wavelengths thus requires the elimination of the Si absorbing volume. The simplest means of accomplishing this is by oxidizing PSi into porous silicon dioxide ($PSiO_2$)[21,22].

While oxidation extinguishes absorption, it also greatly limits the achievable refractive index range due to the reduced refractive index contrast between the SiO_2 scaffold and air.

Alternatively, PSi (or $PSiO_2$) can be used as a sacrificial template. In this approach, materials are introduced into the pores and the Si (or SiO_2) backbone is dissolved, leaving behind an optically transparent structural inversion of the initial PSi GRIN scaffold. To date, both PSi and $PSiO_2$ have successfully served as sacrificial templates[23,24]. But, these efforts have only demonstrated inversion into polymers like polystyrene or silicone[23], which offer no optical advantage over $PSiO_2$ in terms of refractive index contrast, or carbon[24], which lacks transparency in the visible spectrum. Transparent, high refractive index materials like ZnO[25], TiO_2[26], or SnO_2[27] have been deposited into PSi templates, but this has been accomplished with sol-gel chemistry[25,26] and atomic layer deposition[27], neither of which densely fill the PSi void volume for inversion. Beyond these, a great deal of the work using PSi as a host material[28] has focused on depositing metals[29,30], which are opaque at visible wavelengths, or the use of macroporous templates[31,32], which possess large pore dimensions that generate significant scatterings losses and inhibit visible frequency applications.

Here, we combine thermal oxidation and material infiltration to transform PSi templates into visibly transparent GRIN photonic elements. By coupling reflectance and transmittance spectroscopy with thin-film optical analysis, thermal oxidation is shown to impart transparency on PSi by converting it to $PSiO_2$, while subsequent infiltration with TiO_2 by way of atomic layer deposition (ALD) creates a $PSiO_2/TiO_2$ composite with tunable optical properties. This conversion methodology is applied to a discrete GRIN stack (i.e., a DBR) and the optical evolution of the element is readily predicted from the analysis of optically homogeneous $PSiO_2/TiO_2$ thin films. Finally, a radial GRIN PSi film is converted into a $PSiO_2$ template possessing a lens-like parabolic phase profile with an effective radius of curvature that is strongly enhanced by its transformation into a $PSiO_2/TiO_2$ composite element.

5.2 Material transformation of porous silicon templates: process and characterization

The process for converting a PSi template into a $PSiO_2/TiO_2$ element is depicted in **Figure 5.1**. After a PSi template is electrochemically etched into a Si wafer it can be electrochemically detached from the Si wafer and transferred to a transparent, thermally-stable quartz substrate under a gentle stream of ethanol. After carefully rinsing with hexanes to limit capillary forces[33] and drying in air, the PSi is left in intimate contact with the quartz substrate. The PSi on quartz is then subjected to a two-part thermal oxidation, first being exposed to a dry oxygen atmosphere at 500 ^{0}C to stabilize the microstructure[34] and then at 900 ^{0}C to fully convert PSi into $PSiO_2$. Finally, the $PSiO_2$ film on quartz is infiltrated with TiO_2 by means of atomic layer deposition (ALD), creating a $PSiO_2/TiO_2$ composite with an optical response tuned by the extent of filling.

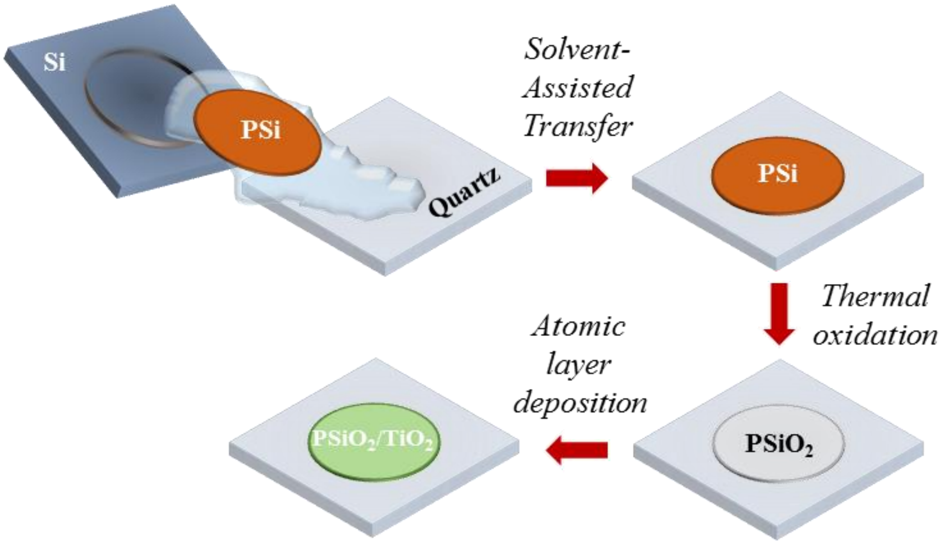

Figure 5.1. Schematic representing the process flow for transforming an absorptive PSi template into a transparent, functional $PSiO_2/TiO_2$ optical composite.

To characterize the optical evolution, reflectance and transmittance spectra are collected from optically homogeneous films (i.e., PSi template etched at single current density) at various stages of the conversion (**Figure 5.2, top row**) and used to extract (see **Appendix A**) the refractive index and the extinction coefficient (**Figure 5.2, bottom row**). As-fabricated, PSi is highly dispersive with a non-zero extinction coefficient (**Figure 5.2, lower left**), which is manifested in a transmittance that drops off steeply towards shorter wavelengths (**Figure 5.2, upper left**). Oxidation eliminates the absorptive Si scaffold and its associated extinction coefficient (**Figure 5.2, lower middle**), with $PSiO_2$ exhibiting high transmittance (**Figure 5.2, upper middle**). Gradual TiO_2 infiltration incrementally increases the refractive index (**Figure 5.2, lower right** and **Figure 5.3**) while maintaining the transparency (**Figure 5.2, upper right**) offered by pure $PSiO_2$.

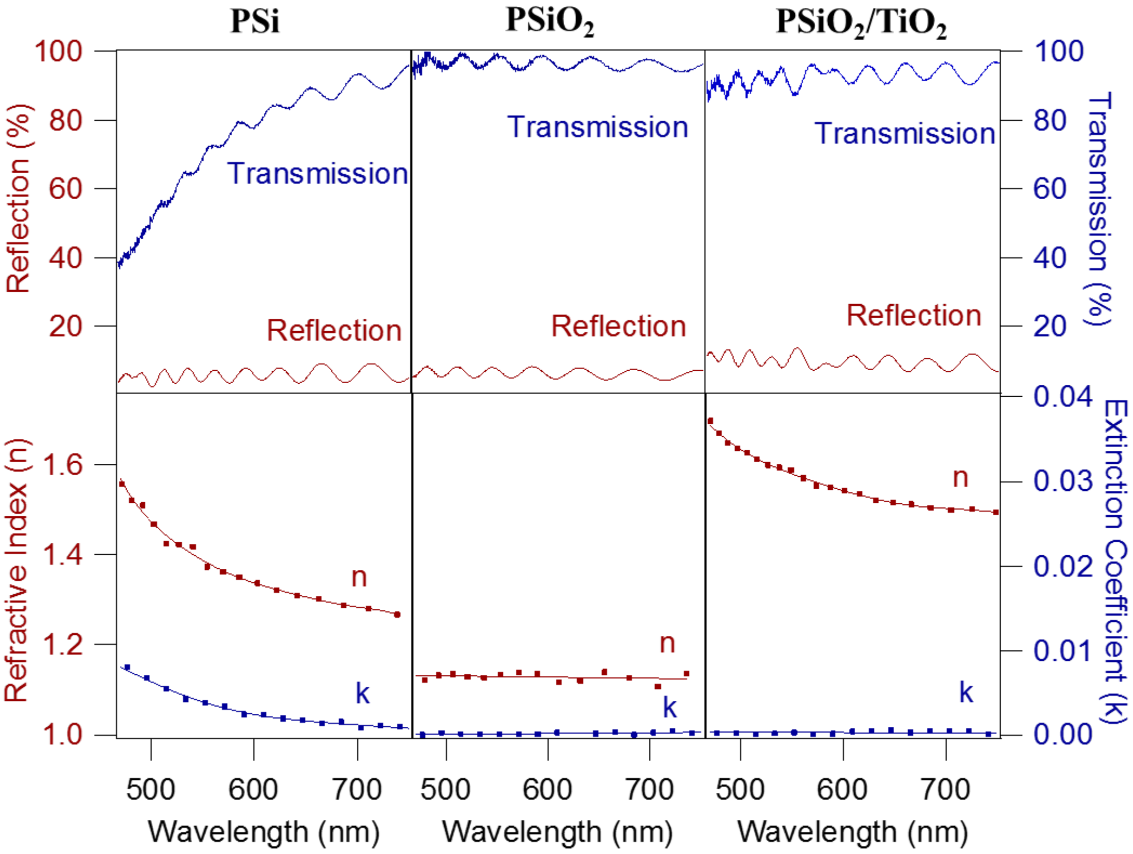

Figure 5.2. The evolution of optical response during PSi template transformation. As-fabricated, the PSi template is highly absorptive (upper left) and dispersive (lower left) owing to the presence

Figure 5.2 (cont.) of Si. Oxidation transforms the PSi template into a transparent (upper middle) PSiO2 film with lower refractive index (bottom middle). Infiltration with TiO2 by way of ALD maintains the transparency of PSiO2 (upper right) with the reduced transmittance being not a result of absorption, but of increased reflectance (upper right) owing to the increased refractive index of PSiO2/TiO2 (lower right).

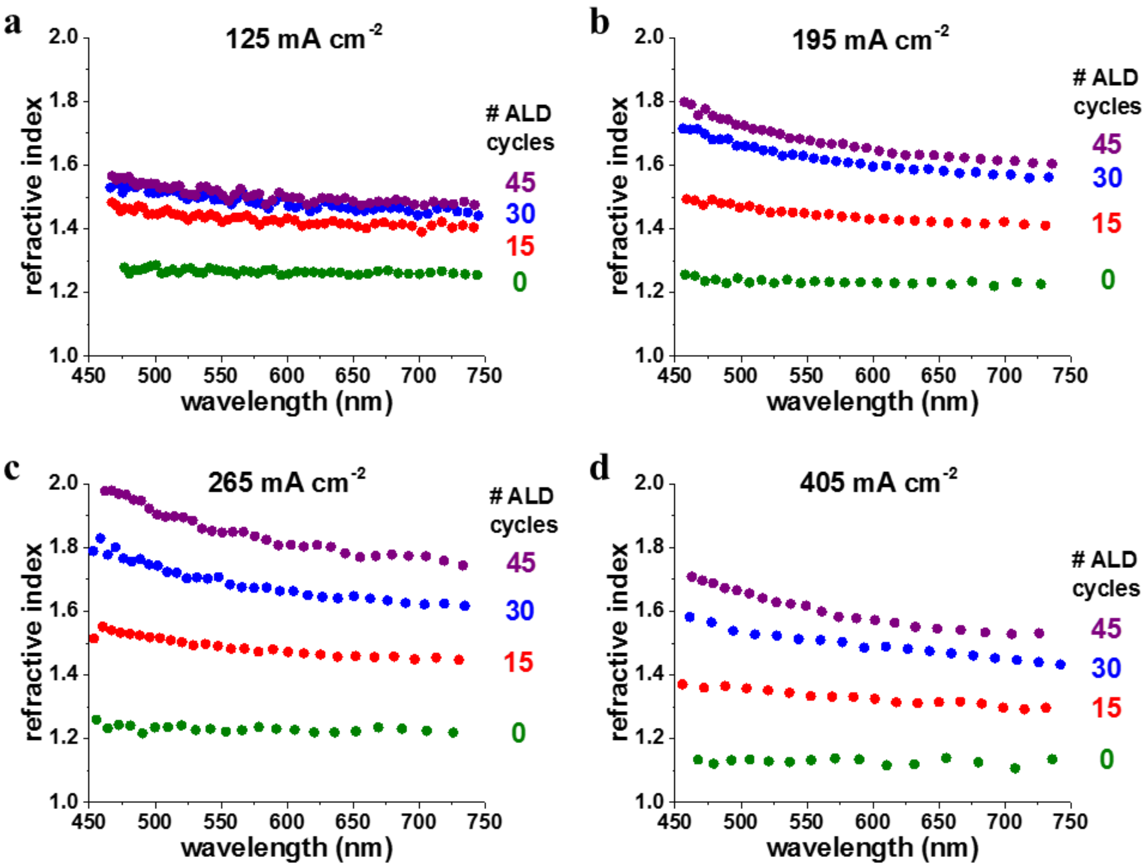

Figure 5.3. Dispersion curves for optically homogeneous templates etched with an electrochemical current density of (a) 125 mA cm^{-2}, (b) 195 mA cm-^{2}, (c) 265 mA cm^{-2}, and (d) 405 mA cm^{-2} that have been oxidized and subjected to different levels of TiO_2 infiltration, as indicated by the number of ALD cycles with 0 cycles corresponding to pure $PSiO_2$.

The observed increase in the refractive index of $PSiO_2/TiO_2$ is consistent with the introduced TiO_2 reducing the void volume of $PSiO_2$ (**Figure 5.4a**) in accordance with the three-component Bruggeman effective medium approximation (EMA)

$$0 = \phi_{Sio_2}\left(\frac{n_{SiO_2}^2 - n_{PSiO_2/TiO_2}^2}{n_{SiO_2}^2 - 2\,n_{PSiO_2/TiO_2}^2}\right) + \phi_{Void}\left(\frac{n_{void}^2 - n_{PSiO_2/TiO_2}^2}{n_{void}^2 - 2\,n_{PSiO_2/TiO_2}^2}\right) + \phi_{TiO_2}\left(\frac{n_{TiO_2}^2 - n_{PSiO_2/TiO_2}^2}{n_{TiO_2}^2 - 2\,n_{PSiO_2/TiO_2}^2}\right) \qquad \textbf{(5.1)}$$

where n_{PSiO_2/TiO_2} represents the effective refractive index of the PSiO$_2$/TiO$_2$ composite, while ϕ is the volume fraction of the indicated material component with

$$\phi_{SiO_2} + \phi_{Void} + \phi_{TiO_2} = 1 \tag{5.2}$$

The value of n_{void} = 1, while n_{SiO_2} is described by[35]

$$n_{SiO_2}^2 - 1 = \frac{0.6961663\lambda^2}{\lambda^2-0.0684043^2} + \frac{0.4079426\lambda^2}{\lambda^2-0.1162414^2} + \frac{0.8974794\lambda^2}{\lambda^2-9.896161^2} \tag{5.3}$$

and n_{TiO_2} is given by[36]

$$n_{TiO_2}^2 = 5.913 + \frac{0.2441}{\lambda^2-0.0803} \tag{5.4}$$

with λ representing the wavelength of light in units of micrometers (μm). Applying **Equations (5.1)** and **(5.2)** to the measured effective refractive index post-oxidation (ϕ_{TiO_2} = 0) generates information about void and SiO$_2$ volume fractions, while applying **Equations (5.1)** and **(5.2)** after infiltration describes how much void volume is replaced by TiO$_2$.

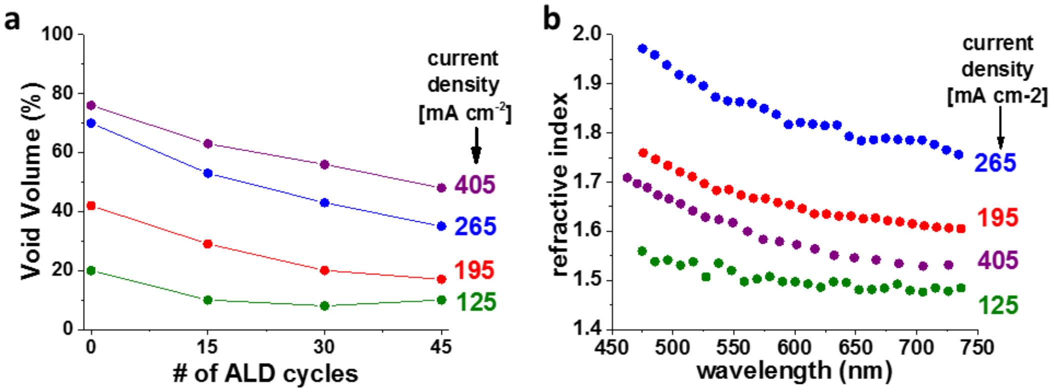

Figure 5.4. Optical implications of variable filling capacity between templates. (a) The increased refractive index observed when filling optically homogeneous templates is a result of void volume being consumed by TiO$_2$, as described by the Bruggeman EMA. Templates fabricated with larger current densities, which possess a larger porosity, are able to accommodate more TiO$_2$ within the microstructure. (b) The variable filling capacity of different porosity templates can lead to initially higher porosity (and thus lower refractive index) templates to have their refractive index increase more than lower porosity templates, leading to optical inversion.

Films prepared with higher current densities (265 and 405 mA cm^{-2}) possess more void volume that is continuously replaced with TiO_2 through 45 ALD cycles, while the film prepared at the lowest current density (125 mA cm-^{2}) is incapable of accommodating TiO_2 beyond 15 ALD cycles. As a result, the dispersion for the series of optically homogeneous films (**Figure 5.4b**) does not feature the clear current density-dependent trend of PSi and $PSiO_2$ (i.e., lowest current density yields highest refractive index). Instead, the refractive index associated with higher current density fabrication can be seen to surpass that associated with lower current density fabrication after oxidation and TiO_2 infiltration. This is an important point of consideration for designing GRIN templates, as the GRIN profile can be "optically inverted" during conversion to $PSiO_2/TiO_2$.

5.3 Discrete gradient refractive index superlattice template

The simple, discrete GRIN profile of DBRs and microcavities make these elements easily fabricated with PSi for sensing[15,19,37] and optoelectronic applications[38–40]. While these PSi-based elements have been applied at visible wavelengths, they are limited to applications that only require high reflectance or are not adversely affected by absorption. To extend the functionality of these porous GRIN stacks to low absorption applications at visible frequencies, a 30-period PSi DBR is fabricated with alternating current density pulses of 265 and 405 mA cm^{-2}, generating a stopband located at 530 nm with poor out-of-band transmittance (**Figure 5.5**).

The measured post-oxidation stopband is located at ~ 440 nm (**Figure 5.6, top purple trace**), which is slightly (~ 10 nm) blue-shifted from transfer-matrix calculations[41] (**Figure 5.6, bottom purple trace**) combining the EMA data from **Figure 5.4a** and the thicknesses of the layers (~90 nm and ~114 nm) as determined by a cross-sectional scanning electron micrograph. The out-of-band transmittance of the $PSiO_2$ DBR is markedly improved compared to the PSi template, but the photonic strength is diminished from the reduced refractive index contrast.

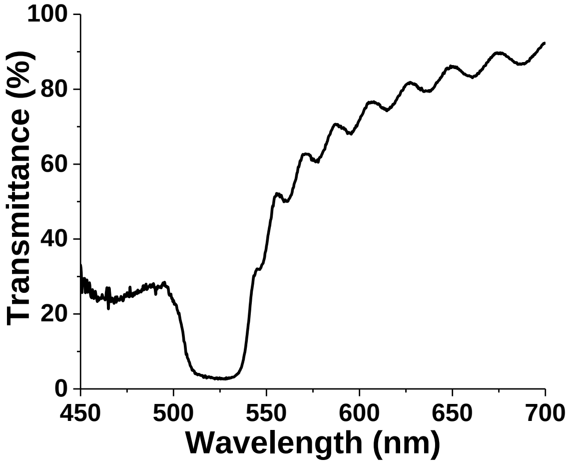

Figure 5.5. Measured transmittance spectrum from a 30-period PSi DBR template.

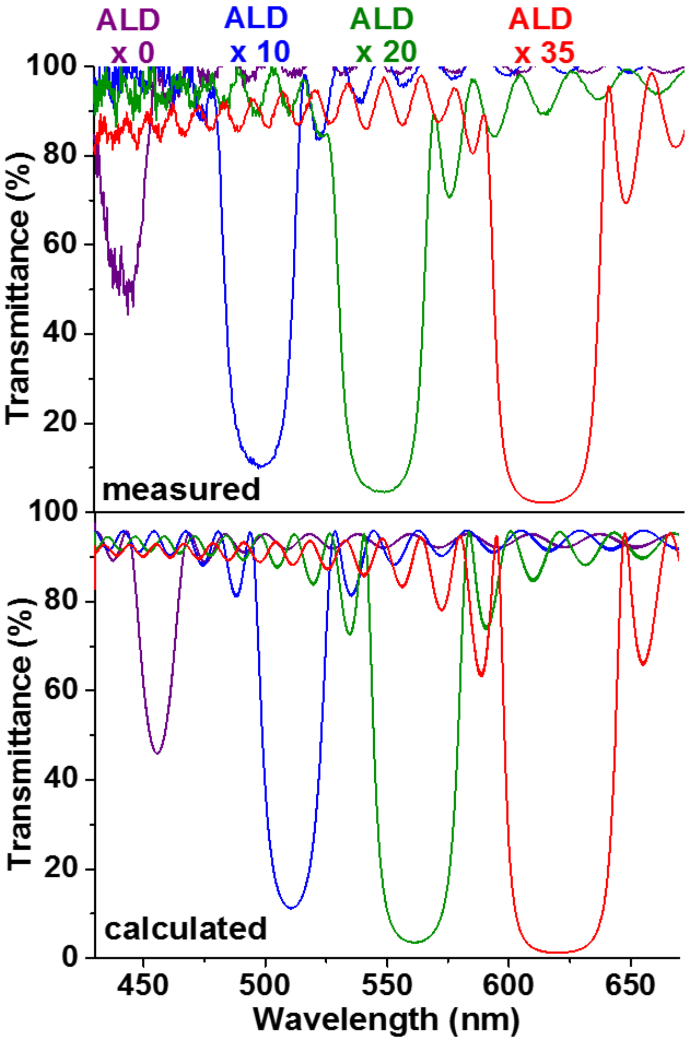

Figure 5.6. Comparison of the measured optical evolution of a PSi DBR template (top) with the calculated evolution (bottom) determined transfer matrix-based simulations.

After just 10 cycles of TiO_2 ALD, the measured stopband red-shifts to ~ 492 nm (**Figure 5.6, top blue trace**) and the photonic strength is noticeably restored. The measured spectral position of the stopband is again slightly blue-shifted from calculation (**Figure 5.6, bottom blue trace**) and remains so with further filling (**Figure 5.7a**), but we find that the calculated shift of the stopband positon is in excellent agreement with measurements (**Figure 5.7b**).

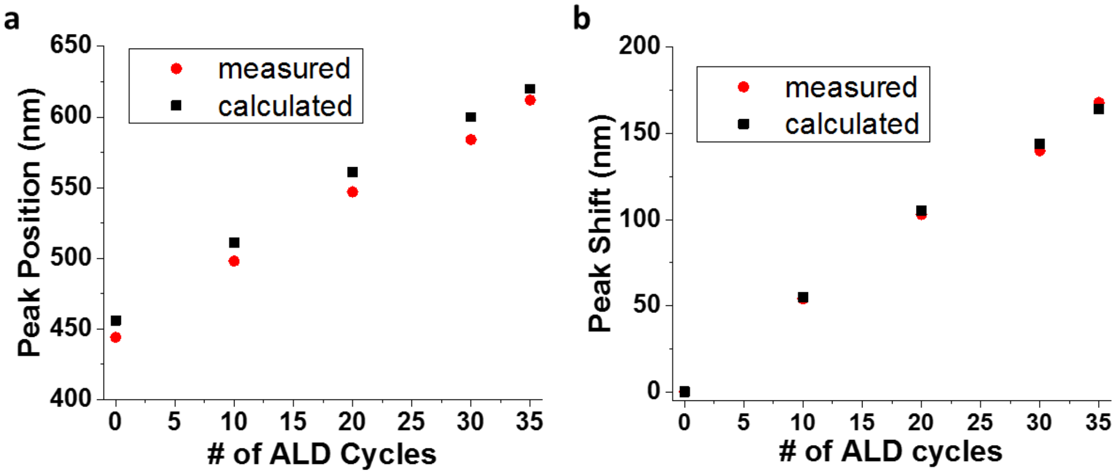

Figure 5.7. (a) The measured peak positions from the transformed PSi DBR template are consistently blue-shifted relative to the calculated peak positions. (b) While there is a small discrepancy between measured and calculated absolute peak position, the relative shift of the measured and calculated peaks is in excellent agreement.

Given the high photonic strength and the transparency that are attainable, $PSiO_2/TiO_2$ 1D GRIN structures lend well to absorption-sensitive applications such as emission modification. Building upon demonstrations with PSi, monolithic $PSiO_2/TiO_2$ microcavities could serve as hosts to nanoscale emitters[42,43] while other classes of emitters may potentially be integrated between $PSiO_2/TiO_2$ DBRs to form hybrid light-emitting modules[44]. Beyond emission modification, there is also the possibility to use $PSiO_2/TiO_2$ 1D GRIN stacks in a transmission-based sensing or spectral filtering capacity. Unfortunately, the conformal nature of the ALD process demonstrated here means that the filling capacity of a discrete GRIN is set by the lowest void volume in the stack, limiting the refractive index contrast to a modest level (~ 0.1 – 0.3 refractive index unit). This could be remedied by the development of a nanoscale bottom-up deposition technique to densely fill $PSiO_2$, greatly enhancing the available refractive index contrast for $PSiO_2/TiO_2$ discrete GRIN stacks and expanding their utility to applications like spectrally-selective filters for photovoltaics[45–47].

5.4 Continuous radial gradient refractive index template

The ease with which the refractive index of PSi is modulated can also be extended to 2D and 3D GRIN templates. While 1D GRIN PSi is generated from a time-varying current density, 2D or 3D GRIN PSi requires a spatially-varying current density, which has been used to create lateral GRIN filters[48,49] and GRIN lens-like films[50]. We constructed a 2D GRIN PSi template by applying a constant current density with a "pin" electrode positioned in close proximity (~2 mm) to the Si surface (**Figure 5.8a**). This results in a radially-varying current density that manifests in the concentric fringes observed from the PSi template (**Figure 5.8b**).

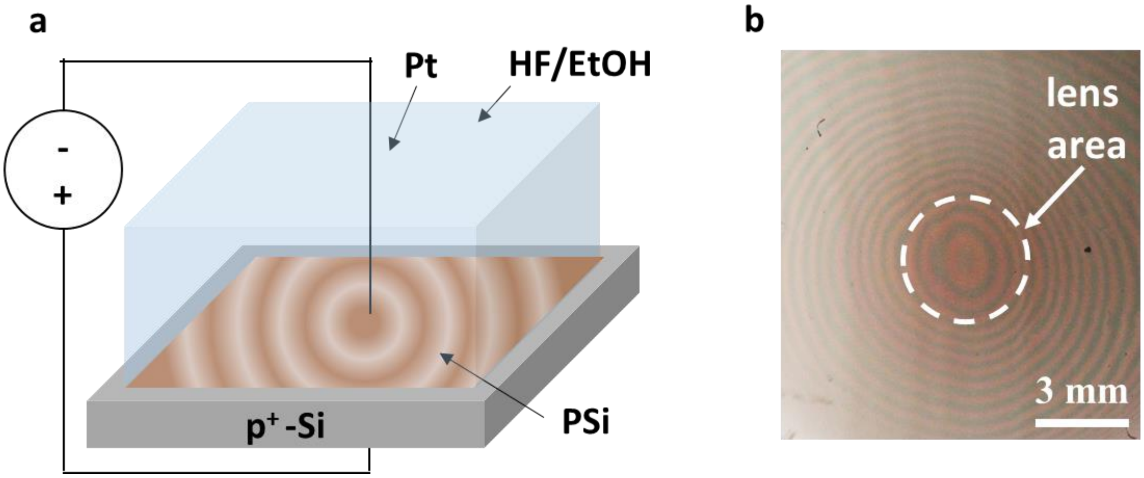

Figure 5.8. A simple radial GRIN PSi template. (a) By placing a Pt pin electrode in close proximity to the Si wafer etching surface, a radially-varying current density profile is generate. (b) The resulting radially-varying current density profile creates a radial GRIN that manifests in the concentric fringes observed from the PSi template.

The radial thickness profile (**Figure 5.9a**) and the GRIN profile (**Figure 5.9b**) are determined after oxidizing the PSi template by performing spatially-resolved scanning electron microscopy and reflectance spectroscopy, respectively. While the $PSiO_2$ GRIN profile mimics that of a diverging lens, the calculated phase profile (**Figure 5.9c, blue trace**) experienced by an electromagnetic wave interacting with the structure has a converging lens-like parabolic shape and a theoretical focal length (f) of 1.48 m according to[51]

$$\Delta\phi(r) = \frac{-\pi}{\lambda f} r^2 \qquad \textbf{(5.5)}$$

where λ is the wavelength of light (630 nm here) and r is the radial position. The theoretical capacity of such a $PSiO_2$ radial GRIN element to function as a focusing lens indicates that its interaction with light is dominated by the physical thickness profile. Still, the GRIN profile contributes to the element's phase behavior, allowing the light-matter interaction to be tuned by modulating the GRIN profile. After applying 60 cycles of TiO_2 ALD, the $PSiO_2/TiO_2$ element's GRIN profile (**Figure 5.9b, red trace**) is inverted compared to bare $PSiO_2$. This is readily explained by the ability of higher void volume $PSiO_2$ to accommodate more TiO_2. Consequently, the GRIN profile and physical thickness profile are made to work in concert, noticeably sharpening the phase-space radius of curvature (**Figure 5.9c, red trace**) and reducing the theoretical focal length of the $PSiO_2/TiO_2$ radial GRIN element to 0.80 m.

It is noted that efforts were made to experimentally measure the focal length, but this proved difficult owing to aberrations introduced during the initial PSi template fabrication, as well as issues with delamination of the element from quartz during the thermal oxidation process that prevented the element from lying flat on the quartz substrate. As such, we were unable to directly observe the focusing behavior of the transformed radial GRIN element.

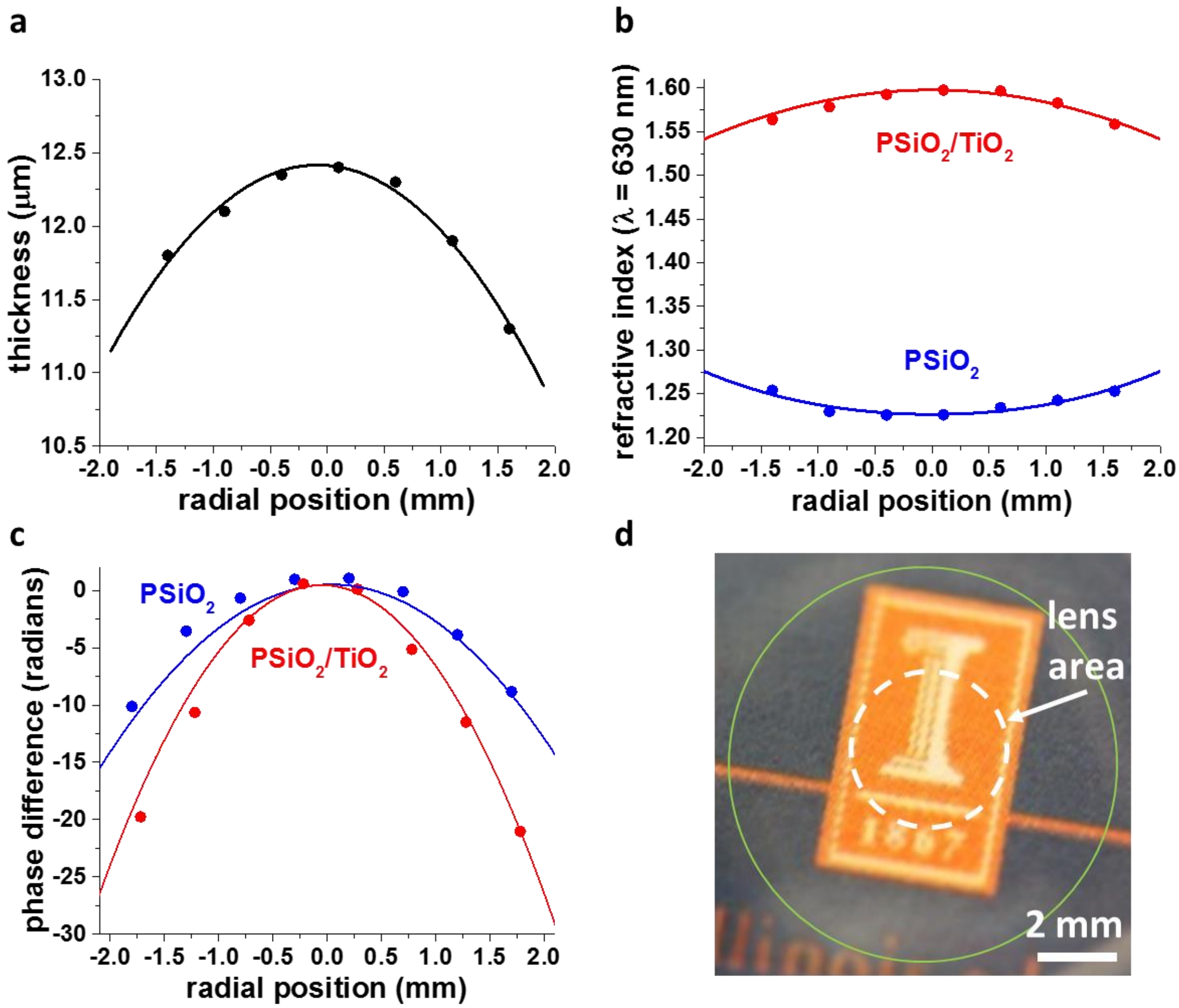

Figure 5.9. Optical characterization of a transformed radial GRIN PSi template. (a) The radial thickness profile as determined by cross-sectional SEM imaging after oxidation of the PSi template. (b) The GRIN profile post-oxidation (blue) and after 60 cycles of TiO_2 ALD infiltration (red trace). The variable filling capacity of the spatially-varying porosity results in the GRIN profile becoming optically inverted. The points correspond to measured points, while the solid lines represent quadratic fits. (c) The calculated (using the information in parts (a) and (b)) phase profile for light encountering the radial GRIN element. Both $PSiO_2$ (blue) and $PSiO_2/TiO_2$ (red) exhibit a converging lens-like parabolic profile, but the $PSiO_2/TiO_2$ features a sharper curvature because its GRIN profile works in concert with the physical thickness profile. The points correspond to measured points, while the solid lines represent a quadratic fit to **Equation (5.5)**. (d) Top view optical image of the radial GRIN $PSiO_2/TiO_2$ element on quartz. The green circle roughly indicates the border of the entire $PSiO_2/TiO_2$ film, while the dashed white circle indicates the measured "lensing" region.

While the large theoretical focal length of the $PSiO_2/TiO_2$ radial GRIN lens limits the available applications, it could be utilized in low-numerical aperture configurations such as collimators for narrow laser beam divergence. To expand the general applicability of $PSiO_2/TiO_2$ GRIN elements, one can couple photonic design with more sophisticated PSi template fabrication. This is particularly promising in light of the recent demonstration of photo-mediated PSi etching for constructing macroscale transformation optics[52]. By using a photoelectrochemically-defined PSi template, it may be possible to realize $PSiO_2/TiO_2$ macroscale transformation optics that exhibit broadband functionality at visible wavelengths.

5.5 Conclusions

In conclusion, we have shown that the combination of thermal oxidation and TiO_2 infiltration by ALD offers an opportunity to fabricate visibly transparent GRIN optical elements from absorptive PSi templates. Optical characterization of homogeneous PSi confirms that thermal oxidation creates transparent $PSiO_2$ that is transformed into a $PSiO_2/TiO_2$ composite upon infiltration, with an optical response governed by the filling fractions. By applying the conversion methodology to a PSi DBR template, we demonstrate the controllability of the process by closely predicting the spectral evolution of the element during its transformation from PSi to $PSiO_2/TiO_2$. Further, we expanded the conversion to a 2D radial GRIN template, constructing a transparent element with a focal length adjusted by the introduction of TiO_2. Coupling the transparency of $PSiO_2/TiO_2$ with the complex GRIN architectures accessible with PSi photonic templates may enable the fabrication of complex GRIN elements and phase-shaping optics at visible wavelengths.

5.6 Experimental Methods

5.6.1 Porous silicon etching and electropolishing

All PSi templates were formed from single-side polished, highly-doped ($\rho \sim 0.001$-0.005 Ω cm) p-type Si (Prolog Semicor Ltd). Etching was carried out in a polypropylene cell with an exposed etch area of ~ 1.20 cm^2. Contact to the back of the Si wafer was established with a stainless steel electrode. Current was delivered to the cell by an SP-200 Research Grade Potentiostat/Galvanostat (Bio-Logic Science Instruments) and pulsed with a duty cycle of 33% at a frequency of 1.33 Hz (unless specified otherwise). After etching, all templates were throughly rinsed with ethanol. The electrolyte was comprised of a 1:1 volume ratio of 48% hydrofluoric acid (aq) (Sigma-Aldrich) and 100% ethanol (Decon Labs). A 5 mm diameter Pt-Ir inoculating loop (Thomas Scientific) served as the counter electrode (except for radial GRIN templates, discussed below) and was located at the center of the cell ~25mm from the etch surface to provide a uniform current density across the sample..

The radial GRIN PSi template was formed using the process described above with the exception that Pt-Ir pin placed ~2-3 mm from the etch surface served as the counter electrode. A current density of 150 mA cm^{-2} was applied with the aforementioned duty cycle and pulse frequency.

Electropolishing was carried out with an electrolyte comprised of a 1:3 volume ratio of 48% hydrofluoric acid (aq) and 100% ethanol. The 5 mm Pt-Ir ring served as the counter electrode and a current density of 300 mA cm^{-2} was applied with a duty cycle of 20% at a frequency of 0.40 Hz. Before the electrochemically-induced detachment, a stainless steel syringe needle was used to mechanically score and release the edges of the PSi template to allow the film to remain flat for printing. After the electropolishing process, all PSi templates were carefully rinsed with ethanol in such a fashion that the free-standing PSi template glided from the Si wafer and onto a 25 mm × 25 mm × 1 mm quartz slide. Once on the quartz substrate, all PSi templates were then gently rinsed with hexanes and allowed to dry in air.

5.6.2 Thermal oxidation

Thermal oxidation was performed by Christian Ocier, a fellow graduate student in Prof. Paul Braun's research group. Dried PSi templates on quartz were loaded into an alumina, centered within an alumina furnace tube, and loaded into CM 1600 Series Furnace connected to a dual argon (Ar) and oxygen (O_2) inlet. Under Ar flow, the temperature of the furnace was increased from room temperature to 500 ºC at 200 ºC/hour. Next, the Ar flow was replaced with O_2 gas and held for 1 hour at 500 ºC. After purging O_2 from the furnace, the temperature was increased to 925 ºC at a rate of 125 ºC/hour under flowing Ar. Again, O_2 gas replaced Ar and the furnace was held at 925 ºC for 1 hour in order to fully oxidze the PSi template into $PSiO_2$. After oxidation, the furnace was purged with Ar and then cooled to room temperature at a rate of 125 ºC/hour with Ar flowing. The furnace is located in the Micro/Nanofabrication Facility of the Materials Research Lab (MRL)

5.6. 3 Atomic layer deposition

ALD infiltration of $PSiO_2$ with TiO_2 was performed by Christian Ocier, a fellow graduate student in Prof. Paul Braun's research group. The ALD system (Cambridge Nanotech) used water and tetrakis(dimethylamido)titanium as precursors for TiO_2 deposition, which was carried out at a chamber temperature of 140 °C. This recipe, developed with the assistance of Cambridge Nanotech, used (for both precursors) a stopvalve opening time of 0.3 s, precursor pulse time of 180 s, and a precursor dwell time of 180 s. The ALD system is located in the Micro/Nanofabrication Facility of the Materials Research Lab (MRL).

5.6.4 Optical characterization

Reflectance and transmittance spectra were collected using a Si PDA spectrometer (Control Development, Inc.) hooked up to an Axio Observer D1 inverted microscope (Carl Zeiss, Inc.) with a white-light halogen lamp serving as the source. The microscope features a motorized sample stage that can take defined steps, which enabled spatially-resolved measurements used to characterize the radial GRIN template and transformed element. The setup is located in the Microscopy Suite of the Beckman Institute for Advanced Science and Technology

5.7 References

1. Canham, L. T. Silicon quantum wire array fabrication by electrochemical and chemical dissolution of wafers. *Appl. Phys. Lett.* **57,** 1046–1048 (1990).
2. Lehmann, V. & Gösele, U. Porous silicon formation: A quantum wire effect. *Appl. Phys. Lett.* **58,** 856–858 (1991).
3. Gal, M., Reece, P. J., Zheng, W. & Lerondel, G. Porous silicon: a versatile optical material. in *Proc. SPIE* **5277,** 9–16 (2004).
4. Smith, R. L. & Collins, S. D. Porous silicon formation mechanisms. *J. Appl. Phys.* **71,** R1–R22 (1992).
5. Frohnhoff, S. & Berger, M. G. Porous silicon superlattices. *Adv. Mater.* **6,** 963–965 (1994).
6. Vincent, G. Optical properties of porous silicon superlattices. *Appl. Phys. Lett.* **64,** 2367–2369 (1994).
7. Lorenzo, E. *et al.* Porous silicon-based rugate filters. *Appl. Opt.* **44,** 5415 (2005).
8. Ilyas, S. *et al.* Porous silicon based narrow line-width rugate filters. *Opt. Mater.* **29,** 619–622 (2007).

9. Pellegrini, V., Tredicucci, A., Mazzoleni, C. & Pavesi, L. Enhanced optical properties in porous silicon microcavities. *Phys. Rev. B* **52,** R14328–R14331 (1995).

10. Ghulinyan, M., Oton, C. J., Bonetti, G., Gaburro, Z. & Pavesi, L. Free-standing porous silicon single and multiple optical cavities. *J. Appl. Phys.* **93,** 9724–9729 (2003).

11. Reece, P. J., Lérondel, G., Zheng, W. H. & Gal, M. Optical microcavities with subnanometer linewidths based on porous silicon. *Appl. Phys. Lett.* **81,** 4895–4897 (2002).

12. Bjorklund, R. B., Zangooie, S. & Arwin, H. Adsorption of Surfactants in Porous Silicon Films. *Langmuir* **13,** 1440–1445 (1997).

13. Anderson, M. A. *et al.* Sensitivity of the optical properties of porous silicon layers to the refractive index of liquid in the pores. *Phys. Status Solidi A* **197,** 528–533 (2003).

14. Lin, V. S.-Y., Motesharei, K., Dancil, K.-P. S., Sailor, M. J. & Ghadiri, M. R. A Porous Silicon-Based Optical Interferometric Biosensor. *Science* **278,** 840–843 (1997).

15. Chan, S., Fauchet, P. M., Li, Y., Rothberg, L. J. & Miller, B. L. Porous Silicon Microcavities for Biosensing Applications. *Phys. Status Solidi A* **182,** 541–546 (2000).

16. Stewart, M. P. & Buriak, J. M. Chemical and Biological Applications of Porous Silicon Technology. *Adv. Mater.* **12,** 859–869 (2000).

17. Rong, G., Saarinen, J. J., Sipe, J. E. & Weiss, S. M. High Sensitivity Sensor Based on Porous Silicon Waveguide. in *Symposium I – Silicon-Based Microphotonics* **934,** (2006).

18. Rong, G., Najmaie, A., Sipe, J. E. & Weiss, S. M. Nanoscale porous silicon waveguide for label-free DNA sensing. *Biosens. Bioelectron.* **23,** 1572–1576 (2008).

19. Mulloni, V. & Pavesi, L. Porous silicon microcavities as optical chemical sensors. *Appl. Phys. Lett.* **76,** 2523–2525 (2000).

20. Ilyas, S. & Gal, M. Optical devices from porous silicon having continuously varying refractive index. *J. Mater. Sci. Mater. Electron.* **18,** 61–64 (2007).

21. Salonen, J., Lehto, V.-P. & Laine, E. Thermal oxidation of free-standing porous silicon films. *Appl. Phys. Lett.* **70,** 637–639 (1997).

22. Berger, M.. *et al.* Dielectric filters made of PS: advanced performance by oxidation and new layer structures. *Thin Solid Films* **297,** 237–240 (1997).

23. Li, Y. Y. *et al.* Polymer Replicas of Photonic Porous Silicon for Sensing and Drug Delivery Applications. *Science* **299,** 2045–2047 (2003).

24. Kelly, T. L., Gao, T. & Sailor, M. J. Carbon and Carbon/Silicon Composites Templated in Rugate Filters for the Adsorption and Detection of Organic Vapors. *Adv. Mater.* **23,** 1776–1781 (2011).

25. Singh, R. G., Singh, F., Agarwal, V. & Mehra, R. M. Photoluminescence studies of ZnO/porous silicon nanocomposites. *J. Phys. Appl. Phys.* **40,** 3090 (2007).

26. Li, J. & Sailor, M. J. Synthesis and characterization of a stable, label-free optical biosensor from TiO2-coated porous silicon. *Biosens. Bioelectron.* **55,** 372–378 (2014).

27. Dücsö, C. *et al.* Deposition of Tin Oxide into Porous Silicon by Atomic Layer Epitaxy. *J. Electrochem. Soc.* **143,** 683–687 (1996).

28. Granitzer, P. & Rumpf, K. Porous Silicon—A Versatile Host Material. *Materials* **3,** 943–998 (2010).

29. Oskam, G., Long, J. G., Natarajan, A. & Searson, P. C. Electrochemical deposition of metals onto silicon. *J. Phys. Appl. Phys.* **31,** 1927 (1998).

30. Fukami, K., Tanaka, Y., Chourou, M. L., Sakka, T. & Ogata, Y. H. Filling of mesoporous silicon with copper by electrodeposition from an aqueous solution. *Electrochimica Acta* **54,** 2197–2202 (2009).
31. Harraz, F. A. *et al.* Pore filling of macropores prepared in p-type silicon by copper deposition. *Phys. Status Solidi A* **202,** 1683–1687 (2005).
32. Fang, C., Foca, E., Xu, S., Carstensen, J. & Föll, H. Deep Silicon Macropores Filled with Copper by Electrodeposition. *J. Electrochem. Soc.* **154,** D45–D49 (2007).
33. Belmont, O., Bellet, D. & Bréchet, Y. Study of the cracking of highly porous p+ type silicon during drying. *J. Appl. Phys.* **79,** 7586–7591 (1996).
34. Pap, A. E. *et al.* Thermal oxidation of porous silicon: Study on structure. *Appl. Phys. Lett.* **86,** 041501 (2005).
35. Malitson, I. H. Interspecimen Comparison of the Refractive Index of Fused Silica*,†. *J. Opt. Soc. Am.* **55,** 1205 (1965).
36. DeVore, J. R. Refractive Indices of Rutile and Sphalerite. *J. Opt. Soc. Am.* **41,** 416 (1951).
37. Snow, P. A., Squire, E. K., Russell, P. S. J. & Canham, L. T. Vapor sensing using the optical properties of porous silicon Bragg mirrors. *J. Appl. Phys.* **86,** 1781–1784 (1999).
38. Weiss, S. M., Haurylau, M. & Fauchet, P. M. Tunable Porous Silicon Mirrors for Optoelectronic Applications. in *Symposia E/F – Physics and Technology of Semiconductor Quantum Dots – Nanocrystalline Semiconductor Materials and Devices* **737,** F3.50 (2002).
39. Bisi, O., Ossicini, S. & Pavesi, L. Porous silicon: a quantum sponge structure for silicon based optoelectronics. *Surf. Sci. Rep.* **38,** 1–126 (2000).

40. Weiss, S. M. & Fauchet, P. M. Electrically tunable porous silicon active mirrors. *Phys. Status Solidi A* **197,** 556–560 (2003).

41. Peumans, P., Yakimov, A. & Forrest, S. R. Small molecular weight organic thin-film photodetectors and solar cells. *J. Appl. Phys.* **93,** 3693–3723 (2003).

42. Qiao, H. *et al.* Optical properties of II-VI colloidal quantum dot doped porous silicon microcavities. *Appl. Phys. Lett.* **96,** 161106 (2010).

43. Setzu, S., Létant, S., Solsona, P., Romestain, R. & Vial, J. C. Improvement of the luminescence in p-type as-prepared or dye impregnated porous silicon microcavities. *J. Lumin.* **80,** 129–132 (1998).

44. Ning, H. *et al.* Transfer-Printing of Tunable Porous Silicon Microcavities with Embedded Emitters. *ACS Photonics* **1,** 1144–1150 (2014).

45. Brudieu, B. *et al.* Sol–Gel Route Toward Efficient and Robust Distributed Bragg Reflectors for Light Management Applications. *Adv. Opt. Mater.* **2,** 1105–1112 (2014).

46. Eisler, C. N., Abrams, Z. R., Sheldon, M. T., Zhang, X. & Atwater, H. A. Multijunction solar cell efficiencies: effect of spectral window, optical environment and radiative coupling. *Energy Environ. Sci.* **7,** 3600–3605 (2014).

47. Xu, L. *et al.* Enhanced Photon Collection in Luminescent Solar Concentrators with Distributed Bragg Reflectors. *ACS Photonics* **3,** 278–285 (2016).

48. Li, Y. Y., Kim, P. & Sailor, M. J. Painting a rainbow on silicon – a simple method to generate a porous silicon band filter gradient. *Phys. Status Solidi A* **202,** 1616–1618 (2005).

49. Collins, B. E., Dancil, K.-P. S., Abbi, G. & Sailor, M. J. Determining Protein Size Using an Electrochemically Machined Pore Gradient in Silicon. *Adv. Funct. Mater.* **12,** 187–191 (2002).

50. Ilyas, S. & Gal, M. Gradient refractive index planar microlens in Si using porous silicon. *Appl. Phys. Lett.* **89,** 211123–211123–3 (2006).

51. Goodman, J. W. *Introduction to Fourier Optics*. (W. H. Freeman, 2005).

52. Barth, D. S. *et al.* Macroscale Transformation Optics Enabled by Photoelectrochemical Etching. *Adv. Mater.* **27,** 6131–6136 (2015).

CHAPTER 6

SUMMARY AND FUTURE DIRECTIONS

6.1 Summary

In summary, this dissertation has focused on the application of PSi as a platform for GRIN photonics. **Chapter 1** provided a general introduction to PSi as a material system, including information about formation, microstructure, optical properties, photonic utility, and non-photonic applications. **Chapter 1** also very generally introduced the area of GRIN photonics and briefly discussed its discrete and continuous manifestations in the form of PhCs and transformation optics, respectively.

Chapter 2 described a method developed to modularly assemble optical microcavities comprised of a disparate cavity material sandwiched between PSi DBRs in a vertical cavity configuration. The modified transfer-printing methodology was shown to enable the construction of high-quality structures exhibiting large area uniformity that strongly modifies light emission from the cavity material, including polymers loaded with PbS QDs and solid-state GaAs thin films. Additionally, the concept of a PSi cavity coupling layer was developed and applied to both globally tune and spatially modulate the light emission from PSi-based hybrid microcavity architectures.

A new technique, called shape-defined PSi formation, was then exploited to construct novel PSi-based GRIN micro-optics. **Chapter 3** focused on utilizing a square micro-column (SMC) geometry to interact with in-plane light propagation. Owing to the structural birefringence of PSi, homogeneously etched PSi SMCs were observed to perform polarization splitting comparable to previously proposed dielectric gradient metasurfaces that require more complicated fabrication. Imparting a PSi SMC with a linear GRIN profile was demonstrated to generate unique, polarization selective lensing behavior. TM polarized light was found to focus to a diffraction-limited line along the optical propagation axis, while TE polarized light was separately focused into two distinct foci that were laterally displaced from the TM focal position.

Chapter 4 then demonstrated that arrays of Si rectangular blocks can be transformed into flat, PSi 1D GRIN microlens arrays (MLAs) that interact with through-plane light propagation. The approach for determining how to etch individual PSi microlenses with the desired GRIN profile was introduced, using the current density dependence of PSi's refractive index and etch rate to map the spatial GRIN profile to a temporal current density waveform to be applied during electrochemical etching. It was then shown that the flat PSi GRIN MLAs could be embedded in a transparent optical polymer, detached from the Si fabrication substrate, and planarized with combination of reactive ion etching and mechanical polishing. This combined design and process flow was used to realize two separate types of flat GRIN MLAs, one with a parabolic GRIN profile that generated an array of focal lines, and the other with a linear GRIN profile that generated a lattice of Bessel sheet beams.

Finally, the work in **Chapter 5** took aim at deploying PSi GRIN photonics to low optical absorption applications at visible wavelengths by using PSi as a template to be thermally oxidized and then infiltrated with TiO_2 by ALD. The material conversion process was characterized via optically homogeneous PSi templates, which demonstrated that thermal oxidation transforms a PSi template into a visibly transparent $PSiO_2$ structure that can be filled by ALD to create a $PSiO_2/TiO_2$ composite that is optically tuned by the extent of TiO_2 filling. The conversion process was applied to a discrete GRIN DBR, whose optical evolution was well-predicted by calculations based upon an effective medium summary of $PSiO_2/TiO_2$ processing. A continuous radial GRIN PSi template with a parabolic, lens-like phase profile was also transformed. It was found that this phase profile could be strongly modulated post-oxidation by infiltration with TiO_2, as the variable filling capacity across the template led to the GRIN profile being optically inverted.

6.2 Future Directions

The transfer-printing process behind the assembly of heterogeneous PSi-based microcavities in **Chapter 2** could most obviously be used to create tunable, hybrid on-chip light sources that are comprised largely of Si. While GaAs was used as a light-emitting module here, it is speculated that a properly designed gain medium, such as a multi-quantum-well structure[1], could be used to realize coherent light sources in the 900 nm ~ 1100 nm wavelength regime (i.e., where bulk Si is absorptive). From a broader perspective, the generality of the transfer-printing method, coupled with the unique optical properties of PSi, may offer a new paradigm in the assembly of other PSi-based architectures, including photonic/diffractive hybrids. For example, a PSi DBR can be printed on top of an NOA optical polymer that has been imprinted with a grating feature (**Figure 6.1**).

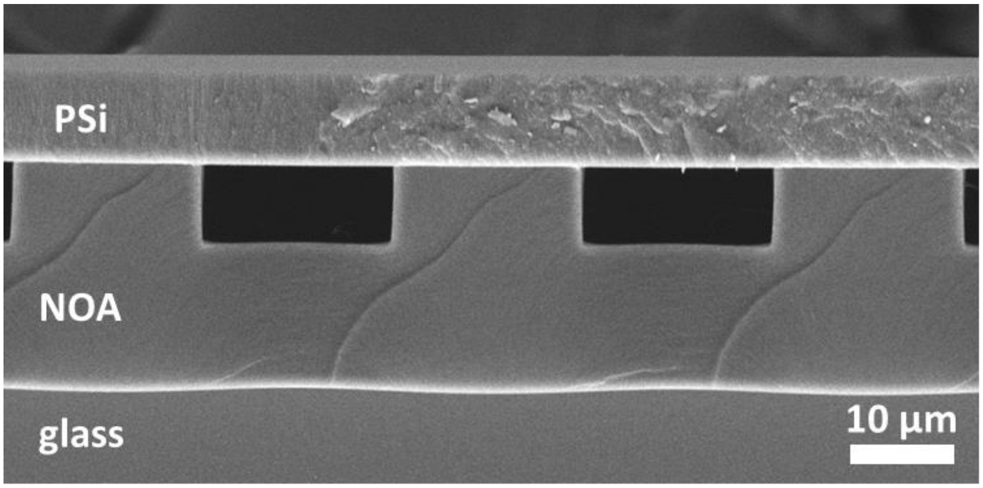

Figure 6.1. Hybrid element formed by printing a PSi DBR on top of a grating imprinted into a film of Norland Optical Adhesive (NOA). This approach could find use for assembling hybrid diffractive optics.

These hybrid architectures can also be considered for applications outside of photonics. Although not discussed in this dissertation, this concept was applied to interface PSi films with biopolymer membranes, such as poly(lactic-co-glycolic acid) (PLGA), to construct transient electronic brains sensors[2]. Additional opportunities exist in this space to create more complicated PSi/PLGA layered composites with tunable dissolution kinetics and tailored mechanical response to be applied as a platform for transient electronics or drug delivery.

The PSi SMCs developed in **Chapter 3** represent an exciting advance in the fabrication of 3D GRIN micro-optics, with the potential to be applied on-chip within photonic integrated circuits to perform polarization-selective operations like conversion or splitting of photonic modes. Future work to this end can consider new geometries and index profile, but the anisotropy of the PSi formation process[3] must be considered. For example, circular geometries do not electrochemically etch in a purely radial fashion (**Figure 6.2**) with crystalline Si, inhibiting access to complex GRIN optics like Luneburg lenses[4,5].

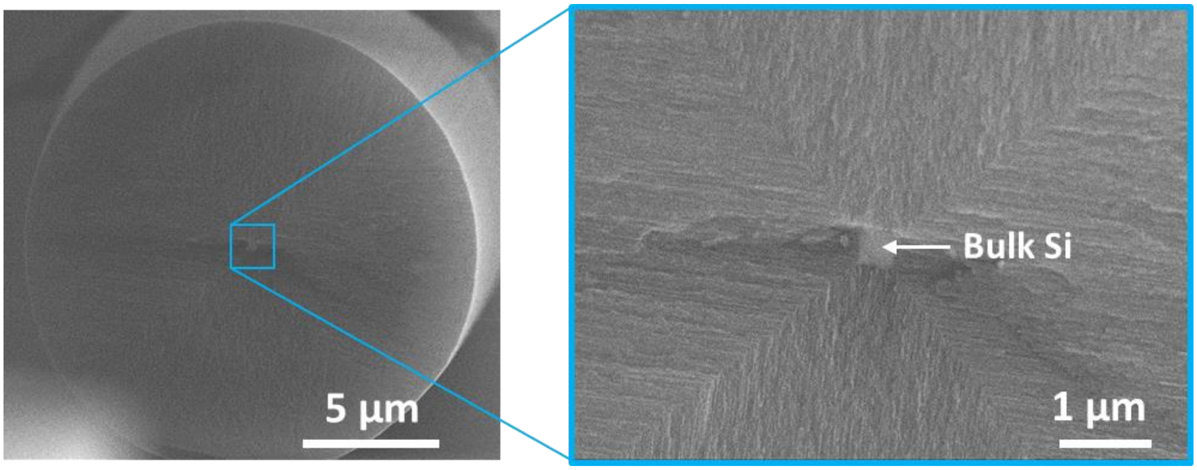

Figure 6.2. Observed anisotropy of PSi formation in crystalline Si microcylinders. The higher magnification SEM image (right) clearly shows that the pore formation proceeds along four planes, leading to an internal microstructure with four domains of linear pore trajectory, rather than a universally isotropic radial pore trajectory.

Amorphous Si may offer the potential for radial etches, as electrochemical processing of this nature has been reported with Ge[6], but this would prohibit thick structures like those in this dissertation because of limited film deposition thicknesses. While the anisotropy complicates the application of a PSi GRIN to a circular feature, homogeneous etched circular structures have exhibited interesting behavior in the form of elongated focal depths (**Figure 6.3**). These extended focal depths are reminiscent of a photonic nanojet, a propagating beam capable of possessing a sub-classical diffraction-limited beam waist propagating over distances many times the wavelength of light[7,8]. Photonic nanojects have been proposed for on-chip sensing and detection[9,10] and low-loss optical waveguiding[11,12]. Individual PSi microcylinders could represent an interesting new approach for sensitive photonic nanojects, while strings of these could be explored for waveguide-esque optical transport. Moreover, this can be coupled with the thermal oxidation utilized in **Chapter 5** to reduce optical losses and reduce the refractive index of the microcylinder relative its surrounding, as this refractive index contrast has a pronounced effect on photonic nanojets[7,8].

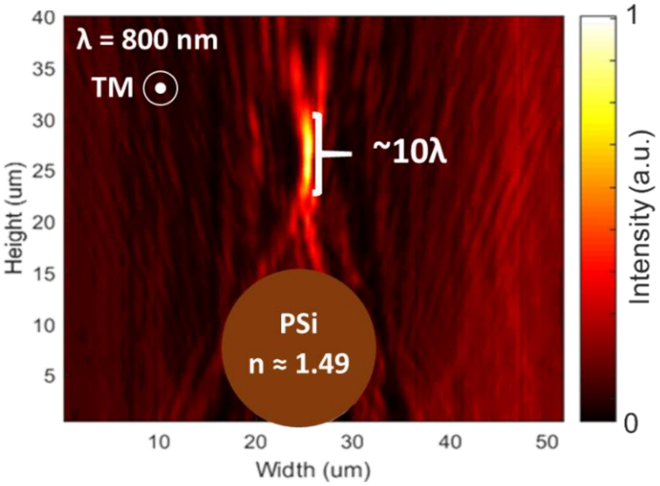

Figure 6.3. Experimentally measured cross-sectional stacked intensity distribution of a homogeneously etched PSi microcylinder exhibiting an elongated, photonic nanojet-like focus. The photonic nanojet intensity was observed by illuminating the microcylinder from below with a

Figure 6.3 (cont.) collimated TM-polarized with 800 nm wavelength. Measurements were performed by graduate student Aaron Holsteen in the lab of Prof. Mark Brongersma at Stanford University using the same confocal microscope system used in **Chapters 3** and **4.**

Geometric modifications can also be applied in moving forward with the MLAs demonstrated in **Chapter 4**. More specifically, future work can aim at maximizing the length of the lenses and minimizing the pitch between lenses to make the MLA more closely resemble a lenticular array. This would maximize the collection area and improve performance if integrated with detector pixels. One drawback with the current version of PSi GRIN MLAs is the presence of the n-type cap in the structure, which, although not quantified in this dissertation, is expected limit optical transmission efficiency because of large interfacial reflectance. To remedy this, one can consider using thin-film deposition to introduce anti-reflection layers on top of the n-type cap. Alternatively, a different capping material can be considered such as Si_3N_4[13,14], which has a lower refractive index than bulk Si and may even have the possibility to be removed after fabrication. Thermal oxidation of these MLAs, as done with PSi templates in **Chapter 5**, could open up their application space to integration with photovoltaic modules for concentrating solar radiation[15]. Thermal oxidation is also interesting in light of the above discussion pertaining to the n-type Si cap of the MLA elements, as this bulk Si could potentially be fully oxidized, significantly reducing interfacial reflectance losses.

Considering PSi as a template as in **Chapter 5** is a promising approach to extending the functionality of PSi GRIN photonics, including those discussed in **Chapters 2 - 4**, to visible wavelength operation. Beyond shape-defined PSi formation, other means of more complicated template fabrication should also be considered. One such approach is photo-mediated electrochemical etching[16], which can realize very complex and arbitrary GRIN profiles to engineer the phase of light interacting with the structure. Additionally, the recent development of direct imprint via metal-assisted chemical etching[17] opens up the possibility of refractive GRIN microlens templates. A flat PSi film with a GRIN profile along its etch depth could be imprinted with a stamp featuring an array of concave features, such that the PSi film becomes an array of convex microlenses that feature an axial GRIN, which can engineered to greatly mitigate third-order geometrical aberrations[18,19]. Transforming these PSi GRIN templates into $PSiO_2$ or $PSiO_2/TiO_2$ elements would create optically transparent MLAs for applications such as collections optics that increase the effective fill-factor of CCD pixels[20].

6.3 References

1. Yang, H. *et al.* Transfer-printed stacked nanomembrane lasers on silicon. *Nat. Photonics* **6,** 615–620 (2012).
2. Kang, S.-K. *et al.* Bioresorbable silicon electronic sensors for the brain. *Nature* **530,** 71–76 (2016).
3. Astrova, E. V., Ulin, V. P., Zharova, Y. A., Shul’pina, I. L. & Nashchekin, A. V. Anisotropy Effects in Electrochemical Etching of p+-Si. *J. Electrochem. Soc.* **159,** D172–D180 (2012).
4. Di Falco, A., Kehr, S. C. & Leonhardt, U. Luneburg lens in silicon photonics. *Opt. Express* **19,** 5156–5162 (2011).
5. Gabrielli, L. H. & Lipson, M. Integrated Luneburg lens via ultra-strong index gradient on silicon. *Opt. Express* **19,** 20122–20127 (2011).
6. Kempa, T. J., Bediako, D. K., Kim, S.-K., Park, H.-G. & Nocera, D. G. High-throughput patterning of photonic structures with tunable periodicity. *Proc. Natl. Acad. Sci.* **112,** 5309–5313 (2015).

7. Heifetz, A., Kong, S.-C., Sahakian, A. V., Taflove, A. & Backman, V. Photonic Nanojets. *J. Comput. Theor. Nanosci.* **6,** 1979–1992 (2009).

8. Kim, M.-S., Scharf, T., Mühlig, S., Rockstuhl, C. & Herzig, H. P. Engineering photonic nanojets. *Opt. Express* **19,** 10206 (2011).

9. Horiuchi, N. Light scattering: Photonic nanojets. *Nat. Photonics* **6,** 138–139 (2012).

10. McCloskey, D., Wang, J. J. & Donegan, J. F. Low divergence photonic nanojets from Si3N4 microdisks. *Opt. Express* **20,** 128 (2012).

11. Liu, C.-Y. & Wang, P.-K. Real-space observation of nanojet-induced modes in a chain of microspheres. *Phys. Lett. A* **378,** 1636–1641 (2014).

12. Yang, S. & Astratov, V. N. Photonic nanojet-induced modes in chains of size-disordered microspheres with an attenuation of only 0.08dB per sphere. *Appl. Phys. Lett.* **92,** 261111 (2008).

13. Tiggelaar, R. M., Verdoold, V., Eghbali, H., Desmet, G. & Gardeniers, J. G. E. Characterization of porous silicon integrated in liquid chromatography chips. *Lab Chip* **9,** 456–463 (2009).

14. Malsche, W. D. *et al.* Integration of porous layers in ordered pillar arrays for liquid chromatography. *Lab Chip* **7,** 1705–1711 (2007).

15. Yoon, J. *et al.* Ultrathin silicon solar microcells for semitransparent, mechanically flexible and microconcentrator module designs. *Nat. Mater.* **7,** 907–915 (2008).

16. Barth, D. S. *et al.* Macroscale Transformation Optics Enabled by Photoelectrochemical Etching. *Adv. Mater.* **27,** 6131–6136 (2015).

17. Azeredo, B. P. *et al.* Direct Imprinting of Porous Silicon via Metal-Assisted Chemical Etching. *Adv. Funct. Mater.* **26,** 2929–2939 (2016).

18. Manhart, P. K. & Blankenbecler, R. Fundamentals of macro axial gradient index optical design and engineering. *Opt. Eng.* **36,** 1607–1621 (1997).

19. Blough, C. G. *et al.* Effects of axial and radial gradients on Cooke triplets. *Appl. Opt.* **29,** 4008–4015 (1990).

20. Spring, K. R., Fellers, T. J. & Davidson, M. W. Introduction to Charge-Coupled Devices (CCDs). *Nikon Microsc. U*

APPENDIX A

DETERMINING REFRACTIVE INDEX BY THIN-FILM REFLECTANCE AND TRANSMITTANCE SPECTROSCOPY

A.1 Real refractive index of a thin film from reflectance spectrum

The real part of the refractive index (n) of a film can be readily extracted based upon the spacing between adjacent maxima (or minima) of the oscillations in the thin-film reflectance spectrum[1]. The generalized characterization, which features a film of porous silicon (PSi) on a bulk Si substrate, is displayed in **Figure A.1**.

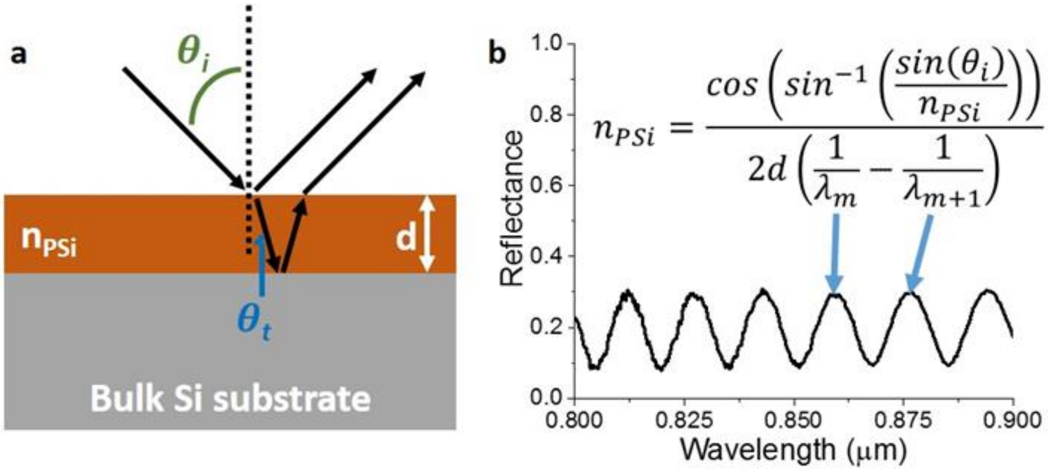

Figure A.1. (a) Side view schematic of reflected thin film intereference that is utilized for characterizing the dispersion curve of the thin film. (b) Representative reflectance versus wavelength curve and the corresponding transcendental equation that is used to extract dispersion information from the reflectance data.

The phase condition for constructive interference order m is given by

$$\frac{2\pi}{\lambda_m}\, n\, \Delta PL_m = 2\, \pi\, m \qquad \textbf{(A.1)}$$

where λ_m is the wavelength, n is the refractive index of the thin-film, and ΔPL is the difference in physical path length traveled by rays that reflect off the air/thin-film interface and thin-film/substrate interface, respectively. Taking the difference between the m and $m+1$ orders and rearranging, it can be shown that

$$n = \frac{1}{\Delta PL} \frac{1}{\left(\frac{1}{\lambda_m} - \frac{1}{\lambda_{m+1}}\right)} \tag{A.2}$$

where n is assumed to be constant in the spectral region between λ_m and λ_{m+1}. The physical path length difference is just the path length traversed by the ray that propagates in the film, which can be determined from the geometry of the problem to be

$$\Delta PL = \frac{2d}{\cos(\theta_t)} \tag{A.3}$$

This can be generalized to the angle of incidence (θ_i) using Snell's Law.

$$\Delta PL = \frac{2d}{\cos\left(\sin^{-1}\left(\frac{\sin(\theta_i)}{n}\right)\right)} \tag{A.4}$$

The final result is a transcendental equation of the form

$$n = \frac{cos\left(sin^{-1}\left(\frac{sin(\theta_i)}{n}\right)\right)}{2d\left(\frac{1}{\lambda_m} - \frac{1}{\lambda_{m+1}}\right)} \tag{A.5}$$

which can easily be solved for n using a program such as MATLAB. However, this is greatly simplified for reflectance collected at normal incidence, reducing the path length to $2d$, which transforms the transcendental equation for determining n into a closed-form solution.

$$n = \frac{1}{2d\left(\frac{1}{\lambda_m} - \frac{1}{\lambda_{m+1}}\right)} \tag{A.6}$$

For the work in this dissertation, various films of PSi were etched at different current densities and characterized with the above approach by collecting the reflectance spectrum at normal incidence, with the film thickness determined by scanning electron microscope imaging. It should be noted that if the thin film is on top of an optically transparent substrate, then the real part of the refractive index could similarly be extracted from the oscillations in the transmittance spectrum.

A.2 Imaginary refractive index of a thin film from reflectance and transmittance spectra

The imaginary part of the refractive index, also known as the extinction coefficient, indicates the absorptive nature of a material. Thus, the extinction coefficient can be calculated by quantifying material absorption (A) through a combination of reflectance (R) and transmittance (T) spectroscopy given that

$$R + T + A = 1 \qquad \textbf{(A.7)}$$

which simply indicates that energy must be conserved. The absorption can be related to the extinction coefficient (κ) through Beer's Law in the form

$$A = 1 - e^{-\frac{4\pi \kappa d}{\lambda}} \qquad \textbf{(A.8)}$$

such that **Equation (A.7)** can be recast as

$$R + T + 1 - e^{-\frac{4\pi \kappa d}{\lambda}} = 1 \qquad \textbf{(A.9)}$$

which simplifies to

$$R + T = e^{-\frac{4\pi \kappa d}{\lambda}} \qquad \textbf{(A.10)}$$

Thus, by collecting both the reflected and transmitted intensity of a thin film, the extinction coefficient at a particular wavelength (λ) can be calculated via the expression

$$\kappa = -\left(\frac{\lambda}{4\pi d}\right) \ln(R + T) \qquad \textbf{(A.11)}$$

where d is the physical thickness of the thin film, which can be determined by using a technique such as scanning electron microscopy (SEM). It should be noted that this assumes that absorption is only occurring in the thin film and not elsewhere, like the underlying substrate.

A.3 References

1. Manifacier, J. C., Gasiot, J. & Fillard, J. P. A simple method for the determination of the optical constants n, k and the thickness of a weakly absorbing thin film. *J. Phys. [E]* **9,** 1002 (1976).